Aus dem Neurowissenschaftlichen Forschungszentrum
der Medizinischen Fakultät Charité – Universitätsmedizin Berlin

DISSERTATION

Entwicklungsbiologischer und Interspezies Vergleich von Morphologie und Plastizität in neuronalen Netzwerken des Geruchssystems

Developmental and interspecies comparison of morphology and plasticity in neuronal circuits involved in olfactory information processing

zur Erlangung des akademischen Grades
Doctor of Philosophy (PhD)

vorgelegt der Medizinischen Fakultät
Charité – Universitätsmedizin Berlin

von

Laura Moreno Velasquez

aus Medellin, Kolumbien

Datum der Promotion: 25.06.2023

Table of Contents

1. List of Figures

2. List of abbreviations

ACSF	Artificial cerebrospinal fluid
AP	Action potential
aPCx	Anterior piriform cortex
ATP	Adenosine triphosphate
BL	Branch length
Cm	Membrane capacitance
DG	Dentate gyrus
Eu	Euclidian
fAHP	Fast after-hyperpolarization
fEPSP	Field excitatory post-synaptic potential
FF	Frequency facilitation
FOV	Field of view
GAD	Glutamic acid decarboxylase
GC	Granule cells
GECI	Genetically encoded Ca^{2+} indicator
GTP	Guanosine triphosphate
GUI	Graphical user interface
L1A	Layer 1A
L1B	Layer 1B
L2	Layer 2
L2A	Layer 2A
L2B	Layer 2B
LJP	Liquid junction potential
LOT	Lateral olfactory tract
LTP	Long-term potentiation
MF	Mossy fiber
NB	Number of branches
NGS	Normal goat serum
NS	Number of stems
OE	Olfactory epithelium
OB	Olfactory bulb
p, pd	postnatal days
PBS	Phosphate-buffered saline
PFA	Paraformaldehyde
pPCx	Posterior piriform cortex
PPR	Paired pulse ratio
PTP	Post-tetanic potentiation
Rec	Recording
Rin	Input resistance
ROI	Region of interest
SD	Standard deviation
Stim	Stimulation
STP	Short term plasticity
Syt7	Synaptotagmin 7
TDBL	Total dendritic branch length
Vm	Resting membrane potential

3. Abstract

The anterior piriform cortex (aPCx) is a three layered paleocortex receiving afferent inputs from the olfactory bulb as well as local and long-range associational inputs. Neurons in layer 2 are segregated into layer 2A and layer 2B according to their position, morphology and implementation in the sensory and associative circuits. The dendritic architecture of these neurons is determined during postnatal development and plays an important role for the functionality and circuit integration of the two cell types. Here, confocal imaging, electrophysiology, morphometry and Ca^{2+} imaging, were combined in order to study the development of the dendritic arborizations for both subtypes of layer 2 neurons.

Three different growth phases were identified: branch complexity determination, branch elongation and pruning, occurring at different time windows during development. Layer 2A and layer 2B neurons showed morphological differences between their apical and basal dendrites from the very first postnatal days; as well as phase-specific differences during development associated to differences in circuit implementation.

During the first postnatal week, early spontaneous network activity in layer 2 of the aPCx displayed differences between layer 2A and layer 2B neurons in their functional connectivity, reflected in the morphological dissimilarities between their basal dendritic trees during the period of branch complexity determination. Additionally, strong differences in growth phase three were observed. Pruning was exclusive for layer 2B neurons and selective for apical dendrites receiving layer 1A sensory inputs. These differences between layer 2A and layer 2B cells in their morphological and functional development exhibit the close association between circuit specificity and neuronal development.

Finally, synaptic plasticity in the mossy fiber (MF) pathway of the hippocampus in shrews was investigated and compared to mice. Although hippocampal structure in shrews is preserved, short and long-term plasticity at the MF synapsis was lower compared to mice, suggesting different involvement of these synapses in the behavioral outcome of different species.

4. Zusammenfassung

Der Cortex piriformis anterior (aPCx auf Englisch) ist ein dreischichtiger Paläokortex, der sensorische afferente Eingänge aus dem Riechkolben sowie intracerebrale assoziative Eingänge empfängt. Die Neuronen in Schicht 2 werden nach ihrer Position, Morphologie und Einbindung in die sensorischen und rekurrenten Netzwerke in die Schichten 2A und 2B unterteilt. Die dendritische Architektur dieser Neurone wird während der postnatalen Entwicklung festgelegt und spielt eine wichtige Rolle für die Funktionalität und Netzwerkintegration der beiden Zelltypen. Hier wurden konfokales Imaging, Elektrophysiologie, Morphometrie und Kalzium-Imaging kombiniert, um die Entwicklung der Dendritenbäume für beide Subtypen von Schicht-2-Neuronen zu untersuchen.

Es wurden drei verschiedene Wachstumsphasen identifiziert: Bestimmung der Komplexität der Verzweigung, Verlängerung der Verzweigung und strukturelle Vereinfachung, die in verschiedenen Zeitfenstern während der Entwicklung auftreten. Neurone der Schicht 2A und der Schicht 2B zeigten bereits in den ersten postnatalen Tagen morphologische Unterschiede zwischen ihren apikalen und basalen Dendriten sowie phasenspezifische Unterschiede während der Entwicklung, die mit Unterschieden in der Netzwerkimplementierung verbunden sind.

Während der ersten postnatalen Woche zeigte die frühe spontane Netzwerkaktivität in Schicht 2 des aPCx Unterschiede in der funktionellen Konnektivität zwischen Neuronen der Schicht 2A und Schicht 2B, die sich in den morphologischen Unterschieden zwischen ihren basalen Dendritenbäumen während der Bestimmung der Verzweigungskomplexität widerspiegelten. Außerdem wurden starke Unterschiede in der dritten Wachstumsphase beobachtet. Die strukturelle Vereinfachung fand ausschließlich bei Neuronen der Schicht 2B statt und war selektiv für apikale Dendriten, die sensorische Inputs der Schicht 1A erhielten. Diese Unterschiede zwischen Zellen der Schicht 2A und der Schicht 2B in ihrer morphologischen und funktionellen Entwicklung zeigen den engen Zusammenhang zwischen Netzwerkspezifität und neuronaler Entwicklung.

Schließlich wurde die synaptische Plastizität des Moosfaser (MF)-Trakts des Hippocampus bei Spitzmäusen untersucht und mit der von Mäusen verglichen. Obwohl die Struktur des Hippocampus bei Spitzmäusen erhalten ist, war die Kurz- und Langzeitplastizität an den MF-Synapsen im Vergleich zu Mäusen geringer, was auf eine unterschiedliche Beteiligung dieser Synapsen an spezifisch adaptierte Verhaltensweisen der beiden Spezies hindeutet.

5. Introduction

The anterior piriform cortex or primary olfactory cortex (aPCx) is a trilaminar palaeocortex and the first and largest cortical destination of sensory olfactory inputs. The aPCx is in charge of the recognition, separation and completion of odor patterns to finally achieve odor perception and discrimination (Wilson and Sullivan 2011). Peripheral odor information is transmitted from the olfactory epithelium (OE) located in the nose to the olfactory bulb (OB). Then, mitral and tufted cells from the OB form an axonal bundle known as the lateral olfactory tract (LOT) and transfer further sensory information to layer 1A in the aPCx (Neville and Haberly 2004) (Fig 1A1). These projections from the OB are diffuse and their target neurons are distributed across the aPCx without any preferential spatial structure (Bekkers and Suzuki 2013,Srinivasan and Stevens 2018). Additionally, aPCx receive excitatory associational inputs in layer 1B, 2 and 3 from within the aPCx and other brain regions (Neville and Haberly 2004), forming a recurrent network similar to the hippocampal CA3 (Guzman et al. 2016,Bolding et al. 2020,Franks et al. 2011).

This clear spatial determination between sensory and associative inputs is possible because of the laminar structure of the aPCx. Layer 2 is the main cellular layer of the aPCx and it is clearly divided into two sublayers according to the position, morphology, physiology and genetic molecular markers of its principal cells (Suzuki and Bekkers 2011,Choy et al. 2015,Diodato et al. 2016,Martin-Lopez, Ishiguro, and Greer 2019):
Layer 2A corresponds to the third most superficial part of layer 2 and contains mostly superficial (layer 2A) neurons, also known as semilunar cells. Layer 2B conforms the second and third deepest parts of layer 2 and consists of deep (layer 2B) neurons also known as superficial pyramidal cells (Fig 1A2). The two cell types play different roles in network incorporation: Layer 2A neurons have a very simple and sometimes non-existent basal dendritic tree and therefore, receive mostly sensory inputs that are then propagated to layer 2B and layer 3 neurons (Choy et al. 2015). In contrast, layer 2B neurons receive sensory inputs in layer 1A and in addition, sample associational inputs in layer 1B and 2 (Wiegand et al. 2011,Suzuki and Bekkers 2006).

This laminar organization of the afferent information converging in the aPCx is also reflected in the different dendritic trees, where sensory and associational inputs are compartmentalized. Apical dendrites of layer 2 neurons establish synaptic connections with the LOT sampling sensory information in layer 1A and recurrent information in layer 1B and 2. In contrast, basal dendrites receive exclusively associational inputs (Johenning et al. 2009, Wiegand et al. 2011). Thus, the aPCx displays a clear segregation of neurons that differ in their morphology but also in their functionality and involvement in different synaptic circuits.

While the structure and function of the layer 2A and 2B cells in the mature aPCx is well characterized, the development of these neurons is not known. Little is known regarding the emergence of the differences between these two cell types and specifically if these differences are predetermined or appear through activity-dependent mechanisms. Dendritic morphologies are unique to each neuronal type and together with their developmental patterns, are determinants of their function within the networks they conform (Lanoue and Cooper 2019). Extracellular signals, on the other hand, are crucial in guiding the dendritic growth, location, length and geometry (Dong, Shen, and Bülow 2015). Here, electrophysiology was used in combination with confocal imaging and 3D neuronal reconstruction techniques in order to study the developmental dendritic growth

of principal cells in layer 2 of the aPCx in acute brain slices (Fig 1B). Three dendritic growth phases were identified with differences specific to the two neuron types (layer 2A and 2B neurons) and the two arborizations (basal and apical dendritic trees).

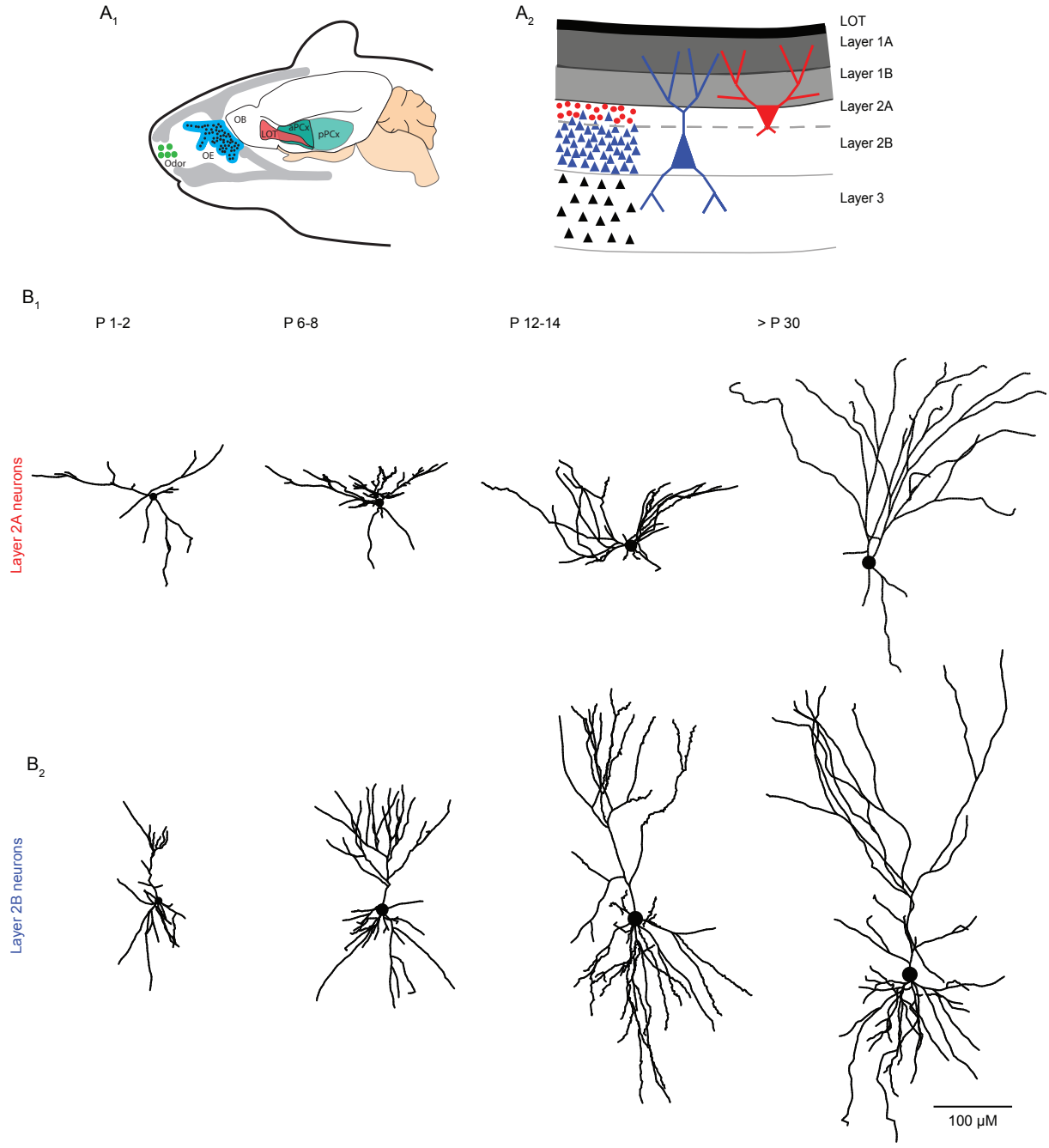

Figure 1: Representation of the two principal neurons in the anterior piriform cortex (aPCx) in the mouse brain during development. (A) Schemes of the location of the aPCx along the lateral olfactory tract (LOT) in the mouse brain (A1) and of the position of layer 2A (red) and layer 2B (blue) neurons within layer 2 of the aPCx (A2). OB stands for olfactory bulb, OE for olfactory epithelium and pPCx for posterior piriform cortex. (B) Dendritic reconstructions of layer 2A (B1) and layer 2B (A2) neurons at four time windows (expressed as postnatal days, p): right after birth (p1–p2), at the end of the first postnatal week (p6–p8), at the end of the second postnatal week (p12–p14), and after the fifth postnatal week (>p30). Figure modified from (Moreno-Velasquez et al. 2020).

Additionally, network involvement of layer 2A and layer 2B neurons was investigated using Ca^{2+} imaging in brain slices of Ai95-NexCre mice. In order to analyze the differences in early spontaneous activity between the two cell types, SamuROI software

was developed and used. This tool facilitated the exploratory analysis of the images acquired including the exploration, visualization, and processing of the data. The results showed how the morphological differences between the two cell types evident after the first postnatal week were also reflected in the local functional connectivity of layer 2 in the aPCx.

Finally, in a complementary study, synaptic plasticity in the hippocampus of shrews was investigated. Here, the focus was not on the comparison of the development of different morphologically defined circuits (associative versus sensory) in the same brain region but on the comparison of the functional properties of specific functionally defined inputs to an associative circuit between different species. The hippocampus is a very important structure in the processes of learning and memory and one of the most studied neuronal formations in the mammalian brain. Due to its extensive connectivity and because of its location, the hippocampus is also incorporated into olfactory processing, receiving strong and direct projections from the olfactory system (Eichenbaum and Otto 1992).

The Dentate Gyrus (DG) is the structure in charge of receiving olfactory cortical sensory signals and transferring non-overlapping information to the CA3 hippocampal area (Fig 9A) (Nicoll and Schmitz 2005). For instance, granule cells (GC), the principal neurons of the DG, effectively encode odor stimulus identities and are involved in learning the associations between the olfactory inputs and the behavioral outcome (Woods et al. 2020).

The information reaches then the CA3 region through the mossy fiber synapses (MF), consisting of the axonal projections from the GC in the DG (Nicoll and Schmitz 2005). Based on its functional and pharmacological properties, this connection between the DG and the associative CA3 network can be studied with high specificity, which makes it an ideal candidate for a comparative study. Although the MF synapse is one of the most investigated in the field, most of the MF studies have been limited to rodents, and there is a lack of understanding of these processes across mammalian species. One important question of interspecies comparison is the question of scaling. In this respect, the Etruscan shrew is one of the smallest mammals with preserved genetic and anatomical features in the neocortex and hippocampus (Naumann et al. 2012). The layout of the hippocampus is similar in shrews in comparison to other mammalian species, with clear structures like DG and CA3, CA2 and CA1 areas, although shrews have a higher relative convergence ratio of MF inputs into CA3 compared to mice (Beed et al. 2020). Here, differences in the shrew MF plasticity were found compared to mice, insinuating specific adaptation of neuronal circuits across species.

6. Materials and Methods

6.1 Slice preparation:

Acute brain slices were prepared as previously described in (Moreno-Velasquez et al. 2020) from C57Bl6/N and Ai95-NexCre (for Ca^{2+} imaging experiments) female and male mice and female and male Etruscan Shrews. For experiments in the piriform cortex, horizontal slices were preferred for most of the experiments since they preserve the rostro caudal association fibers (Markopoulos et al. 2008). Slices were prepared at different ages ranging from postnatal day 0 (p0) to p40. Mice older than p14 were decapitated in isoflurane anesthesia and brains were prepared in ice-cold artificial cerebrospinal fluid (ACSF; pH7.4) containing (in mM): 87 NaCl, 26 $NaHCO_3$, 10 glucose, 2.5 KCl, 3 $MgCl_2$, 1.25 NaH_2PO_4, 0.5 $CaCl_2$, and 50 sucrose. Slices were cut at 400 µm thickness and incubated at 35°C for 30 min. Then, slices were transferred to standard ACSF containing (in mM): 119 NaCl, 26 $NaHCO_3$, 10 glucose, 2.5 KCl, 2.5 $CaCl_2$, 1.3 $MgCl_2$, and 1 NaH_2PO_4. Slices from animals at p14 or younger were prepared in ice-cold standard ACSF and incubated for 30 min in standard ACSF at 35°C. The slices were then stored in standard ACSF at room temperature in a submerged chamber for 0.5–6 h before being transferred to the recording chamber.

For Ca^{2+} imaging experiments, spontaneous activity was required and high extracellular $[K^+]$ induces spontaneous network activity by increasing excitability of the neurons. Brains were then prepared in ice-cold high KCl-ACSF containing (in mM): 125 NaCl, 25 $NaCHCO_3$, 10 glucose, **4 KCl**, 1.25 NaH_2PO_4, 2 $CaCl_2$, and 1 $MgCl_2$. Slices were incubated at 35° C for 30min and stored at room temperature in a sub-merged chamber in high KCl-ACSF for 0.5–6 h.

For mossy fibers recordings, mice and shrews were decapitated in isoflurane anesthesia and brains prepared in high-sucrose ACSF containing (in mM): 50 NaCl, 25 $NaHCO_3$, 10 glucose, 150 sucrose, 2.5 KCl, 1 NaH_2PO_4, 0.5 $CaCl_2$, and 7 $MgCl_2$. Sagittal slices were cut at 400 µm thickness and incubated at 35°C for 30 min and subsequently stored in standard ACSF at room temperature in a sub-merged chamber for 0.5-6 h before being transferred to the recording chamber.

All animal procedures were performed in accordance with the national and institutional guidelines of the Charité-Universitätsmedizin Berlin. All procedures were approved by the local health authority and the local ethics committee (Landesamt für Gesundheit und Soziales, Berlin).

6.2 Electrophysiology:

Whole-cell current clamp experiments were performed as previously described in (Moreno-Velasquez et al. 2020) at near physiological temperature (32-34°C) using an Axon Multiclamp 700B amplifier (Molecular Devices). For morphological reconstructions, neurons were filled at four different time intervals expressed as postnatal days (p): right after birth (p1-p2), and after the first (p6-p8), second (p12-p14) and fifth (p30-p40) postnatal week. The electrophysiological characterization was limited to two age intervals: p12-14 and p30-p40. Here, signals were low pass filtered at 2 kHz and digitized at a sampling rate of 20kHz (BNC-2090, National Instruments Corporation). Pipettes (3–

6 MΩ) were filled with an intracellular solution containing (in mM): 135 K-gluconate, 6 KCl, 10 HEPES, 0.2 EGTA, 2 $MgCl_2$, 2 NaATP, 0.5 NaGTP, and 5 phosphocreatine Na (pH 7.3) and biocytin (0.20%). Liquid junction potential (LJP) was not corrected. Bridge balance compensation was applied in current clamp. Cells were discarded if the series resistance exceeded 30 MΩ.

For mossy fiber recordings, experiments were performed as previously described in (Beed et al. 2020) at room temperature and slices were continuously superfused with ACSF at a rate of 2.5 ml/min. Multiclamp 700B amplifier was used for extracellular field recordings in current clamp configuration. Signals were low pass filtered at 2 KHz and digitized at 10-20 KHz (BNC-2090, National Instruments Corporation). Field excitatory post-synaptic potentials (fEPSP) were electrically evoked at 0.05 Hz in the granule cell layer or the hilus region of the dentate gyrus (DG) and responses were recorded with a low resistance electrode in the *stratum lucidum* in the CA3 region. In order to confirm the mossy fiber origin of recorded signals, an agonist of type II metabotropic glutamate receptors (DCG IV) was applied at 1 µM. DCG IV suppresses release of neurotransmitters from the mossy fiber terminals into CA3 but does not from neighboring associational commissural synapses (Kamiya, Shinozaki, and Yamamoto 1996). Only responses inhibited by at least 80% were assumed to be pure mossy fiber signals and were considered for analysis.

6.3 Immunohistochemistry:

Immunohistochemistry of slices was performed as previously described in (Moreno-Velasquez et al. 2020). Slices with biocytin-filled cells were stored in 4% paraformaldehyde (PFA) overnight. Slices were then washed three times (10 min each) in Phosphate-buffered saline (PBS) following by incubation in blocking solution composed of 5% normal goat serum (NGS; Biozol), 1% Triton X-100 (Sigma), and PBS, for 3 hours at room temperature with gentle agitation.

Primary antibodies were then diluted in blocking solution (2.5% NGS, 1% Triton X-100, PBS), and slices were incubated at 4°C. Streptavidin marker conjugated to AF 488 (Invitrogen, S-32354; 1:500 dilution) was used to label biocytin-filled neurons, calretinin (anti-mouse; Millipore, MAB1568; 1:1000 dilution or anti-rabbit; SWANT, 7697; 1:4000 dilution) labeled the lateral olfactory tract (LOT) and mitral cell axons in layer 1A of the piriform cortex and glutamic acid decarboxylase (GAD) 67 (anti-mouse; Millipore, MAB 5406; 1:500 dilution), GAD 65/67 (anti-rabbit; Chemicon, AB 11070; 1:500 dilution), or gephyrin (anti-mouse; SYSY 147111; 1:500 dilution) were used to label interneurons.

After 72 hours, slices were washed two times (10 min each) with PBS and incubated with secondary antibodies (goat anti-rabbit AF 555, goat anti-rabbit AF 647, goat anti-mouse AF 555, goat anti-mouse AF 647; Invitrogen; 1:500 dilution in 0.5% Triton X-100, PBS) for 3 hours at room temperature. Finally, slices were washed three times in PBS (10 min each) and mounted on glass slides and embedded in mounting medium Fluoroshield with 4',6-diamidino-2-phenylindole (DAPI; Sigma).

6.4 Cell identification and morphological reconstructions:

Stained slices were visualized on a fluorescent microscope (10x objective, 0.3 N.A.; Leica) to identify and select the biocytin-filled neurons located in the aPCx for further

analysis. Selected slices were then imaged on an up-right Leica TCS SP5 confocal microscope (Leica Microsystems) through a 20x oil immersion objective (0.7 N.A.; Leica) with 405-nm (diode), 488-nm (argon), 568-nm (solid state), and 633-nm (helium-neon) laser lines. For biocytin-filled neurons, the soma was further imaged through a 63x oil immersion objective (1.4 N. A.; Leica) in order to exclude neurons positively labeled with any of the markers used to label interneurons (such as GAD67 or GAD65/67). Additionally, Neurons were further selected for reconstruction only when they displayed homogenous filling with biocytin and did not display any obvious cut in the dendritic trees.

Selected cells were then classified as previously described in (Moreno-Velasquez et al. 2020) according to their position in layer 2 of the aPCx using FIJI (https://imagej.nih.gov/ij/). The position in layer 2 was defined as the smallest distance from the soma to the border between layer 1B and layer 2A, normalized to the total width of layer 2 for each neuron. The border between layers 1A and 1B was also traced to classify the apical dendrites according to their synaptic inputs: dendrites receiving sensory inputs reaching layer 1A and dendrites receiving associational inputs reaching only layer 1B or layer 2. Neuronal morphologies of layer 2A (n=46/25 neurons/mice) and layer 2B (n=43/27 neurons/mice) were then reconstructed with neuTube software (Feng, Zhao, and Kim 2015). Reconstructed segments were then labeled as soma, basal dendrites, apical layer 1A dendrites, apical layer 1B dendrites and apical layer 2 dendrites and later exported as SWC files.

6.5 Ca^{2+} imaging:

Genetically encoded Ca^{2+} indicator (GECI) GCaMP6F was used for imaging spontaneous synchronous network activity in the piriform cortex. Nex-Cre mice (Goebbels et al. 2006) were crossed with Ai95 mice (Madisen et al. 2015) for constitutive GCaMP6F expression in excitatory cells. Slices were prepared during the first postnatal week. Population imaging was performed using a Yokogawa CSU-22 spinning disk microscope at 5000 rpm allowing the generation of a large field of view time series at a high acquisition rate. A 40x objective was used to focus the 488-nm laser onto the field of view and the emission light was filtered using a 515 ± 15-nm bandpass filter. Fluorescence was detected using an Andor Ixon DU-897D back-illuminated CCD, with a pixel size of 16 µm and Andor iQ software was used for data acquisition. Population Ca^{2+} imaging was performed at 10 or 40 Hz.

6.6 Data analysis:

6.6.1 Electrophysiological analysis:

Custom written routines in Python, previously described in (Moreno-Velasquez et al. 2020), were used to analyze intrinsic electrophysiological parameters of the cells. Resting membrane potential (Vm) was calculated as the mean value of the baseline before current was injected. Cells were discarded if the Vm was above -60 mV. For characterization, neurons were held at -60 mV. Input resistance (Rin), membrane time constant (Tau), and membrane capacitance (Cm) were calculated from the voltage response to an 80 pA hyperpolarizing current step. Action potential (AP) threshold was defined as the membrane potential at the point where the slope (dV/dt) reached 1% of its maximum. The fast after-hyperpolarization (fAHP) was defined as the difference between AP threshold and the minimum voltage seen within 5 ms after the AP peak. Finally, the instant firing

frequency was defined as the frequency between the first and second AP. For comparability, these values were extracted from the first 600 ms depolarizing current injection step that elicited at least nine APs.

For analysis of mossy fiber experiments, fEPSP amplitudes were measured as the average of 2 ms around the peak, with respect to 10 ms baseline before the stimulation artifact. In these recordings, four parameters were analyzed and compared between species: Frequency facilitation (FF), paired pulse ratio (PPR), post-tetanic potentiation (PTP) and long term potentiation (LTP). FF was measured by stimulating 20 times at 1Hz and changes in amplitude were normalized to 3 min baseline. PPR was calculated as the ratio of two fEPSP stimulated at an inter-pulse interval of 50 ms. LTP was induced with 4 trains of 125 pulses at 25 Hz. LTP increased was calculated 25 to 30 min after induction and normalized to 10 min baseline before induction. Finally, PTP was determined as the average of the signals during the first min after the LTP-induction protocol.

6.6.2 Morphological analysis:

Morphometric parameters were extracted with L-measure software (Scorcioni, Polavaram, and Ascoli 2008) and analyzed with R studio and Python using btmorph v2 (Torben-Nielsen 2014) and SciPy packages. Reconstructed neurons were classified in four groups (Fig 1) according to their age expressed as postnatal days (1-2 pd, 6-8 pd, 12-14 pd and ≥ 30 pd) and in two groups according to their position (Layer 2A and Layer 2B).

Basal and apical dendritic growth were described and compared for the two neurons in the different age intervals according to the following parameters: number of branches (NB), total dendritic branch length (TDBL), number of stems (NS), average branch length (BL) and distribution of branches as a function of the distance from the soma. Additionally, for the apical dendritic tree, branches were compared according to their synaptic inputs with the following parameters: NB in layer 1A, layer 1B and layer 2, number of intermediate branches and tips in layer 1A, TDBL and average BL of branches in layer 1A and BL distribution.

6.6.3 Imaging analysis:

For population Ca^{2+} imaging, fields of view (FOVs) with at least 5 min of recordings were included in the analysis. Videos were motion corrected using Suite2p (Pachitariu et al. 2016) and analyzed using custom Python code and SamuROI (Rueckl et al. 2017).

SamuROI (Structure analysis of multiple user-defined ROIs) is an open source python-based software developed to facilitate the exploratory analysis of imaging data with complex spatio-temporal structure at three different spatial scales: micro-scale for subcellular compartments, meso-scale for whole cell and population imaging and macro-scale for large brain regions. The built-in graphical user interface (GUI) displays the data in three different domains: space (frame view), time (raster view) and amplitude (trace view). This characteristic allows the user to comfortably explore, visualize and process the data.

For best performance, SamuROI requires python code and the interactive shell Jupyter notebook is recommended in order to get all of the features for data accessing and

processing. The interaction between the GUI and the python notebook was designed as "Document-view" design pattern (Gamma et al. 2015). In document view, the data (arrays containing the videos and masks for instance) and its presentation on the GUI do not depend on one another but there is a signal slot pattern that allows communication between them. This signaling structure allows then that changes in one side are communicated to all parts on the other side and vice versa. This means that if there is a change on the Jupyter notebook, all the views on the GUI will be inform and update and the same way if there are interactions with the GUI that updates the data.

Ca^{2+} imaging analysis in the piriform cortex was performed as previously described in (Moreno-Velasquez et al. 2020). Recordings were included only if motion artefacts could be corrected. Each pixel of the raw data was normalized using the six-sample window with the lowest standard deviation (SD). Traces were extracted from each region of interest (ROI), and event detection was conducted. Events were detected as increases in $\Delta F/F>2.5$ SDs from baseline with a peak width of at least two consecutive samples. Results were manually checked and events were excluded based on the inter-event interval, amplitude, signal-to-noise ratio, and peak width. Incomplete events at the start or end of each recording were excluded from analysis. The rates of false positives (4.5%) and negatives (5.1%) were calculated from a random subset of the data consisting of 100 cells and three mice.

For detection of global events, the average change in fluorescence for all pixels of layer 2 in the piriform cortex, including the neuropil, was measured using a rectangular ROI defined by the upper and lower boundaries of layer 2. Layer 2 was delineated based on cell bodies density.

For single-cell analysis, image segmentation was performed with ilastik software (Sommer et al. 2011). Ilastik was trained to segment z-projection sum images of a subset of FOVs to produce a five-label image containing nuclei, somata, bright debris, dark debris, and background. Neurons were detected using the nuclei label and false positives were manually rejected. With these cell locations, the somata image was divided into territories using watershed segmentation, and only the nearest pixels to each nucleus were included. ROIs with fewer than 70 pixels were rejected. $\Delta F/F$ for each ROI was calculated and an estimate of the local neuropil contribution was subtracted using an equal number of randomly selected non-cell pixels within a fixed radius of 70 pixels.

6.6.4 Statistics:

Statistical tests were performed using the SciPy library in python and the DABEST package in R (Ho et al. 2019). For figure 8, data was tested for normality and according to this, unpaired t test (not normally distributed single comparisons) was applied to compared the percentage of coactive neurons in the different locations of layer 2 in the aPCx. Additionally, Spearman correlation test was used to measure the association between cell position and dendritic branch-length. Otherwise, estimation-based statistics with mean-difference plots were used to display all the other results (Ho et al. 2019).

7. Results

7.1 Identification of the piriform cortex during postnatal growth

For collecting the data, whole cell patch clamp was performed in 400 µm acute brain slices. Random excitatory cells were recorded along the rostro caudal axis and for the whole extent of the anterior piriform cortex (aPCx) (Fig 1A). While patching, cells were simultaneously filled with biocytin for later morphological reconstructions (Fig 2A1).

In order to identify the location of the recorded cells, slices were also post hoc stained with DAPI and Calretinin. The location of the aPCx throughout development was confirmed with Calretinin as it stains the LOT and fibers in layer 1A (Sarma, Richard, and Greer 2011) (Fig 2A2). In horizontal slices, aPCx lies along the LOT (Markopoulos et al. 2008). Additionally, DAPI stain of cell bodies was used to delineate the whole extent of layer 2 (Fig 2A3), since in this layer the cell body density is higher in comparison with layers 1 or 3. For consistently classifying the recorded neurons throughout the different age groups, layer 2 was further divided into layer 2A (comprising the upper third bordering layer 1) and layer 2B (deep two thirds bordering layer 3). This classification was chosen considering the differences in morphology, electrophysiology and genetics of the cells located in the superficial and deep layer 2 in the aPCx (Choy et al. 2015, Diodato et al. 2016, Martin-Lopez, Ishiguro, and Greer 2019, Suzuki and Bekkers 2006).

Finally, interneurons were also post hoc stained with markers such as GAD 67 and only negative cells (Fig 2B) were further treated and analyzed.

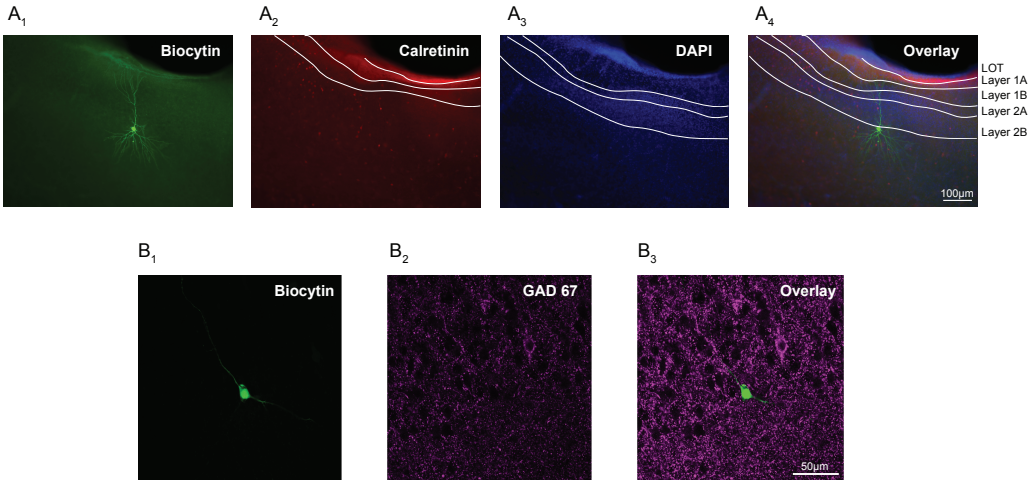

Figure 2: Postnatal localization of the aPCx and identification of the two principal neurons in layer 2 of the aPCx. (A) Confocal image of a slice containing one recorded neuron filled with biocytin (A1) and, additionally, post hoc labeled with calretinin (A2) and DAPI (A3). The overlay (A4) shows the recorded neuron located in the layer 2B/3 of the aPCx. LOT stands for lateral olfactory tract. (B) Confocal image of a recorded neuron at a bigger scale (63x, B1) and the correspondent field of view labeled with GAD 67 (B2). The overlay (B3) shows that the recorded neuron is negative for the interneuron stain. Figure modified from (Moreno-Velasquez et al. 2020).

7.2 Different sublayers of layer 2 comprise different cell types

The adult aPCx has been well characterized. Layer 2 is dominated by two distinctive cell types: semilunar cells and superficial pyramidal cells, with different location in layer 2,

different morphologies and genetics (Suzuki and Bekkers 2006, Wiegand et al. 2011, Suzuki and Bekkers 2011, Diodato et al. 2016). Semilunar cells are located in layer 2A and are characterized by a very simple, sometimes non-existent, basal dendritic tree. Superficial pyramidal cells are located in layer 2B and have a larger and more complex basal dendritic tree (Suzuki and Bekkers 2011, Wiegand et al. 2011).

In order to ensure an unbiased classification of the cells throughout development, selected cells were classified as layer 2A and layer 2B cells (Fig 3A) according to their position in layer 2 and the total dendritic branch length (TDBL) of the basal dendritic tree, since this measurement illustrates the complexity of the basal arborization. The normalized position of the cells in layer 2 was plot against the basal TDBL for four time windows: directly after birth (1-2 pd, layer 2A: n=6/4; layer 2B: n=12/6 neurons/mice, Fig 3B1), at the end of the first (6-8 pd, layer 2A: n=10/5; layer 2B: n=10/7 neurons/mice, Fig 3B2) and second (12-14 pd, layer 2A: n=11/8; layer 2B: n=9/8 neurons/mice, Fig 3B3) postnatal weeks and after the critical period for plasticity of sensory synapses (>30 pd, layer 2A: n=19/6; layer 2B: n=12/6 neurons/mice, Fig 3B4) (Poo and Isaacson 2007, Franks and Isaacson 2005). The data shows a clear correlation between these two parameters for all of the time windows, with a superficial to deep increasing gradient of basal dendritic length. Furthermore, basal dendritic trees of classified layer 2A neurons have a smaller number of stems (NS) and number of branches (NB) compared to the basal dendritic tree of layer 2B neurons (Fig 5B1-2). These results prove that the basal TDBL is a sufficient morphologic parameter to distinguish and classify between superficial (layer 2A) and deep (layer 2B) cells in layer 2 of the aPCx.

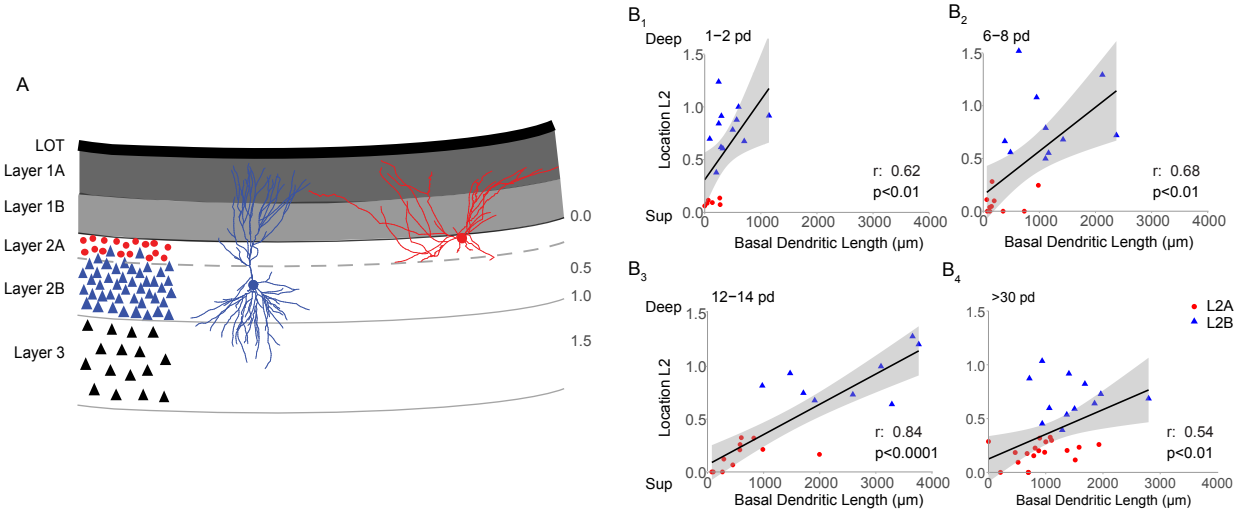

Figure 3: Classification of two cell types in aPCx according to their position and basal dendritic length. (A) Schematic showing the sublayers of the piriform cortex and principal neurons belonging to these sublayers; layer 2A neurons in red and layer 2B neurons in blue. LOT stands for lateral olfactory tract. (B) Correlation between the total basal dendritic length and the location of the cells in layer 2 is shown at four time windows, expressed as postnatal days, pd (B1: 1–2 pd, B2: 6–8 pd, B3: 12–14 pd, B4: >p30 pd). Spearman r and p values are shown for each time group. Figure modified from (Moreno-Velasquez et al. 2020).

7.3 Electrophysiological properties of layer 2 neurons during development

In previous studies, layer 2A and layer 2B neurons have been reported to show different intrinsic electrophysiological properties: Layer 2A neurons exhibited significantly higher input resistances, membrane time constants and resting potentials compared to Layer 2B

neurons (Suzuki and Bekkers 2006). Additionally, layer 2B neurons were found to fire APs with an initial high-frequency burst in contrast to layer 2A neuros which fired a regular train of APs in response to a depolarizing current step (Suzuki and Bekkers 2006).

In this study, however, electrical differences between the two cell types are not evident. Electrophysiological characterization was performed for neurons during and after the critical period (12-14 pd: Layer 2A n=10/6; layer 2B n=8/7 and >30 pd: Layer 2A n=14/7; layer 2B n=9/6 neurons/mice) (Fig 4B).

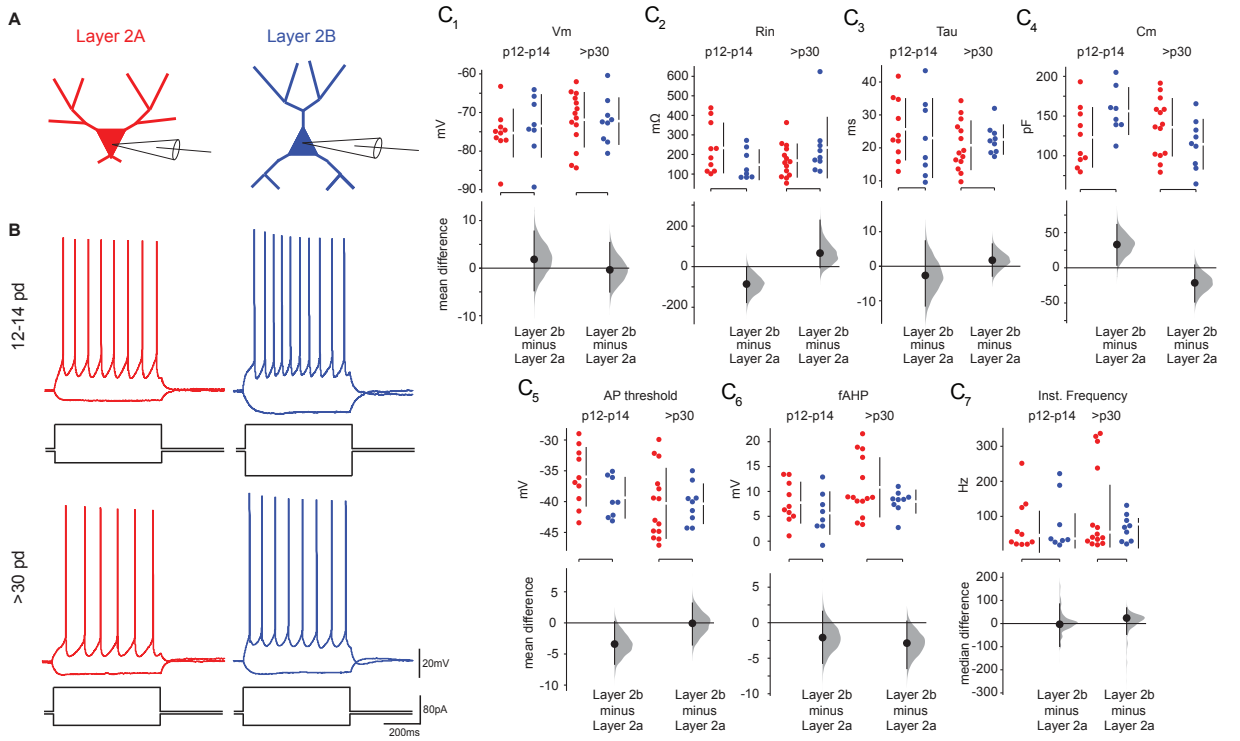

Figure 4: Electrophysiological characterization of the two cell types in the aPCx. (A) Visual representation of layer 2A (red) and layer 2B (blue) neurons. B, firing profile of the two different cell types in response to the corresponding current steps (at the bottom) at two age intervals expressed in postnatal days, pd (12-14 pd and >30 pd) and their respective intrinsic electrophysiological parameters: Resting potential (Vm, C1), input resistance (Rin, C2), time constant (Tau, C3), membrane capacitance (Cm, C4), action potential Threshold (C5), fast after hyperpolarizing potential (fAHP, C6) and instant frequency (C7). Mean and median differences are shown in Cumming estimation plots. The raw data is plotted on the upper axes; each mean or median difference is plotted on the lower axes as a bootstrap sampling distribution. Mean and median differences are depicted as dots and the 95% confidence intervals are indicated by the ends of the vertical error bars. Figure modified from (Moreno-Velasquez et al. 2020).

Input resistances of layer 2A neurons show a trend towards higher values compared to layer 2B neurons at 12-14 pd; similar to the values observed before (Suzuki and Bekkers 2006). Nevertheless, this tendency disappears after the critical period (Fig 4C2). Furthermore, our data displays less pronounced differences in Vm, Tau, Cm, AP threshold, fAHP and instant frequency compared to the ones previously reported (Fig 4C1-7) (Suzuki and Bekkers 2006). This discrepancy may be due to two factors: (a) differences in sampling, since in this study neurons were recorded within the whole extend of layer 2 instead of focusing exclusively in the lower and upper border as has been done before (Suzuki and Bekkers 2011). And (b) changes in intrinsic properties as a consequence of using k-gluconate-based intra in opposition to the previously used KMESO4-based intra (Kaczorowski, Disterhoft, and Spruston 2007, Zhang et al. 1994).

However, morphology and location were sufficient to solidly classify and distinguish layer 2A and layer 2B neurons over development (Fig 3).

7.4 Dendritic developmental growth in layer 2 neurons

In addition to the morphological and electrophysiological differences of the olfactory neurons, the aPCx is also divided according to its synaptic inputs, receiving compartmentalized sensory and associational inputs. Apical dendrites of layer 2 neurons sample both sensory and associational inputs in layer 1A and 1B respectively, while basal dendrites sample exclusively associational inputs in layer 2 and 3 (Johenning et al. 2009, Bekkers and Suzuki 2013).

To describe the growth and complexity of the dendritic trees, a set of morphometric parameters were selected: NS, NB, TDBL, average BL and distribution of branches as a function of the distance from the soma (Figs 5 and 6). According to these parameters, three different developmental growth phases were identified in the two dendritic trees of layer 2A and 2B neurons: (1) branch addition and determination of branch complexity; (2) branch elongation and (3) pruning.

7.4.1 Development of the basal dendritic tree

As mentioned before, basal dendrites of layer 2 neurons receive exclusively associational inputs (Johenning et al. 2009) and therefore, basal dendritic length and complexity are good indicators of neuron incorporation in the recurrent circuit. An increasing gradient in the TDBL has been observed in relation to the position of the neurons from superficial to deep (Fig 3) and following the classification of the neurons into layer 2A and layer 2B, differences in the architecture of the basal dendritic tree between the two cell types can be observed since the very first post-natal days. Growth phase one, consisting of the determination of branch complexity, is represented by NS and NB. These parameters are larger in basal dendritic trees of layer 2B than in layer 2A neurons directly after the birth of the mice and throughout development (Fig 5B). Moreover, in layer 2B neurons, the largest increase in NB takes place during the first postnatal week (Fig 5B2), which means that branch complexity is already determined by then; while in layer 2A neurons branch addition is only noteworthy over the whole developmental period observed, namely when comparing NB right after birth to NB after the fifth postnatal week (Fig 5B2).

Growth phase two consists of branch elongation and is reflected in changes in the branch length. In layer 2B neurons, there is significant increase in TDBL during the first and second postnatal week (Fig 5C1); this increase is caused by a combination of branch addition and branch elongation. However, in layer 2B neurons, individual branch length increase is only noticeable during the second postnatal week (Fig 5C2), meaning that the second growth phase occurs during this period. Similar to growth phase one, in layer 2A neurons, TDBL and average BL changes are only noteworthy over the whole developmental period observed (Fig 5C).

Finally, growth phase three, consisting on branch pruning, is present only in basal dendritic tree of layer 2B neurons. In these cells, dendrites prune after the second postnatal week, both with respect to NB and BL (Fig 5B and 5C). The distribution of basal branch density as a function of distance from the soma is similar for both cell types, with

a shift towards the right for layer 2B neurons, demonstrating larger complexity for this neuron type (Fig 5D).

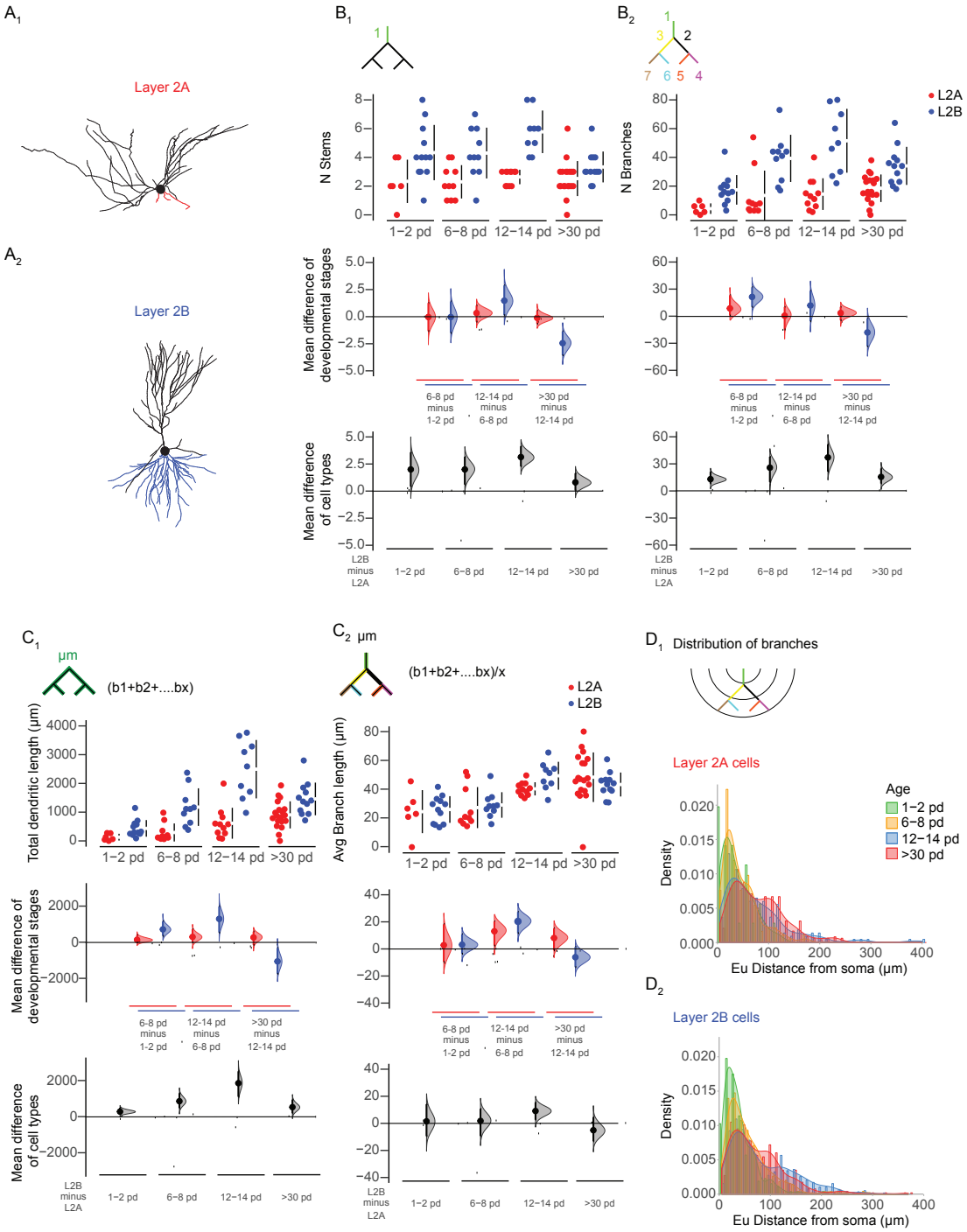

Figure 5: Morphology of the basal dendritic tree over development. (A) Visual representation of layer 2A (A1) and 2B (A2) neurons. (B-C) Morphologic parameters used to describe growth patterns of basal dendrites of Layer 2A (red) and layer 2B (blue) neurons at four different time ranges (expressed as postnatal days, pd): number of basal stems per cell (B1), total number of basal branches per cell (B2), total basal dendritic length per cell (C1) and average basal branch length per cell (C2). These parameters are shown in Cumming estimation plots, the raw data are plotted on the upper axes; mean differences between developmental stages are plotted on the middle axes and mean differences between the cell types are plotted on the lower axes, as a bootstrap sampling distribution. Mean differences are depicted as dots and the 95% confidence intervals are indicated by the ends of the vertical error bars. (D) Densities of the distributions of basal branches for layer 2A (D1) and layer 2B (D2) neurons are displayed as a function of the Euclidian distance from the soma at the same four time intervals: 1-2 dp (green), 6-8 pd (yellow), 12-14 pd (blue) and >30 pd (red). Figure modified from (Moreno-Velasquez et al. 2020).

These results confirm that the morphologies of basal dendritic trees differ between layer 2A and 2B neurons, that these differences are determined already since growth phase one and are visible over development.

7.4.2 Development of the apical dendritic tree

Semilunar and superficial pyramidal cells have also shown morphological differences in their apical dendritic tree in NS, NB, TDBL and branch distribution (Suzuki and Bekkers 2011, Bathellier, Margrie, and Larkum 2009). In this respect, layer 2A and layer 2B neurons are also expected to show differences in their apical dendritic tree. In this study, the most evident difference between the two cell types is found in the NS; while layer 2B neurons consistently show one or two apical stems per neuron, layer 2A neurons show 2 or more (Fig 6B1). Additionally, apical dendrites of layer 2A and layer 2B neurons also diverge in their developmental trajectory. In growth phase one, layer 2B neurons define their NS since birth, but layer 2A neurons display a significant increase in NS after the first postnatal week (Fig 6B1). As well in this period, the largest increase in NB is observed for both cell types: 75% of total increase of NB for layer 2A neurons and 90% of total increase of NB for layer 2B neurons (Fig 6B2). This means that by the end of the first postnatal week the complexity of the apical dendritic trees is defined and growth phase one is completed.

Regarding growth phase two, TDBL of apical dendrites of layer 2A neurons significantly increases by the end of the second and fifth postnatal week (Fig 6C1) and in layer 2B neurons, TDBL significantly increases during the first and second postnatal week (Fig 6C1). However, as it was mentioned before, increases in TDBL could be due to the addition of new branches or the elongation of the existing ones. In this regard, individual apical dendrites of both layer 2A and layer 2B neurons show significant elongation after the second postnatal week and by the fifth postnatal week (Fig 6C2), depicting growth phase two in these two periods.

Growth phase three also differs within the two cell types. Whereas in layer 2A neurons, there is a reduction of NS between the second and fifth postnatal week (Fig 6B1), in layer 2B neurons a reduction is visible for the same period but in NB (Fig 6B2); besides, this reduction is accompanied by an increase in the average BL (Fig 6C2) and a halt in TDBL increase (Fig 6C1). These results highlight another of the differences between the apical trees of the two cell types: Although throughout development and up to the end of the second postnatal week both cell types show similar TDBL, by the fifth week layer 2B neurons exhibit a shorter apical dendritic tree compared to layer 2A neurons due to the pruning (Fig 6C1).

Finally, branch distributions as function of the distance from the soma illustrate more clearly the differences in the developmental trajectories and spatial arrangement of the two cell types. During the first two postnatal weeks, layer 2A neurons branch close to the soma and their distribution is single-peaked (Fig 6D1) opposed to layer 2B neurons that show a second peak of branching (Fig 6D2). However, during the second growth phase, layer 2A neurons show a second peak and layer 2B neurons shift their second peak more distal from the soma, indicating that elongation of branches is not limited to the tips but is also happening in intermediate branches (Fig 6D). Finally, pruning of layer 2B neurons is observed in a reduction of the second peak, suggesting a shortening of distal dendrites and equalizing the branch distribution of both cell types (Fig 6D).

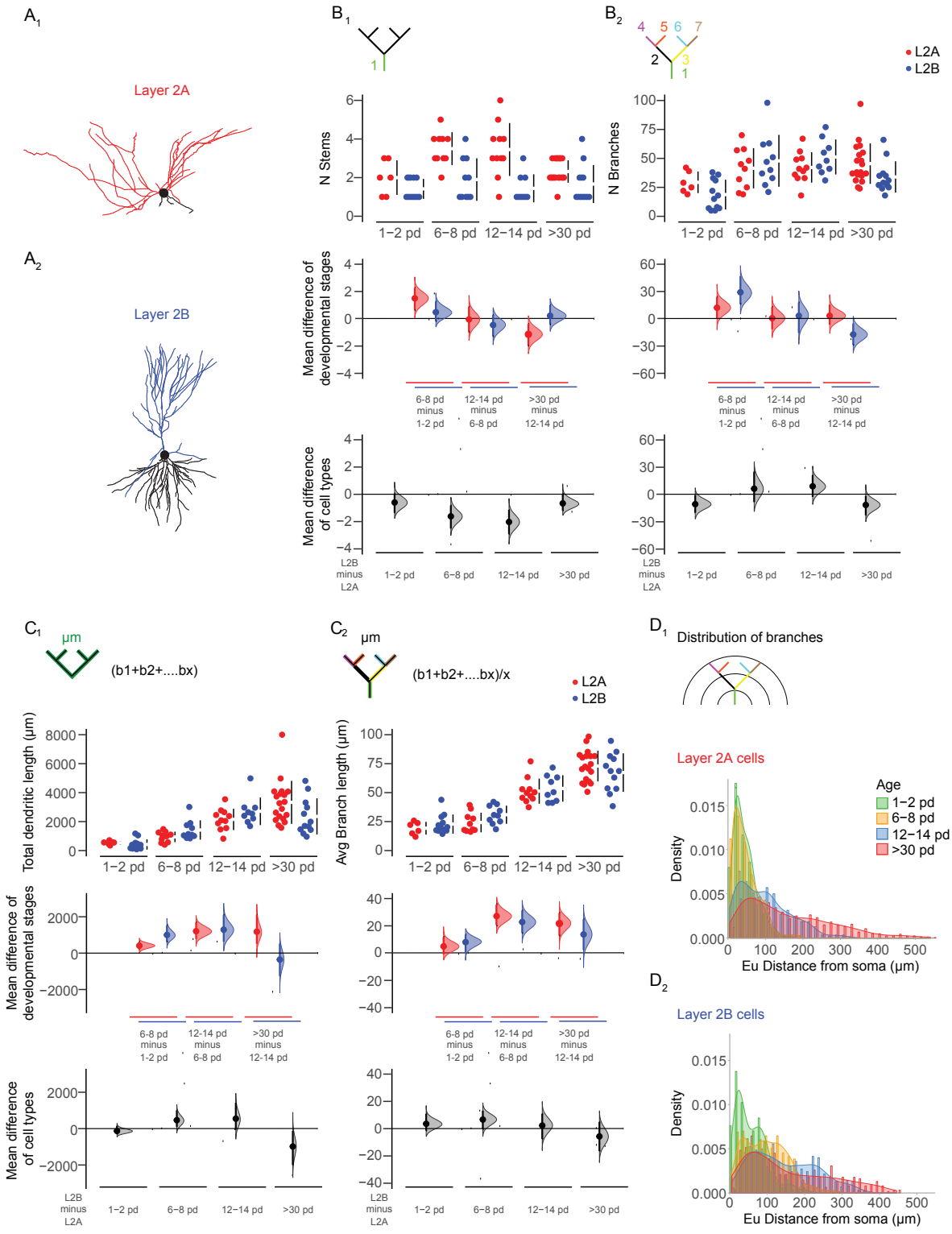

Figure 6: Morphology of the apical dendritic tree over development. (A) visual representation of layer 2A (A1) and 2B (A2) neurons. (B-C) Morphologic parameters used to describe growth patterns of apical dendrites of Layer 2A (red) and layer 2B (blue) neurons at four different time ranges (expressed as postnatal days, pd): number of apical stems per cell (B1), total number of apical branches per cell (B2), total apical dendritic length per cell (C1) and average apical branch length per cell (C2). These parameters are shown in Cumming estimation plots, the raw data are plotted on the upper axes; mean differences between developmental stages are plotted on the middle axes and mean differences between the cell types are plotted on the lower axes, as a bootstrap sampling distribution. Mean differences are depicted as dots and the 95% confidence intervals are indicated by the ends of the vertical error bars. (D) Densities of the distributions of basal branches for layer 2A (D1) and layer 2B (D2) neurons are displayed as a function of the Euclidian distance from the soma at the same four time intervals: 1-2 dp (green), 6-8 pd (yellow), 12-14 pd (blue) and >30 pd (red). Figure modified from (Moreno-Velasquez et al. 2020).

7.4.3 Selective pruning in apical dendritic tree of layer 2B neurons

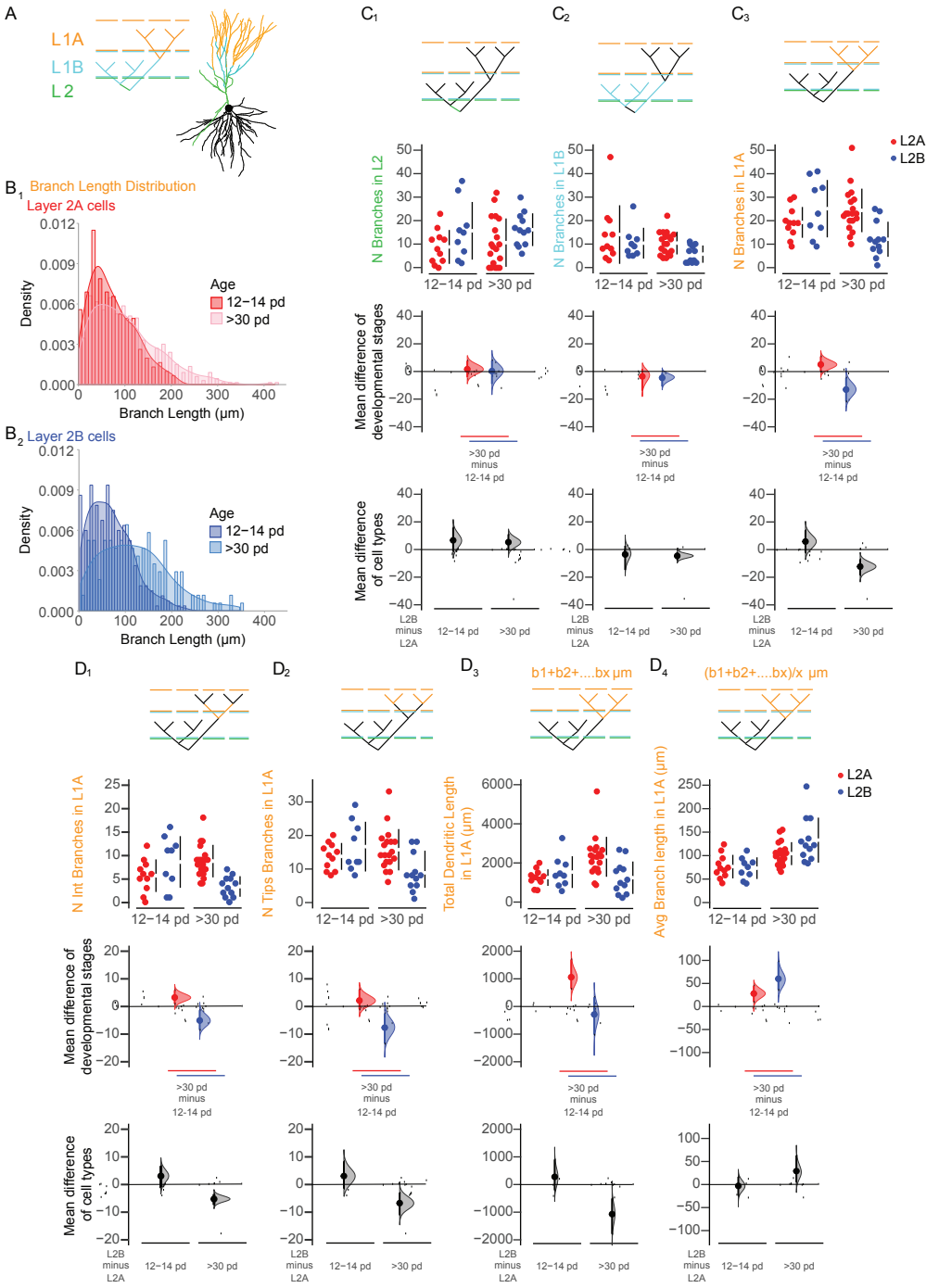

Figure 7: Input specific pruning in apical dendrites of layer 2A and layer 2B neurons. (A) Visual representation of a layer 2B neuron showing apical dendrites classification into three categories: branches terminating in layer 2 (L2, green), layer 1B (L1B, cyan) and layer 1A (L1A, orange). (B) Densities of the distributions of layer 1A branches for layer 2A (B1) and layer 2B (B2) neurons are displayed as a function of the branch length at two time intervals: 12-14 pd (L2A red and L2B blue) and >30 pd (L2A pink and L2B light blue). (C-D) Morphologic parameters used to describe pruning of apical dendrites of Layer 2A (red) and layer 2B (blue) neurons at two different time ranges (expressed as postnatal days, pd): total number of apical branches terminating in L2 (C1), L1B (C2) and L1A (C3), total number of apical intermediate branches (D1) and tips (D2) terminating in L1A and total dendritic length (D3) and average branch length (D4) of apical branches terminating in L1A. These parameters are shown in Cumming estimation plots, the raw data are plotted on the upper axes; mean differences between developmental stages are plotted on the middle axes and mean differences between the cell types are plotted on the lower axes, as a bootstrap sampling distribution. Mean differences are depicted as dots and the 95% confidence intervals are indicated by the ends of the vertical error bars. Figure modified from (Moreno-Velasquez et al. 2020).

In growth phase 3, pruning of branches was observed between the second and fifth postnatal week, which correspond to the critical period for plasticity of sensory synapses (Franks and Isaacson 2005, Poo and Isaacson 2007). Therefore, this pruning could be affected by the different synaptic inputs received in layer 1 of the aPCx. Apical dendrites of layer 2 neurons receive compartmentalized sensory and associational inputs in layer 1A and layer 1B/2 respectively (Johenning et al. 2009, Bekkers and Suzuki 2013). Apical dendritic pruning was then examined according to the position of the branches in layer 1 and 2. Apical dendrites of the two cell types were classified as branches terminating in layer 1A receiving sensory inputs and branches terminating in layer 1B and layer 2, both receiving recurrent inputs (Fig 7A). Calretinin and DAPI stainings were used to delineate layer 1A/1B and layer 2 (Fig 2).

Apical branches of both layer 2A and 2B neurons receiving associational inputs in layer 1B and layer 2 do not show any significant reduction during this critical period (Fig 7C1 and 7C2) even though basal branches of layer 2B neurons display some pruning (Fig 5B and 5C). Only branches of layer 2B neurons receiving sensory inputs prune between the second and fifth postnatal week; contrary to layer 2A neurons which remain stable (Fig 7C3). This suggests that pruning is limited to a specific circuit (sensory circuit) in a subpopulation of neurons in the aPCx.

Layer 2B dendrites terminating in layer 1A present significant reduction in the number of intermediate branches (Fig 7D1) and tips (Fig 7D2). However, these branches do not show significant pruning in their TDBL (Fig 7D3), instead they show an increase in their individual BL (Fig 7D4).

Changes in the distribution of average BL during the critical period help to better understand the differences in the pruning of the two cell types (Fig 7B). Both layer 2A and 2B neurons show a shift toward longer branches terminating in layer 1A; however, layer 2A neurons do not present any branch loss and therefore this shift could be simply explained by branch elongation (Fig 7D4). On the other hand, layer 2B neurons show a decrease of branches terminating in layer 1A and thus, the shift in the BL distribution could only be explained by the pruning of shorter branches tending to disappear and elongation of longer surviving branches or survival of longer branches.

7.5 Network implementation of the two cell types reflects morphological differences

It has been shown in different studies that the development and stability of dendritic arborizations are strictly related to neuronal activity (Wong and Ghosh 2002, Cline 2001, McAllister 2000). It was also shown in the previous enumerate that the dendritic developmental growth phase one, consisting of the determination of branch complexity, is concluded after the first postnatal weeks for layer 2A and 2B neurons in the aPCx (Fig 5 and 6). Thus, in order to understand the differences in the network implementation of the two cell types, patterns of neuronal activity of layer 2A and 2B neurons were compared during the first postnatal week, fitting the time of branch complexity determination. For this, Ca^{2+} imaging was performed in slices of Ai95-NexCre mice expressing GCaMP6F exclusively in glutamatergic neurons (Fig 8A) and SamuROI software was used to analyzed spontaneous population imaging of layer 2 neurons in the aPCx (Fig 8B). First of all, all visible neurons were identified (4755/50/39/23 neurons/fields of view/slices/mice) and events were defined as Ca^{2+}-mediated increases

of the fluorescence signals with respect to the baseline. Then, events were extracted from individual active cells and the percentage of layer 2 simultaneously coactive cells in the same field of view was calculated (Fig 8C).

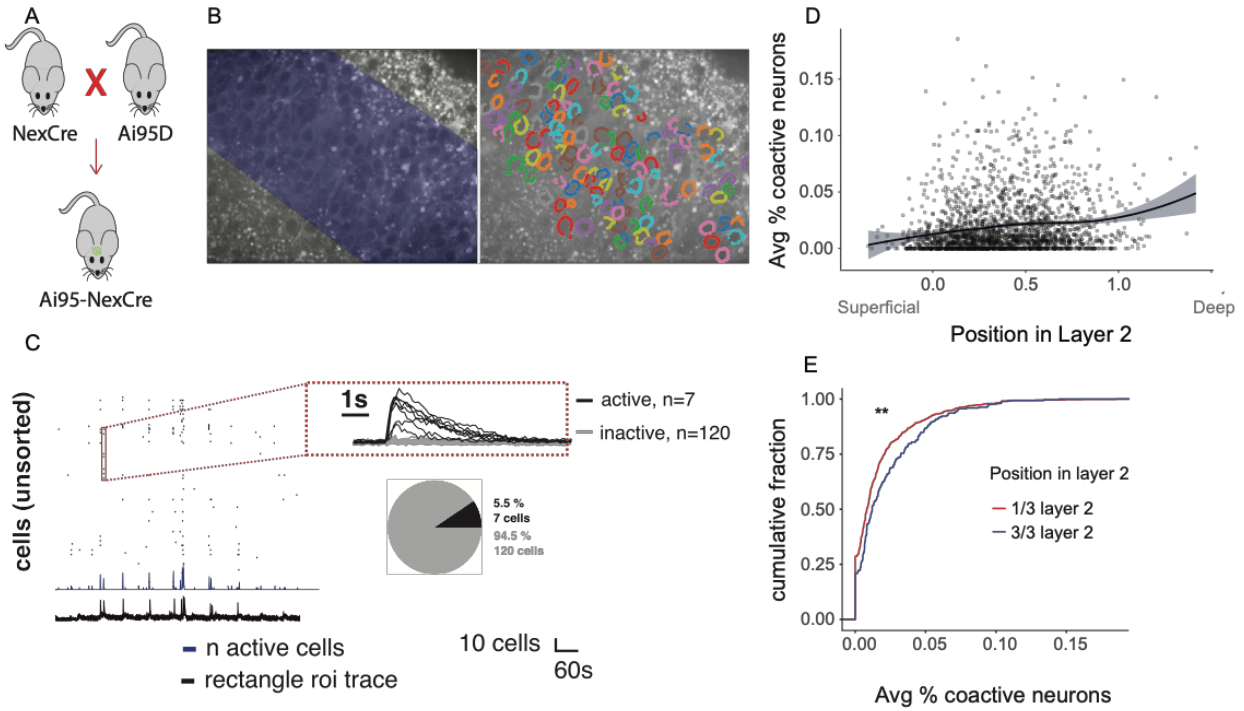

Figure 8: Network implementation of layer 2A and layer 2B neurons during early spontaneous events. (A) Schematic showing the genetic crossing used to obtain GCaMP6F expression in excitatory neurons. (B) Example of a baseline GCaMP-fluorescence image from an Ai95-NexCre mouse in layer 2 in the anterior piriform cortex (aPCx). Right image shows the rectangular region of interest (ROI) covering layer 2 for detecting global activity. Left image shows all detected neurons in layer 2. (C) Corresponding traces from global events measured from the ROI (black trace) and the active cells (blue) shown in the raster plot. The red inset shows fluorescent traces from individual neurons in the raster plot. The pie chart displays the proportion of active versus inactive cells for one event. (D) Average percentage of coactive neurons for each active neuron is plotted against the position of the active neuron in layer 2 in the aPCx. Data are measured from the first postnatal week and fitted with a local polynomial regression. (E) Cumulative distributions of the average percentage of coactive neurons from (D) are plotted for the most superficial third (red) and most deep third (blue) of layer 2 in aPCx (1/3 versus 3/3 layer 2: $p<0.01$ unpaired t-test). **: $p<0.01$. Figure modified from (Moreno-Velasquez et al. 2020).

Average of the percentage of coactive neurons over all events observed in a neuron were calculated and plotted against neuronal position in layer 2 of aPCx (Fig 8D). This plot shows that coactivity is significantly stronger in the deeper third of layer 2 compare to the more superficial third (Fig 8D and 8E), suggesting significantly higher coactivity for layer 2B neurons compared to layer 2A cells and therefore, higher local functional connectivity of these neurons. The higher functional connectivity of layer 2B neurons complies with the more complex morphology of its basal dendritic tree receiving more associational inputs (Haberly 1985, Wiegand et al. 2011).

These results show that differences in basal dendritic tree complexity between layer 2A and 2B neurons already evident after the first postnatal week are reflected by differences in their local functional connectivity during spontaneous network activity.

7.6 Mossy fibers in the Etruscan Shrew

The hippocampus is a crucial brain structure in the processes of learning and memory consolidation and has been tightly linked to the olfactory system, receiving strong and direct projections from it (Eichenbaum and Otto 1992). The DG receives the information from the olfactory system and transfers it to the CA3 hippocampal area through the mossy fiber (MF) pathway (Fig 9A) (Nicoll and Schmitz 2005).

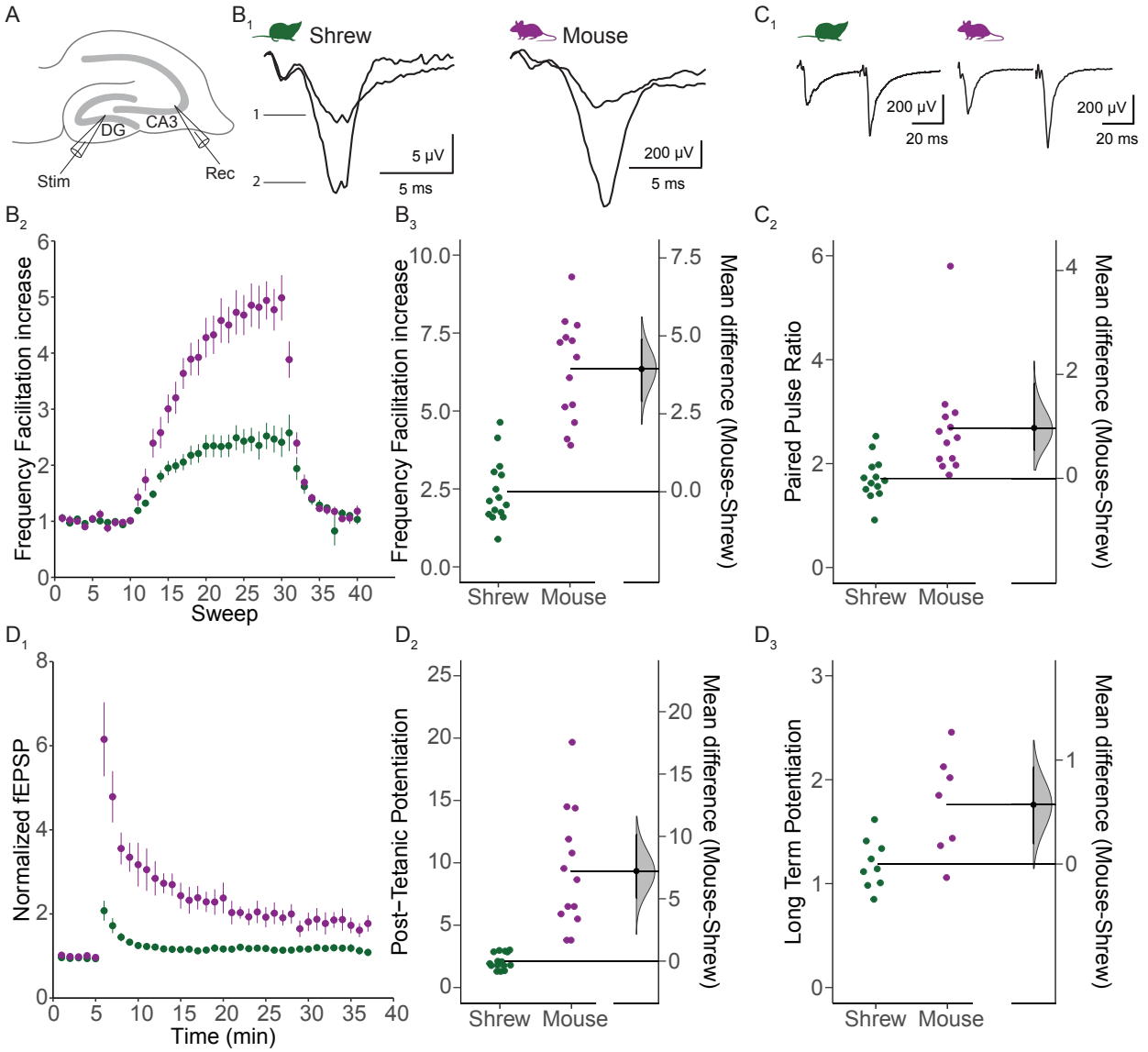

Figure 9: Synaptic plasticity of the mossy fiber (MF) synapse of the Etruscan shrew. (A) Visual representation of the experimental setup for MF recordings with the stimulation electrode in the granule cell layer of the dentate gyrus (DG) and the recording electrode in the stratum lucidum in the CA3 region. (B-D) Electrophysiological parameters used to evaluate plasticity of the MF in shrews (green) versus mice (purple). (B) Frequency facilitation (FF) exemplary traces (B1) of the first (1) and last (2) MF fEPSP evoked by a train of 20 stimuli at 1 Hz, followed by the FF increase in every sweep (B2) and explicitly during at the 20th stimuli (B3) in shrews and mice; values normalized to the baseline. (C) Paired pulse ratio (PPR) exemplary traces (C1) and values of the radio of the second fEPSP to the first one at 20 Hz (C2) in shrews and mice. Finally, long-term potentiation (LTP) time plot (D1) followed by post-tetanic potentiation (D2), measured the first minute after the induction protocol, and the LTP values analyzed 30 min after LTP induction (D3) for both shrews and mice; values normalized to the baseline. Mean differences between species are shown in Cumming estimation plots. The raw data are plotted on the left axes and mean differences between species are plotted on the right axes as a bootstrap sampling distribution. Mean differences are depicted as dots and the 95% confidence intervals are indicated by the ends of the vertical error bars. Figure modified from (Beed et al. 2020).

The MF pathway is often studied in neurosciences, particularly for its unusual synaptic plasticity which includes low basal release probability, high frequency facilitation and absence of N-methyl-D aspartate (NMDA) receptor in the induction of long-term potentiation (LTP) (Nicoll and Schmitz 2005). In addition, the MF synapse can be specifically identified using functional and pharmacological properties. This ability to clearly delineate and identify the MF pathway is analogous to sensory and associative pathways in the aPCx. This makes it an ideal candidate for a comparative study, this time between species.

According to this, in this study, differences in synaptic transmission and plasticity in the MF pathway were further investigated in the Etruscan shrew in comparison to mice. The hippocampus anatomy is similar in shrews in comparison to other mammalian species, with clear structures like DG and CA3, CA2 and CA1 areas (Naumann et al. 2012). However, shrews are the smallest mammals with clearly identifiably hippocampal structures, which makes them ideal candidates for studying questions related to scaling. Here, fEPSP were elicited in the DG and recorded in CA3 hippocampal area from 400 µm shrew brain slices (Fig 9A).

In order to classify the MF signals, short-term plasticity (STP) was first assessed. STP parameters were found to be significantly lower in the shrews compared to mice, indicating a reduced STP for these animals: FF (Fig 9B), PPR (Fig 9C) and PTP (Fig 9D2). Finally, LTP was also analyzed: shrews showed a significant LTP increase of around 19% in relation to the baseline. This increase in potentiation was significantly lower compared to mice (76%) (Fig 9D). All together, these results show much less plasticity in the shrew MF compared to the mice although the relative convergence ratio of MF inputs in CA3 was higher for this species (Beed et al. 2020). These changes at the MF synapses show specific adaptation of neuronal circuits across species and suggest different involvement of these synapses related to the scaling of brain size and the behavioral outcome.

8. Discussion

Until now, the adult aPCx has been well characterized: It is a three layered paleocortex containing densely packed in layer 2 principal excitatory neurons sampling sensory and associational inputs. Sensory inputs coming via the LOT are restricted to the most superficial part of layer 1 (layer 1A), while recurrent inputs from within aPCx and other brain regions are sampled in layer 1B, layer 2 and layer 3. Layer 2, in turn, is divided into two sublayers along the vertical axis (layer 2A and layer 2B) and its neurons are classified into semilunar and superficial pyramidal cells, with strikingly morphological, electrophysiological and functional differences (Choy et al. 2015, Suzuki and Bekkers 2006). In contrast, development and maturation of this cortex is less studied and little is known regarding the emergence of the differences between the two cell types. Here, detailed morphometric and functional analysis was performed in the aPCx, including morphological development of the two neuron types and their involvement in the sensory and associational circuits.

The first challenge faced during this study was the identification of the aPCx and consistent classification of layer 2 neurons throughout development. Calretinin staining was used to localize and delineate aPCx by labeling the LOT in layer 1A (Fig 1A1 and Fig 2A2) and DAPI staining outline layer 2 from the very first days after birth (Fig 2A3). Then, cells were sampled and recorded from the whole extension of the aPCx and the classification was done afterwards based on the location of these neurons in layer 2 according to the post-hoc staining.

Additional to the well-known classification of the two cell types in layer 2 of the aPCx, a gradient of these cells has been described in the vertical axis with respect to their morphology and electrophysiology (Suzuki and Bekkers 2011, Wiegand et al. 2011). In this study, the morphology and electrophysiology of the recorded neurons support the idea of the vertical gradient. On the one hand, intrinsic electrophysiological properties observed here were more homogeneous between layer 2A and layer 2B neurons, which disagreed with previous studies (Suzuki and Bekkers 2006, Suzuki and Bekkers 2011, Wiegand et al. 2011). Electrophysiological data was compared during and after the critical period for plasticity of sensory synapses. Parameters measured at 12-14 pd best matched observations previously reported. However, even when there was a similar trend in the differences between the two cells in input resistances and the action potential thresholds; resting potential and instant firing frequencies of the two neurons were very similar, differing to what was shown before (Fig 4). This inconsistency could be explained by two main reasons: (1) in this study, sampling was done differently from published results. Here the whole extent of layer 2 was covered including vertical and horizontal axes, whereas previous studies focused on the very superficial or very deep cells in the vertical axis of layer 2. Additionally, coronal slices are normally used while here horizontal slices were prepared, and this change in slicing could influence the sampling in the rostro caudal axis. Finally, (2) the use of a different intracellular solution could cause dissimilarities in intrinsic properties of the neurons. Here, k-gluconate-based intra was used as opposed to the previously used KMESO4-based intra, which could influence changes in input resistance, threshold, AHP and in consequence, changes in the burstiness of the neurons (Kaczorowski, Disterhoft, and Spruston 2007, Zhang et al. 1994).

On the other hand, the segregation based on the location of the neurons in layer 2 exposed morphological differences between the basal dendritic tree of the two cell types:

layer 2A neurons having a shorter or even absent basal arbor and layer 2B a basal dendritic tree more complex and extended (Fig 3). Therefore, location of the cells and basal dendritic complexity were sufficiently robust parameters for differentiating between the two neuronal types.

Next, the main aim of this study was to describe the developmental dendritic growth of layer 2 neurons in the aPCX and to identify the emergence of the differences between the two cell subtypes. Here, detailed morphometric analysis of the arborizations at four different time windows over development was performed to identify a growth timeline divided in three phases: (1) determination of branch complexity, (2) branch elongation and (3) branch pruning. Growth phase one was reflected in the addition of new branches and was completed for basal and apical dendrites after the first postnatal week. Differences in arborizations between layer 2A and layer 2B cells were evident already since this first developmental phase. Especially, basal dendrites showed higher complexity in layer 2B neurons compared to layer 2A already from birth, exposing then the dissimilarities of the two cell types regarding their implementation in the associational circuit.

SamuROI software was successfully developed and used to further recognize the diverse network implementation of the two neurons by analyzing their spontaneous neuronal activity during the first postnatal week of branch complexity determination. Ca^{2+} imaging of layer 2 cells in the aPCx showed higher functional connectivity of layer 2B neurons compared to layer 2A. This increase in coactivity matches with the higher complexity of basal dendrites of layer 2B cells confirming the involvement of these neurons in the recurrent circuit, unlike layer 2A cells that receive exclusively sensory inputs (Haberly 1985, Wiegand et al. 2011, Bekkers and Suzuki 2013).

Growth phase two consisted of the elongation of the dendritic trees and it was accomplished by layer 2B neurons at the end of the second postnatal week and by layer 2A neurons at the end of the fifth postnatal week for both basal and apical dendritic trees. Finally, growth phase 3 showed as well major differences between the two cell types. Pruning was exclusive for layer 2B neurons and selective for apical dendrites receiving layer 1A sensory inputs (Fig 7). It was evidently biased towards shorter branches and it was accompanied by an elongation of longer surviving branches or a preselection of longer surviving branches. Additionally, it happened during the critical period for plasticity of sensory inputs previously described (Poo and Isaacson 2007, Franks and Isaacson 2005). Interestingly, it has been shown that layer 2B neurons displayed NMDA-dependent supralinear dendritic integration of sensory inputs in layer 1A branches, meaning that clustered sensory inputs trigger NMDA-spikes, contrary to distributed inputs of similar strength (Kumar et al. 2018). Clustering spatially refers to distribution on the same dendritic branch, therefore longer branches have a higher probability for NMDA-spike generation. Furthermore, this supralinear integration of sensory inputs was observed during developmental period of dendritic pruning of layer 2B neurons (Moreno-Velasquez et al. 2020), supporting the survival and further elongation of longer apical branches in layer 1A. In contrast, layer 2A neurons do not show supralinear integration of inputs (Moreno-Velasquez et al. 2020) nor pruning, but they do displayed a larger apical dendritic tree in layer 1A of the aPCx (Fig 7), which fits the description of their stronger incorporation into sensory circuits (Bekkers and Suzuki 2013, Wiegand et al. 2011).

This thesis is based on a comparative approach with the overarching goal to describe how neuronal circuits differ at distinct scales. While we compared the developmental growth of different types of neurons with distinct circuit incorporation in the aPCx at different developmental ages representing different brain sizes, we now switch to a comparison of a hippocampal synaptic circuit in differently sized species. For this part of the thesis, synaptic plasticity in the MF pathway of the hippocampus in shrews was investigated and compared to a dataset from mice. The underlying question was whether synaptic properties differ at different scales, with the shrew being the smallest mammal with a preserved hippocampal structure (Naumann et al. 2012). While the hippocampus is not a primary olfactory area like the aPCx, the olfactory system projects strongly onto the hippocampus and it is closely associated to it. Hippocampal circuits play an important role in odor-guided learning and in turn, olfactory inputs influence the physiological activity of the hippocampus (Eichenbaum and Otto 1992). Then, the olfactory-hippocampal pathway could be very useful for the study of higher order coding of sensory information. However, in this study, the hippocampus was studied in isolation with not direct link to the olfactory-hippocampal inputs. In summary, shrews displayed lower short and long-term potentiation at the MF synapse compared to mice, even though the basic layout of the hippocampus was conserved (Beed et al. 2020). Interestingly, it was found that shrews show lower expression of the protein synaptotagmin 7 (Syt7) in the MF pathway (Beed et al. 2020). Syt7 is a calcium sensor required for facilitation at different synapses (Jackman et al. 2016) and the lower expression of this protein in the MF may contribute to the physiological differences seen in synaptic plasticity.

In conclusion, this thesis presented comparative data demonstrating brain-size related circuit-specific differences in dendritic structure and function of layer 2 neurons in the aPCX during brain growth and brain-size related differences of the functional properties of the hippocampal mossy fiber in differently sized species. Here, a first description of circuit-specific differences in dendritic development of the different subtypes of neurons in layer 2 of the aPCX is postulated. Layer 2A and layer 2B neurons differ in their morphology and in their developmental trajectories and these changes are associated with their specific integration to sensory and recurrent circuits. We hope this study serves as the basis for future research involving for instance neurodevelopmental studies of pathological conditions such as autism. Regarding the shrew data, future work will have to examine how the functional differences at the level of hippocampal MF signaling relate to differences in the behavioral repertoire of shrews and mice.

9. References

Bathellier, B., T. W. Margrie, and M. E. Larkum. 2009. “Properties of Piriform Cortex Pyramidal Cell Dendrites: Implications for Olfactory Circuit Design.” *Journal of Neuroscience* 29 (40): 12641–52. https://doi.org/10.1523/JNEUROSCI.1124-09.2009.

Beed, Prateep, Saikat Ray, Laura Moreno Velasquez, Alexander Stumpf, Daniel Parthier, Aarti Swaminathan, Noam Nitzan, Jörg Breustedt, Liora Las, Michael Brecht and Dietmar Schmitz. 2020. “Species-Specific Differences in Synaptic Transmission and Plasticity.” *Scientific Reports* 10 (1): 16557. https://doi.org/10.1038/s41598-020-73547-6.

Bekkers, John M., and Norimitsu Suzuki. 2013. “Neurons and Circuits for Odor Processing in the Piriform Cortex.” *Trends in Neurosciences* 36 (7): 429–38. https://doi.org/10.1016/j.tins.2013.04.005.

Bolding, Kevin A, Shivathmihai Nagappan, Bao-Xia Han, Fan Wang, and Kevin M Franks. 2020. “Recurrent Circuitry Is Required to Stabilize Piriform Cortex Odor Representations across Brain States.” *ELife* 9 (July): e53125. https://doi.org/10.7554/eLife.53125.

Choy, Julian M.C., Norimitsu Suzuki, Yasuyuki Shima, Timotheus Budisantoso, Sacha B. Nelson, and John M. Bekkers. 2015. “Optogenetic Mapping of Intracortical Circuits Originating from Semilunar Cells in the Piriform Cortex.” *Cerebral Cortex*, October, bhv258. https://doi.org/10.1093/cercor/bhv258.

Cline, Hollis T. 2001. “Dendritic Arbor Development and Synaptogenesis.” *Current Opinion in Neurobiology* 11 (1): 118–26. https://doi.org/10.1016/S0959-4388(00)00182-3.

Diodato, Assunta, Marion Ruinart de Brimont, Yeong Shin Yim, Nicolas Derian, Sandrine Perrin, Juliette Pouch, David Klatzmann, Sonia Garel, Gloria B Choi, and Alexander Fleischmann. 2016. “Molecular Signatures of Neural Connectivity in the Olfactory Cortex.” *Nature Communications* 7 (1): 12238. https://doi.org/10.1038/ncomms12238.

Dong, Xintong, Kang Shen, and Hannes E. Bülow. 2015. “Intrinsic and Extrinsic Mechanisms of Dendritic Morphogenesis.” *Annual Review of Physiology* 77 (1): 271–300. https://doi.org/10.1146/annurev-physiol-021014-071746.

Eichenbaum, Howard, and Tim Otto. 1992. “The Hippocampus and the Sense of Smell.” In *Chemical Signals in Vertebrates 6*, edited by Richard L. Doty and Dietland Müller-Schwarze, 67–77. Boston, MA: Springer US. https://doi.org/10.1007/978-1-4757-9655-1_12.

Feng, Linqing, Ting Zhao, and Jinhyun Kim. 2015. “NeuTube 1.0: A New Design for Efficient Neuron Reconstruction Software Based on the SWC Format.” *Eneuro* 2 (1): ENEURO.0049-14.2014. https://doi.org/10.1523/ENEURO.0049-14.2014.

Franks, Kevin M., and Jeffry S. Isaacson. 2005. “Synapse-Specific Downregulation of NMDA Receptors by Early Experience: A Critical Period for Plasticity of Sensory Input to Olfactory Cortex.” *Neuron* 47 (1): 101–14. https://doi.org/10.1016/j.neuron.2005.05.024.

Franks, Kevin M., Marco J. Russo, Dara L. Sosulski, Abigail A. Mulligan, Steven A. Siegelbaum, and Richard Axel. 2011. “Recurrent Circuitry Dynamically Shapes the Activation of Piriform Cortex.” *Neuron* 72 (1): 49–56. https://doi.org/10.1016/j.neuron.2011.08.020.

Gamma, E, R Helm, R Johnson, and J Vlissides. 2015. *Design Patterns: Elements of Reusable Object-Oriented Software*. Boston, MA: Addison-Wesley Longman

Publishing Co., Inc.
Goebbels, Sandra, Ingo Bormuth, Ulli Bode, Ola Hermanson, Markus H. Schwab, and Klaus-Armin Nave. 2006. “Genetic Targeting of Principal Neurons in Neocortex and Hippocampus of NEX-Cre Mice.” *Genesis* 44 (12): 611–21. https://doi.org/10.1002/dvg.20256.
Guzman, Segundo Jose, Alois Schlögl, Michael Frotscher, and Peter Jonas. 2016. “Synaptic Mechanisms of Pattern Completion in the Hippocampal CA3 Network.” *Science* 353 (6304): 1117. https://doi.org/10.1126/science.aaf1836.
Haberly, Lewis B. 1985. “Neuronal Circuitry in Olfactory Cortex: Anatomy and Functional Implications.” *Chemical Senses* 10 (2): 219–38. https://doi.org/10.1093/chemse/10.2.219.
Ho, Joses, Tayfun Tumkaya, Sameer Aryal, Hyungwon Choi, and Adam Claridge-Chang. 2019. “Moving beyond P Values: Data Analysis with Estimation Graphics.” *Nature Methods* 16 (7): 565–66. https://doi.org/10.1038/s41592-019-0470-3.
Jackman, Skyler L., Josef Turecek, Justine E. Belinsky, and Wade G. Regehr. 2016. “The Calcium Sensor Synaptotagmin 7 Is Required for Synaptic Facilitation.” *Nature* 529 (7584): 88–91. https://doi.org/10.1038/nature16507.
Johenning, F. W., P. S. Beed, T. Trimbuch, M. H. K. Bendels, J. Winterer, and D. Schmitz. 2009. “Dendritic Compartment and Neuronal Output Mode Determine Pathway-Specific Long-Term Potentiation in the Piriform Cortex.” *Journal of Neuroscience* 29 (43): 13649–61. https://doi.org/10.1523/JNEUROSCI.2672-09.2009.
Kaczorowski, Catherine Cook, John Disterhoft, and Nelson Spruston. 2007. “Stability and Plasticity of Intrinsic Membrane Properties in Hippocampal CA1 Pyramidal Neurons: Effects of Internal Anions: Stability and Plasticity of Membrane Properties in CA1 Pyramidal Neurons.” *The Journal of Physiology* 578 (3): 799–818. https://doi.org/10.1113/jphysiol.2006.124586.
Kamiya, H, H Shinozaki, and C Yamamoto. 1996. “Activation of Metabotropic Glutamate Receptor Type 2/3 Suppresses Transmission at Rat Hippocampal Mossy Fibre Synapses.” *The Journal of Physiology* 493 (2): 447–55. https://doi.org/10.1113/jphysiol.1996.sp021395.
Kumar, Amit, Oded Schiff, Edi Barkai, Bartlett W Mel, Alon Poleg-Polsky, and Jackie Schiller. 2018. “NMDA Spikes Mediate Amplification of Inputs in the Rat Piriform Cortex.” *ELife* 7 (December): e38446. https://doi.org/10.7554/eLife.38446.
Lanoue, Vanessa, and Helen M. Cooper. 2019. “Branching Mechanisms Shaping Dendrite Architecture.” *Developmental Biology* 451 (1): 16–24. https://doi.org/10.1016/j.ydbio.2018.12.005.
Madisen, Linda, Aleena R. Garner, Daisuke Shimaoka, Amy S. Chuong, Nathan C. Klapoetke, Lu Li, Alexander van der Bourg, Yusuke Niino, Ladan Egolf, Claudio Monetti, Hong Gu, Maya Mills, Adrian Cheng, Bosiljka Tasic, Thuc Nghi Nguyen, Susan M Sunkin, Andrea Benucci, Andras Nagy, Atsushi Miyawaki, Frijof Helmchen, Ruth M Empson, Thomas Knöpfel, Edward S. Boyden, R. Clay Reid, Matteo Carandini and Hongkui Zeng. 2015. “Transgenic Mice for Intersectional Targeting of Neural Sensors and Effectors with High Specificity and Performance.” *Neuron* 85 (5): 942–58. https://doi.org/10.1016/j.neuron.2015.02.022.
Markopoulos, F., F.B. Neubauer, T. Berger, and A.L. Scotti. 2008. “Reassembling a System from the Sensor to Cerebral Representation: The Olfactory System in Vitro.” *Neuroscience* 156 (4): 1048–63. https://doi.org/10.1016/j.neuroscience.2008.07.071.
Martin-Lopez, Eduardo, Kimiko Ishiguro, and Charles A Greer. 2019. “The Laminar Organization of Piriform Cortex Follows a Selective Developmental and Migratory

Program Established by Cell Lineage." *Cerebral Cortex* 29 (1): 1–16. https://doi.org/10.1093/cercor/bhx291.
McAllister, A. K. 2000. "Cellular and Molecular Mechanisms of Dendrite Growth." *Cerebral Cortex* 10 (10): 963–73. https://doi.org/10.1093/cercor/10.10.963.
Moreno-Velasquez, Laura, Hung Lo, Stephen Lenzi, Malte Kaehne, Jörg Breustedt, Dietmar Schmitz, Sten Rüdiger, and Friedrich W. Johenning. 2020. "Circuit-Specific Dendritic Development in the Piriform Cortex." *Eneuro* 7 (3): ENEURO.0083-20.2020. https://doi.org/10.1523/ENEURO.0083-20.2020.
Naumann, R.K., F. Anjum, C. Roth-Alpermann, and M. Brecht. 2012. "Cytoarchitecture, Areas, and Neuron Numbers of the Etruscan Shrew Cortex." *The Journal of Comparative Neurology* 520 (11): 2512–30. https://doi.org/10.1002/cne.23053.
Neville, Kr, and Lb Haberly. 2004. "Olfactory Cortex." In *The Synaptic Organization of the Brain*, 5th ed., 415–54. Oxford University Press. https://doi.org/10.1093/acprof:oso/9780195159561.001.1.
Nicoll, Roger A., and Dietmar Schmitz. 2005. "Synaptic Plasticity at Hippocampal Mossy Fibre Synapses." *Nature Reviews Neuroscience* 6 (11): 863–76. https://doi.org/10.1038/nrn1786.
Pachitariu, Marius, Carsen Stringer, Mario Dipoppa, Sylvia Schröder, L. Federico Rossi, Henry Dalgleish, Matteo Carandini, and Kenneth D. Harris. 2016. "Suite2p: Beyond 10,000 Neurons with Standard Two-Photon Microscopy." Preprint. Neuroscience. https://doi.org/10.1101/061507.
Poo, C., and J. S. Isaacson. 2007. "An Early Critical Period for Long-Term Plasticity and Structural Modification of Sensory Synapses in Olfactory Cortex." *Journal of Neuroscience* 27 (28): 7553–58. https://doi.org/10.1523/JNEUROSCI.1786-07.2007.
Rueckl, Martin, Stephen C. Lenzi, Laura Moreno-Velasquez, Daniel Parthier, Dietmar Schmitz, Sten Ruediger, and Friedrich W. Johenning. 2017. "SamuROI, a Python-Based Software Tool for Visualization and Analysis of Dynamic Time Series Imaging at Multiple Spatial Scales." *Frontiers in Neuroinformatics* 11 (June): 44. https://doi.org/10.3389/fninf.2017.00044.
Sarma, A. A., M. B. Richard, and C. A. Greer. 2011. "Developmental Dynamics of Piriform Cortex." *Cerebral Cortex* 21 (6): 1231–45. https://doi.org/10.1093/cercor/bhq199.
Scorcioni, Ruggero, Sridevi Polavaram, and Giorgio A Ascoli. 2008. "L-Measure: A Web-Accessible Tool for the Analysis, Comparison and Search of Digital Reconstructions of Neuronal Morphologies." *Nature Protocols* 3 (5): 866–76. https://doi.org/10.1038/nprot.2008.51.
Sommer, Christoph, Christoph Straehle, Ullrich Kothe, and Fred A. Hamprecht. 2011. "Ilastik: Interactive Learning and Segmentation Toolkit." In *2011 IEEE International Symposium on Biomedical Imaging: From Nano to Macro*, 230–33. Chicago, IL, USA: IEEE. https://doi.org/10.1109/ISBI.2011.5872394.
Srinivasan, Shyam, and Charles F. Stevens. 2018. "The Distributed Circuit within the Piriform Cortex Makes Odor Discrimination Robust." *Journal of Comparative Neurology* 526 (17): 2725–43. https://doi.org/10.1002/cne.24492.
Suzuki, N., and J. M. Bekkers. 2006. "Neural Coding by Two Classes of Principal Cells in the Mouse Piriform Cortex." *Journal of Neuroscience* 26 (46): 11938–47. https://doi.org/10.1523/JNEUROSCI.3473-06.2006.
Suzuki, N., and J. M. Bekkers. 2011. "Two Layers of Synaptic Processing by Principal Neurons in Piriform Cortex." *Journal of Neuroscience* 31 (6): 2156–66. https://doi.org/10.1523/JNEUROSCI.5430-10.2011.
Torben-Nielsen, Benjamin. 2014. "An Efficient and Extendable Python Library to Analyze

Neuronal Morphologies." *Neuroinformatics* 12 (4): 619–22. https://doi.org/10.1007/s12021-014-9232-7.
Wiegand, H. F., P. Beed, M. H. K. Bendels, C. Leibold, D. Schmitz, and F. W. Johenning. 2011. "Complementary Sensory and Associative Microcircuitry in Primary Olfactory Cortex." *Journal of Neuroscience* 31 (34): 12149–58. https://doi.org/10.1523/JNEUROSCI.0285-11.2011.
Wilson, Donald A., and Regina M. Sullivan. 2011. "Cortical Processing of Odor Objects." *Neuron* 72 (4): 506–19. https://doi.org/10.1016/j.neuron.2011.10.027.
Wong, Rachel O. L., and Anirvan Ghosh. 2002. "Activity-Dependent Regulation of Dendritic Growth and Patterning." *Nature Reviews Neuroscience* 3 (10): 803–12. https://doi.org/10.1038/nrn941.
Woods, Nicholas I., Fabio Stefanini, Daniel L. Apodaca-Montano, Isabelle M.C. Tan, Jeremy S. Biane, and Mazen A. Kheirbek. 2020. "The Dentate Gyrus Classifies Cortical Representations of Learned Stimuli." *Neuron* 107 (1): 173-184.e6. https://doi.org/10.1016/j.neuron.2020.04.002.
Zhang, L., J. L. Weiner, T. A. Valiante, A. A. Velumian, P. L. Watson, S. S. Jahromi, S. Schertzer, P. Pennefather, and P. L. Carlen. 1994. "Whole-Cell Recording of the Ca2+-Dependent Slow Afterhyperpolarization in Hippocampal Neurones: Effects of Internally Applied Anions." *Pfluegers Archiv European Journal of Physiology* 426 (3–4): 247–53. https://doi.org/10.1007/BF00374778.

10. Statutory Declaration

"I, Laura Moreno Velasquez, by personally signing this document in lieu of an oath, hereby affirm that I prepared the submitted dissertation on the topic *'Developmental and interspecies comparison of morphology and plasticity in neuronal circuits involved in olfactory information processing' / ' Entwicklungsbiologischer und Interspezies Vergleich von Morphologie und Plastizität in neuronalen Netzwerken des Geruchssystems'*, independently and without the support of third parties, and that I used no other sources and aids than those stated.

All parts which are based on the publications or presentations of other authors, either in letter or in spirit, are specified as such in accordance with the citing guidelines. The sections on methodology (in particular regarding practical work, laboratory regulations, statistical processing) and results (in particular regarding figures, charts and tables) are exclusively my responsibility.

Furthermore, I declare that I have correctly marked all of the data, the analyses, and the conclusions generated from data obtained in collaboration with other persons, and that I have correctly marked my own contribution and the contributions of other persons (cf. declaration of contribution). I have correctly marked all texts or parts of texts that were generated in collaboration with other persons.

My contributions to any publications to this dissertation correspond to those stated in the below joint declaration made together with the supervisor. All publications created within the scope of the dissertation comply with the guidelines of the ICMJE (International Committee of Medical Journal Editors; www.icmje.org) on authorship. In addition, I declare that I shall comply with the regulations of Charité – Universitätsmedizin Berlin on ensuring good scientific practice.

I declare that I have not yet submitted this dissertation in identical or similar form to another Faculty.

The significance of this statutory declaration and the consequences of a false statutory declaration under criminal law (Sections 156, 161 of the German Criminal Code) are known to me."

Date Signature

11. Declaration of own contribution

Laura Moreno Velasquez contributed the following to the below listed publications:

Publication 1: Moreno-Velasquez, Laura, Hung Lo, Stephen Lenzi, Malte Kaehne, Jörg Breustedt, Dietmar Schmitz, Sten Rüdiger, and Friedrich W. Johenning. "Circuit-Specific Dendritic Development in the Piriform Cortex". *Eneuro*. 2020.

Contribution in detail:

Planning and design of the experiments:

Laura Moreno Velasquez, Hung Lo, Stephen Lenzi, Malte Kaehne, Jörg Breustedt, Dietmar Schmitz, Sten Rüdiger and Friedrich Johenning

Execution of experiments:

Laura Moreno Velasquez, Hung Lo, Stephen Lenzi and Malte Kaehne.

Data Analysis:

Laura Moreno Velasquez, Hung Lo, Stephen Lenzi, Malte Kaehne, Sten Rüdiger and Friedrich Johenning.

Figure preparation:

Laura Moreno Velasquez, Hung Lo, Stephen Lenzi, Malte Kaehne and Friedrich Johenning.

Writing and editing of the manuscript:

Writing done by Friedrich Johenning and editing by all the authors.

Detailed description of own contribution in publication 1:

Figure 1: Laura Moreno Velasquez performed the electrophysiological experiments, immunohistochemistry, confocal imaging, morphological reconstructions, data analysis and statistical evaluation.

Table 1: Laura Moreno Velasquez performed the electrophysiological experiments and statistical evaluation.

Figure 2 and 3: Laura Moreno Velasquez performed the morphological data processing and analysis with inputs from Friedrich Johenning.

Figure 4: Laura Moreno Velasquez prepared figure (from B to D) and performed the statistical analysis based on the data acquired and analyzed by Stephen Lenzi.

Figure 5: Laura Moreno Velasquez performed the morphological data processing and analysis with inputs from Friedrich Johenning.

Extended Data Figure 1-1: Laura Moreno Velasquez performed the statistical analysis.

Extended Data Table 1-1: Laura Moreno Velasquez performed the electrophysiological experiments, data analysis and statistical evaluation.

Extended data Table 1-2: Laura Moreno Velasquez performed statistical evaluation of Table 1 and all the figures, except figure 6.

Extended Data Figure 5-1: Laura Moreno Velasquez performed the morphological data processing and analysis with inputs from Friedrich Johenning.

Publication 2: Rueckl, Martin, Stephen C. Lenzi, Laura Moreno-Velasquez, Daniel Parthier, Dietmar Schmitz, Sten Ruediger, and Friedrich W. Johenning. “SamuROI, a Python-Based Software Tool for Visualization and Analysis of Dynamic Time Series Imaging at Multiple Spatial Scales”. *Frontiers in Neuroinformatics.* 2017.

Contribution in detail:

Planning and conceptualization of the software:
Friedrich Johennign, Martin Rueckl and Stephen Lenzi.

Code:
Martin Rueckl and Stephen Lenzi.

Design and validation of the software:
Friedrich Johenning, Laura Moreno Velasquez, Daniel Parthier, Stephen Lenzi, Martin Rueckl, Sten Ruediger and Dietmar Schmitz.

Exemplary data preparation:
Friedrich Johenning, Laura Moreno Velasquez, Daniel Parthier and Stephen Lenzi.

Writing and editing of the manuscript:
Friedrich Johenning, Stephen Lenzi, Martin Rueckl, Sten Ruediger and Dietmar Schmitz

Detailed description of own contribution in publication 2:
Laura Moreno Velasquez tested and validate the software in two different operating systems (Microsoft windows and Macintosh). Additionally, Laura Moreno Velasquez together with Daniel Parthier, performed the electrophysiological experiments and provided the imaging data for the preparation of figure 5: Macro-scale imaging example for using SamuROI on different cortical regions of a brain slice.

Publication 3: Beed, Prateep, Saikat Ray, Laura Moreno Velasquez, Alexander Stumpf, Daniel Parthier, Aarti Swaminathan, Noam Nitzan, Jörg Breustedt, Liora Las, Michael Brecht and Dietmar Schmitz. “Species-Specific Differences in Synaptic Transmission and Plasticity.” *Scientific Reports*. 2020

Contribution in detail:

Planning and design of the experiments:
Prateep Beed, Saikat Ray, Michael Brecht and Dietmar Schmitz.

Execution of experiments:
Prateep Beed, Saikat Ray, Laura Moreno Velasquez, Alexander Stumpf, Daniel Parthier, Aarti Swaminathan, Noam Nitzan and Liora Las.

Data Analysis:
Prateep Beed, Saikat Ray, Laura Moreno Velasquez, Alexander Stumpf and Jörg Breustedt.

Writing of the manuscript:

Prateep Beed, Saikat Ray, Michael Brecht and Dietmar Schmitz with inputs from all the authors

Detailed description of own contribution in publication 3:

Figure 1: Laura Moreno Velasquez and Prateep Beed performed the electrophysiological experiments on mossy fibers in shrews. Laura Moreno Velasquez analyzed the data and Prateep Beed performed the statistical analysis.

Figure S1: Laura Moreno Velasquez and Prateep Beed performed the electrophysiological experiments on mossy fibers in shrews. Laura Moreno Velasquez analyzed the data and Prateep Beed performed the statistical analysis.

Figure S2: Laura Moreno Velasquez, Alexander Stumpf and Prateep Beed performed the electrophysiological experiments. Laura Moreno Velasquez and Alexander Stumpf analyzed the data and Prateep Beed performed the statistical analysis.

_____

Signature, date and stamp of first supervising university professor / lecturer

_____

Signature of doctoral candidate

12. Journal Summary List (Open Access Journal Positive List): Publication 1

Open Access Journal Positive List

Contains biomedical open access journals that are listed on the Directory of Open Access Journals (DOAJ) and Pubmed Central.

Journal Data filtered by: Selected Categories: "**NEUROSCIENCES**". Total entries: 51 Journals

	Journal title	SCImago Journal Rank (SJR)	SJR Subject Category Quartile	Average time to publication (weeks)	Subject category	Subject category 2	Journal license	Publisher
	All			All	Neu ⊗	All		All
999	Translational Psychiatry	2.76	Q1	23	Neurosciences. Biological psychiatry. Neuropsychiatry		CC BY	Nature Publishing Group
1000	Frontiers in Synaptic Neuroscience	2.257	Q1	14	Neurosciences. Biological psychiatry. Neuropsychiatry		CC BY	Frontiers Media S.A.
1001	Social Cognitive and Affective Neuroscience	2.095	Q1	20	Neurosciences. Biological psychiatry. Neuropsychiatry	Consciousness. Cognition	CC BY, CC BY-NC, CC BY-NC-ND	Oxford University Press
1002	eNeuro	2.088	Q1	16	Neurosciences. Biological psychiatry. Neuropsychiatry		CC BY	Society for Neuroscience
1003	Frontiers in Systems Neuroscience	2.003	Q1	14	Neurosciences. Biological psychiatry. Neuropsychiatry		CC BY	Frontiers Media S.A.
1004	Frontiers in Neural Circuits	1.909	Q1	14	Neurosciences. Biological psychiatry. Neuropsychiatry		CC BY	Frontiers Media S.A.
1005	Frontiers in Molecular Neuroscience	1.851	Q1	14	Neurosciences. Biological psychiatry. Neuropsychiatry		CC BY	Frontiers Media S.A.
1006	Frontiers in Neuroanatomy	1.808	Q1	14	Neurosciences. Biological psychiatry. Neuropsychiatry	Human anatomy	CC BY	Frontiers Media S.A.
1007	Journal of Behavioral Addictions	1.767	Q1	20	Neurosciences. Biological psychiatry. Neuropsychiatry	Psychology	CC BY-NC	Akadémiai Kiadó
1008	Frontiers in Aging Neuroscience	1.635	Q1	14	Neurosciences. Biological psychiatry. Neuropsychiatry		CC BY	Frontiers Media S.A.

Open Access Journal Positive List

Contains biomedical open access journals that are listed on the Directory of Open Access Journals (DOAJ) and Pubmed Central.

		Journal title	SCImago Journal Rank (SJR)	SJR Subject Category Quartile	Average time to publication (weeks)	Subject category	Journal license	Publisher
1	999	Translational Psychiatry	2.76	Q1	23	Neurosciences. Biological psychiatry. Neuropsychiatry	CC BY	Nature Publishing Group
2	1000	Frontiers in Synaptic Neuroscience	2.257	Q1	14	Neurosciences. Biological psychiatry. Neuropsychiatry	CC BY	Frontiers Media S.A.
3	1001	Social Cognitive and Affective Neuroscience	2.095	Q1	20	Neurosciences. Biological psychiatry. Neuropsychiatry	CC BY, CC BY-NC, CC BY-NC-ND	Oxford University Press
4	1002	eNeuro	2.088	Q1	16	Neurosciences. Biological psychiatry. Neuropsychiatry	CC BY	Society for Neuroscience
5	1003	Frontiers in Systems Neuroscience	2.003	Q1	14	Neurosciences. Biological psychiatry. Neuropsychiatry	CC BY	Frontiers Media S.A.
6	1004	Frontiers in Neural Circuits	1.909	Q1	14	Neurosciences. Biological psychiatry. Neuropsychiatry	CC BY	Frontiers Media S.A.
7	1005	Frontiers in Molecular Neuroscience	1.851	Q1	14	Neurosciences. Biological psychiatry. Neuropsychiatry	CC BY	Frontiers Media S.A.
8	1006	Frontiers in Neuroanatomy	1.808	Q1	14	Neurosciences. Biological psychiatry. Neuropsychiatry	CC BY	Frontiers Media S.A.
9	1007	Journal of Behavioral Addictions	1.767	Q1	20	Neurosciences. Biological psychiatry. Neuropsychiatry	CC BY-NC	Akadémiai Kiadó
10	1008	Frontiers in Aging Neuroscience	1.635	Q1	14	Neurosciences. Biological psychiatry. Neuropsychiatry	CC BY	Frontiers Media S.A.
11	1009	Epidemiology and Psychiatric Sciences	1.63	Q1	8	Neurosciences. Biological psychiatry. Neuropsychiatry	CC BY, CC BY-NC-SA, CC BY-NC-ND	Cambridge University Press
12	1010	Frontiers in Cellular Neuroscience	1.618	Q2	14	Neurosciences. Biological psychiatry. Neuropsychiatry	CC BY	Frontiers Media S.A.
13	1011	Frontiers in Neuroscience	1.554	Q1	14	Neurosciences. Biological psychiatry. Neuropsychiatry	CC BY	Frontiers Media S.A.
14	1012	Journal of Neurodevelopmental Disorders	1.496	Q1	20	Neurosciences. Biological psychiatry. Neuropsychiatry	CC BY, CC0	BMC
15	1013	Neural Plasticity	1.422	Q1	16	Neurosciences. Biological psychiatry. Neuropsychiatry	CC BY	Hindawi Limited
16	1014	Network Neuroscience	1.42	Q1	16	Neurosciences. Biological psychiatry. Neuropsychiatry	CC BY	The MIT Press
17	1015	Frontiers in Neuroinformatics	1.377	Q1	14	Neurosciences. Biological psychiatry. Neuropsychiatry	CC BY	Frontiers Media S.A.
18	1016	International Journal of Bipolar Disorders	1.309	Q1	13	Neurosciences. Biological psychiatry. Neuropsychiatry	CC BY	SpringerOpen
19	1017	ASN Neuro	1.2	Q1	12	Neurosciences. Biological psychiatry. Neuropsychiatry	CC BY, CC BY-NC	SAGE Publishing
20	1018	Frontiers in Behavioral Neuroscience	1.199	Q1	14	Neurosciences. Biological psychiatry. Neuropsychiatry	CC BY	Frontiers Media S.A.
21	1019	International Journal of Methods in Psychiatric Research	1.148	Q1	18	Neurosciences. Biological psychiatry. Neuropsychiatry	CC BY-NC-ND	Wiley

22	1020	Journal of NeuroEngineering and Rehabilitation	1.139	Q1	32	Neurosciences. Biological psychiatry. Neuropsychiatry	CC BY, CC0	BMC
23	1021	Frontiers in Computational Neuroscience	1.041	Q2	14	Neurosciences. Biological psychiatry. Neuropsychiatry	CC BY	Frontiers Media S.A.
24	1022	BMC Neuroscience	1.023	Q2	19	Neurosciences. Biological psychiatry. Neuropsychiatry	CC BY, CC0	BMC
25	1023	Neurobiology of Sleep and Circadian Rhythms	1.009	Q2	9	Neurosciences. Biological psychiatry. Neuropsychiatry	CC BY, CC BY-NC-ND	Elsevier
26	1024	Brain Sciences	0.999	Q2	11	Neurosciences. Biological psychiatry. Neuropsychiatry	CC BY	MDPI AG
27	1025	International Journal of Mental Health Systems	0.965	Q1	13	Neurosciences. Biological psychiatry. Neuropsychiatry	CC BY, CC0	BMC
28	1026	IBRO Reports	0.938	Q2	14	Neurosciences. Biological psychiatry. Neuropsychiatry	CC BY, CC BY-NC-ND	Elsevier
29	1027	Neuroscience of Consciousness	0.904	Q1	19	Neurosciences. Biological psychiatry. Neuropsychiatry	CC BY, CC BY-NC	Oxford University Press
30	1028	Journal of Experimental Neuroscience	0.882	Q2	8	Neurosciences. Biological psychiatry. Neuropsychiatry	CC BY, CC BY-NC	SAGE Publishing
31	1029	International Journal of Alzheimer's Disease	0.881	Q2	11	Neurosciences. Biological psychiatry. Neuropsychiatry	CC BY	Hindawi Limited
32	1030	Brain and Behavior	0.873	Q2	14	Neurosciences. Biological psychiatry. Neuropsychiatry	CC BY	Wiley
33	1031	Neurobiology of Pain	0.803	Q1	8	Neurosciences. Biological psychiatry. Neuropsychiatry	CC BY, CC BY-NC-ND	Elsevier
34	1032	Frontiers in Neurorobotics	0.75	Q2	14	Neurosciences. Biological psychiatry. Neuropsychiatry	CC BY	Frontiers Media S.A.
35	1033	Behavioural Neurology	0.701	Q2	34	Neurosciences. Biological psychiatry. Neuropsychiatry	CC BY	Hindawi Limited
36	1034	Translational Neuroscience	0.623	Q3	6	Neurosciences. Biological psychiatry. Neuropsychiatry	CC BY-NC-ND	De Gruyter
37	1035	Journal of Mathematical Neuroscience	0.588	Q3	13	Neurosciences. Biological psychiatry. Neuropsychiatry	CC BY	SpringerOpen
38	1036	Clinical Neurophysiology Practice	0.582	Q3	35	Neurosciences. Biological psychiatry. Neuropsychiatry	CC BY, CC BY-NC-ND	Elsevier
39	1037	Dementia & Neuropsychologia	0.453	Q3	8	Neurosciences. Biological psychiatry. Neuropsychiatry	CC BY	Associação Neurologia Cognitiva e do Comportamento
40	1038	Basic and Clinical Neuroscience	0.431	Q3	4	Neurosciences. Biological psychiatry. Neuropsychiatry	CC BY-NC	Iran University of Medical Sciences
41	1039	Neurology International	0.37	Q3	11	Neurosciences. Biological psychiatry. Neuropsychiatry	CC BY	MDPI AG
42	1040	BioPsychoSocial Medicine	0.318	Q3	18	Neurosciences. Biological psychiatry. Neuropsychiatry	CC BY, CC0	BMC
43	1041	AIMS Neuroscience	0.303	Q4	8	Neurosciences. Biological psychiatry. Neuropsychiatry	CC BY	AIMS Press

44	1042	Neuroscience Journal	-	-	14	Neurosciences. Biological psychiatry. Neuropsychiatry	CC BY	Hindawi Limited
45	1043	Global Mental Health	-	-	25	Neurosciences. Biological psychiatry. Neuropsychiatry	CC BY, CC BY-NC-SA, CC BY-NC-ND	Cambridge University Press
46	1044	Journal of Clinical Movement Disorders	-	-	15	Neurosciences. Biological psychiatry. Neuropsychiatry	CC BY, CC0	BMC
47	1045	Epilepsy and Behavior Case Reports	-	-	6	Neurosciences. Biological psychiatry. Neuropsychiatry	CC BY, CC BY-NC-ND	Elsevier
48	1046	Brain and Neuroscience Advances	-	-	8	Neurosciences. Biological psychiatry. Neuropsychiatry	CC BY, CC BY-NC	SAGE Publishing
49	1047	Personality Neuroscience	-	-	6	Neurosciences. Biological psychiatry. Neuropsychiatry	CC BY, CC BY-NC-SA, CC BY-NC-ND	Cambridge University Press
50	1048	Brain Communications	-	-	6	Neurosciences. Biological psychiatry. Neuropsychiatry	CC BY	Oxford University Press
51	1049	Neuroscience Insights	-	-	9	Neurosciences. Biological psychiatry. Neuropsychiatry	CC BY, CC BY-NC	SAGE Publishing

The first paper included in this thesis *("Circuit-Specific Dendritic Development in the Piriform Cortex"*) was published in the open access journal from society for neurosciences "eNeuro" in 2018. At this time, the journal was not included in the ISi Web of Knowledge list. However, eNeuro had an impact factor of **3.544** and was already part of the Open Access Journal Positive List from the QUEST center of the Berlin Institute of Health (BIH) at Charité. This list comprises biomedical open access journals listed by the Directory of Open Access Journal (DOAJ). DOAJ ensures in turn that journals follow high quality standards.

The Open Access Journal Positive List includes the SCImago Journal Rank (SJR) and the SJR quartiles. The SJR measures the journal impact acording to the average prestige per article; which means that it measures the influence of journals acording to the number of citations received and the prestige of the journals where citations were done ("https://www.scimagojr.com/"). For eNeuro, the SJR in 2018 was **2.218**:

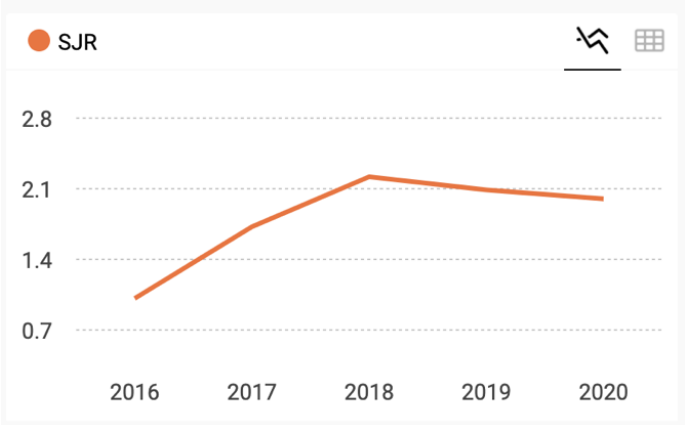

Taken from https://www.scimagojr.com/journalsearch.php?q=21100782808&tip=sid&clean=0

The SJR quartiles compare journals ranking within subject categories; the set of journals ranked according to their SJR are divided into four equal groups (quartiles). Journals in the first quartile (Q1) are among those with the highest SJR in their category

(“https://www.scimagojr.com/”). Already in 2018, eNeuro was placed in the **Q1** for the subject category of **“Neurosciences”:**

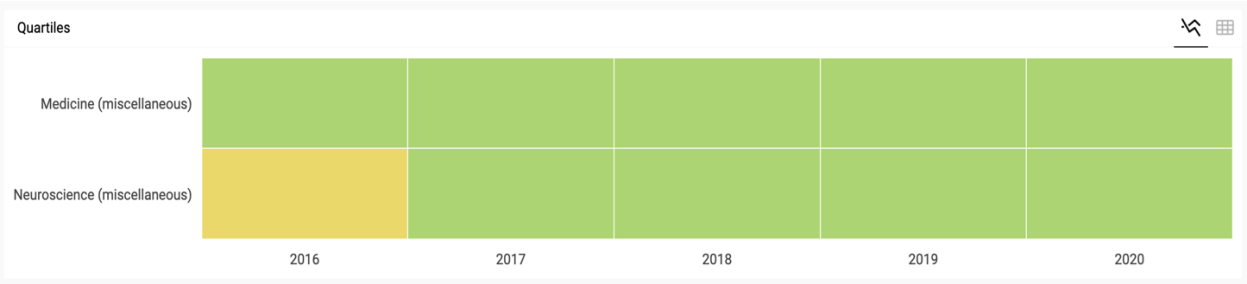

The color code image shows the quartiles for eNeuro for two categories. Q1 (green) comprises the quarter of the journals with the highest values, Q2 (yellow) the second highest values, Q3 (orange) the third highest values and Q4 (red) the lowest values. Taken from https://www.scimagojr.com/journalsearch.php?q=21100782808&tip=sid&clean=0.

These indicators rank the Journal “eNeuro” very high in the category of Neurosciences and ensure the high quality of its publications.

13. Publication 1: Circuit-Specific Dendritic Development in the Piriform Cortex

eNeuro

Research Article: New Research

Development

Circuit-Specific Dendritic Development in the Piriform Cortex

Laura Moreno-Velasquez,[1] Hung Lo,[1,5] Stephen Lenzi,[3] Malte Kaehne,[2] Jörg Breustedt,[1] Dietmar Schmitz,[1,4,5] Sten Rüdiger,[3] and Friedrich W. Johenning[1,5]

https://doi.org/10.1523/ENEURO.0083-20.2020

[1]Neuroscience Research Center, Charité-Universitätsmedizin Berlin, Corporate member of Freie Universität Berlin, Humboldt-Universität zu Berlin, and Berlin Institute of Health, 10117 Berlin, Germany, [2]Institute of Physics, Humboldt Universität Berlin, 12489 Berlin, Germany, [3]Sainsbury Wellcome Centre, University College London, London W1T 4JG, UK, [4]NeuroCure Cluster of Excellence, 10117 Berlin, Germany, and [5]Einstein Center for Neurosciences Berlin, 10117 Berlin, Germany

Abstract

Dendritic geometry is largely determined during postnatal development and has a substantial impact on neural function. In sensory processing, postnatal development of the dendritic tree is affected by two dominant circuit motifs, ascending sensory feedforward inputs and descending and local recurrent connections. In the three-layered anterior piriform cortex (aPCx), neurons in the sublayers 2a and 2b display vertical segregation of these two circuit motifs. Here, we combined electrophysiology, detailed morphometry, and Ca^{2+} imaging in acute mouse brain slices and modeling to study circuit-specific aspects of dendritic development. We observed that determination of branching complexity, dendritic length increases, and pruning occurred in distinct developmental phases. Layer 2a and layer 2b neurons displayed developmental phase-specific differences between their apical and basal dendritic trees related to differences in circuit incorporation. We further identified functional candidate mechanisms for circuit-specific differences in postnatal dendritic growth in sublayers 2a and 2b at the mesoscale and microscale levels. Already in the first postnatal week, functional connectivity of layer 2a and layer 2b neurons during early spontaneous network activity scales with differences in basal dendritic growth. During the early critical period of sensory plasticity in the piriform cortex, our data are consistent with a model that proposes a role for dendritic NMDA-spikes in selecting branches for survival during developmental pruning in apical dendrites. The different stages of the morphologic and functional developmental pattern differences between layer 2a and layer 2b neurons demonstrate the complex interplay between dendritic development and circuit specificity.

Key words: dendritic development; NMDA-spike; piriform cortex

Significance Statement

Sensory cortices are composed of ascending sensory circuits that relay sensory information from the periphery and recurrent intracortical circuits. Dendritic trees of neurons are shaped during development and determine which circuits contribute to the neuronal input space. To date, circuit-specific aspects of dendritic development and the underlying mechanisms are poorly understood. Here, we investigate dendritic development in layer 2 of the piriform cortex, a three-layered palaeocortex that displays a clear vertical segregation of sensory and recurrent circuits. Our results suggest that dendritic development occurs in distinct developmental phases with different circuit-specific properties. We further identify candidate mechanisms for neuronal activity patterns that could determine differences in circuit-specific dendritic development.

Received March 3, 2020; accepted April 20, 2020; First published May 26, 2020.
The authors declare no competing financial interests.

Author contributions: L.M.-V., H.L., S.L., M.K., J.B., D.S., S.R., and F.W.J. designed research; L.M.-V., H.L., S.L., M.K., and F.W.J. performed research; L.M.-V., H.L., S.L., M.K., J.B., S.R., and F.W.J. analyzed data; L.M.-V., M.K., J.B., D.S., S.R., and F.W.J. wrote the paper.

May/June 2020, 7(3) ENEURO.0083-20.2020 1–20

Introduction

The complex geometry of neuronal dendritic trees in relation to their function is not yet fully understood. In sensory cortices, sensory input from the periphery is distributed to cortical neurons in an ascending sensory stream of input. Recurrent connectivity between cortical neurons constitutes the local and descending stream of input, which then transforms the sensory input into cortical output (Srinivasan and Stevens, 2018; Kanari et al., 2019). Developmental growth patterns of dendritic structures are an important determinant of a neuron's function within the different circuits constituting its synaptic input space (Lanoue and Cooper, 2018). This brings up the question of how dendritic morphology develops in relation to the two different glutamatergic circuit elements in sensory information processing, ascending sensory input and recurrent connectivity.

We investigated the palaeocortical three-layered anterior piriform or primary olfactory cortex (aPCx), which shares structural and functional similarities with the reptilian dorsal cortex (Fournier et al., 2015). The aPCx is the largest cortical region receiving olfactory sensory inputs. Peripheral odor information from nasal olfactory sensory neurons converges onto the aPCx via the olfactory bulb. Functionally, the aPCx synthesizes the segregated peripheral input into odor objects and identifies them (Wilson and Sullivan, 2011). Unlike topographically organized neocortical sensory systems, afferent sensory and recurrent input streams to the aPCx lack any apparent spatial structure and are therefore non-topographical (Srinivasan and Stevens, 2018). Layer 2 is the main cellular layer of the olfactory cortex (Bekkers and Suzuki, 2013). Based on the distribution of genetic markers and somatic morphology, layer 2 can be divided into layer 2a (superficial third) and layer 2b (deeper two-thirds; Diodato et al., 2016; Choy et al., 2017; Bolding et al., 2019; Martin-Lopez et al., 2019). Layer 2a predominantly contains superficial so-called semilunar cells (layer 2a neurons). Layer 2b harbors pyramidal cells and semilunar-pyramidal transition cells (layer 2b neurons; Suzuki and Bekkers, 2011; Choy et al., 2017). Neurons in the two sublayers display differences in functional circuit incorporation. Layer 2a neurons predominantly sample converging sensory input and distribute it unidirectionally to the layer 2b and 3 neurons. Layer 2b neurons receive sensory input and, in addition, are incorporated in a rich recurrent network (Suzuki and Bekkers, 2011; Wiegand et al., 2011; Hagiwara et al., 2012; Choy et al., 2017). Recently, it has been demonstrated *in vivo* that these two neuron types play different roles in reading out converging sensory input (layer 2a neurons) and performing pattern storage and completion via recurrent circuits (layer 2b neurons; Bolding et al., 2019).

This vertical organization of input space of layer 2 neurons extends to the dendritic tree, where sensory and recurrent functional domains are spatially segregated. In the apical dendrites of all neurons in layer 2, the majority of sensory input projects to the superficial layer 1a. Layer 1a can be clearly distinguished from layer 1b, which, together with inputs in layers 2 and 3, samples recurrent inputs. Basal dendrites exclusively sample recurrent inputs (Franks Kevin and Isaacson, 2005; Johenning et al., 2009). In aPCx, we therefore observe a clear vertical segregation of functionally distinct cell types and of different functional dendritic domains. This feature of aPCx makes layer 2 of the aPCx an ideal model for the differential analysis of dendritic growth patterns related to sensory input and recurrent connectivity.

Here, we studied developmental dendritic growth in layer 2a and layer 2b neurons in acute brain slices of the aPCx. We applied electrophysiology, detailed morphometry of 3D-reconstructed neurons, Ca^{2+} imaging and computational modeling. We identified distinct phases of dendritic development with cell-type-specific differences of dendritic growth and pruning patterns. We related the different developmental patterns described here at the morphologic level to physiological differences at the microscale and mesoscale levels. This enabled us to identify candidate mechanisms that may drive circuit-specific dendritic development in a non-topographic sensory system.

Materials and Methods

Slice preparation

Acute brain slices were prepared from C57Bl6N mice of either sex except for population Ca^{2+} imaging experiments with GCaMP, where Ai95-NexCre mice were used. In experiments for Figures 1-5, the horizontal slicing orientation was chosen to preserve rostrocaudal association fibers (Demir et al., 2001). For layer 1a dendritic spike measurements in Figure 6, we used coronal slices. All animal procedures were performed in accordance with the national and institutional guidelines of the Charité-Universitätsmedizin Berlin. All procedures were approved by the local health authority and the local ethics committee (Landesamt für Gesundheit und Soziales, Berlin). For morphologic reconstruction, acute brain slices were prepared at four age intervals expressed in postnatal days (p): p1–p2, p6–p8, p12–p14, and p30–p40 (>p30). Electrophysiological Characterization was limited to the two age intervals p12–p14 and p30–p40. For measurements of NMDA-spikes, coronal slices were prepared at p14–p21. Brains from p30–p40 mice and from mice used for dendritic spike measurements were prepared in ice-cold artificial CSF (ACSF; pH

This work was supported by the Deutsche Forschungsgemeinschaft (German Research Foundation) Grants SFB 1315 Project-ID 327654276, Exc 2049, and SPP 1665 (to D.S.); JO 1079/3-1 (to F.W.J.); and RU1660/5-1 (to S.R.); the Bundesministerium für Bildung und Forschung (Federal Ministry of Education and Research) Grant 01GQ1420B (to D.S.); and the ERC BrainPlay-Synergy Grant (D.S.).

Acknowledgements: We thank Robert Sachdev and Matthew Larkum for the Ai95 mouse line. We also thank Anke Schönherr and Susanne Rieckmann for excellent technical assistance.

Correspondence should be addressed to Friedrich W. Johenning at friedrich.johenning@charite.de.

https://doi.org/10.1523/ENEURO.0083-20.2020

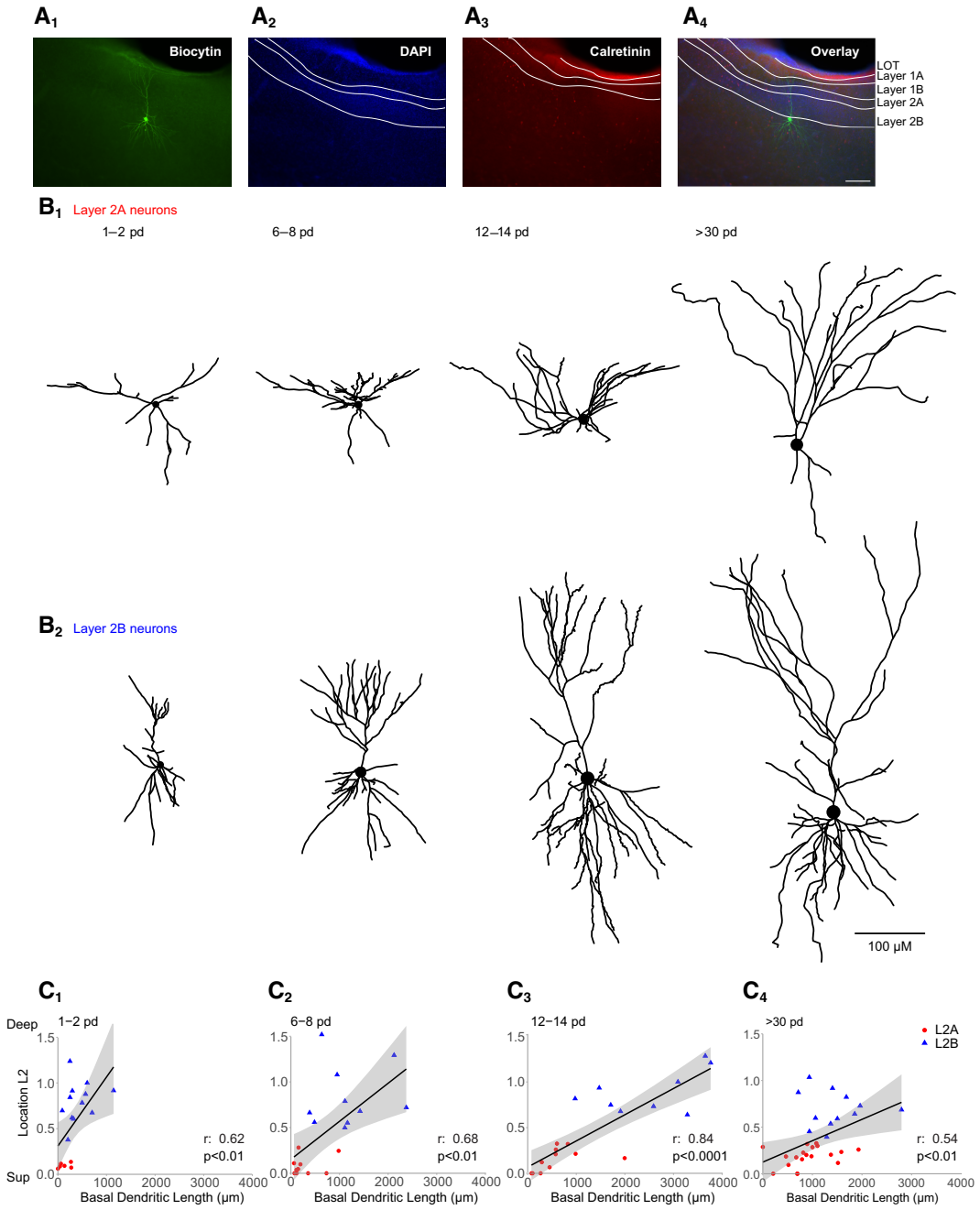

Figure 1. Localization and differentiation of the two principal neuron types in layer 2 of the aPCx. ***A***, Slice containing one recorded neuron filled with biocytin (***A1***) and, additionally, *post hoc* labeled with DAPI (***A2***) and calretinin (***A3***). The overlay (***A4***) shows the recorded neuron located in the layer 2b/layer 3 transition zone of the aPCx. LOT stands for lateral olfactory tract. ***B***, 3D morphologic reconstructions of different layer 2a (***B1***) and layer 2b (***B2***) neurons at four time windows (expressed as postnatal days, pd): right

continued
after birth (p1–p2), at the end of the first postnatal week (p6–p8), at the end of the second postnatal week (p12–p14), and after the fifth postnatal week (>p30). Scale bar: 100 μm. ***C***, Correlation between the total basal dendritic length and the vertical position of the cells in layer 2 (layer 2a neurons (L2A) in red, layer 2b neurons (L2B) in blue) is shown at the same four time windows (C1: p1–2, C2: p6–8, C3: p12–14, C4: >p30). Spearman *r* and *p* values are shown for each time group. See Extended Data Figure 1-1 for further details.
Figure Contributions: Laura Moreno-Velasquez performed the experiments and analyzed the data.

7.4) containing the following: 87 mM NaCl, 26 mM $NaHCO_3$, 10 mM glucose, 2.5 mM KCl, 3 mM $MgCl_2$, 1.25 mM NaH_2PO_4, 0.5 mM $CaCl_2$, and 50 mM sucrose. Slices were cut at 400-μm thickness and incubated at 35°C for 30 min. The slices were then transferred to standard ACSF containing the following: 119 mM NaCl, 26 mM $NaHCO_3$, 10 mM glucose, 2.5 mM KCl, 2.5 mM $CaCl_2$, 1.3 mM $MgCl_2$, and 1 mM NaH_2PO_4. Slices from other age groups were cut in ice-cold standard ACSF and incubated for 30 min in standard ACSF at 35°C. The slices were then stored in standard ACSF at room temperature in a submerged chamber for 0.5–6 h before being transferred to the recording chamber. For dendritic spike measurements in Figure 6, 1 μM gabazine was added to the recording solution. Experiments requiring spontaneous network activity were prepared in ice-cold ACSF containing the following: 125 mM NaCL, 25 mM $NaCHCO_3$, 10 mM glucose, 4 mM KCL, 1.25 mM NaH_2PO_4, 2 mM $CaCl_2$, and 1 mM $MgCl_2$. Slices were incubated at 35°C for 30 min and stored at room temperature in a submerged chamber for 0.5–7 h. All recordings were performed at near-physiological temperature (32–34°C).

Electrophysiology

Whole-cell current clamp experiments were performed at near physiological temperature (32–34°C) using an Axon Multiclamp 700B amplifier (Molecular Devices). For morphologic reconstruction and characterization, signals were low pass filtered at 2 kHz and digitized at a sampling rate of 20 kHz (BNC-2090, National Instruments Corporation). Pipettes (3–6 MΩ) were filled with an intracellular solution containing the following: 135 mM K-gluconate, 6 mM KCl, 10 mM HEPES, 0.2 mM EGTA, 2 mM $MgCl_2$, 2 mM Na-ATP, 0.5 mM Na-GTP, and 5 mM phosphocreatine Na (pH 7.3) and biocytine (0.20%). Liquid junction potential (LJP) was not corrected. Bridge balance compensation was applied in current clamp. Cells were discarded if the resting membrane potential was above −60 mV or the series resistance exceeded 30 MΩ. For dendritic spike recordings, signals were low pass filtered at 8 kHz and digitized at a sampling rate of 20 kHz. Pipettes (3–6 MΩ) were filled with an intracellular solution containing the following: 130 mM K-gluconate, 20 mM KCl, 10 mM HEPES, 4 mM MgATP, 0.3 mM NaGTP, 10 mM phosphocreatine (pH 7.3, adjusted with KOH), 30 μM Alexa Fluor (AF) 594, and 500 μM fluo-5F. Experiments were conducted without exceeding −200 pA at resting membrane potential (layer 2a neurons were held at −60 mV, and layer 2b neurons were held at −70 mV). Series resistance was below 30 MΩ. After dye-filling the patched neuron for 10 min, we placed the θ-glass stimulation electrode close to the distal dendrite in layer 1a of the piriform cortex. Stimulation protocol was set to three pulses at 50 Hz with 10-μA steps (with one exception in layer 2b neuron, which was with 20-μA steps).

Electrophysiological analysis

Analysis was performed using custom-written routines in Python. Resting membrane potential (Vm) was taken as the mean value of the baseline before current injections were performed. For characterization, neurons were held at −60 mV. Input resistance (IR), membrane time constant (Tau), and membrane capacitance (Cm) were calculated from the voltage response to an 80-pA hyperpolarizing current step. Action potential (AP) threshold was defined as the membrane potential at the point where the slope (dV/dt) reached 1% of its maximum. The fast after-hyperpolarization (fAHP) was defined as the difference between AP threshold and the minimum voltage seen immediately after the AP peak (within 5 ms). Finally, the instant firing frequency was defined as the frequency between the first and second AP. For comparability, these values were extracted from the first 600-ms current injection step that elicited at least nine APs. When analyzing the integrative behavior of apical dendrites in Figure 6, we analyzed the changes in EPSP size on linear increase of stimulation intensity. To quantify EPSP size, we measured the amplitude and area under curve of a 60-ms time window following the third pulse compared with baseline (50-ms period before stimulus). Effects of (2*R*)-amino-5-phosphonovaleric acid (APV) were quantified for the largest response that did not yet evoke an AP.

Immunohistochemistry

Slices with biocytin-filled cells were stored in 4% paraformaldehyde (PFA) overnight. The following day, slices were washed three times (10 min each) in PBS and incubated in a blocking solution composed of 5% normal goat serum (NGS; Biozol), 1% Triton X-100 (Sigma), and PBS, for 3 h at room temperature with gentle agitation. Primary antibodies were diluted in blocking solution (2.5% NGS, 1% Triton X-100, PBS), and slices were incubated for 72 h at 4°C. Biocytin-filled neurons were labeled with a streptavidin marker conjugated to AF 488 (Invitrogen, S-32354; 1:500 dilution). Additionally, the lateral olfactory tract (LOT) and mitral cell axons in layer 1a were labeled with calretinin (anti-mouse; Millipore, MAB1568; 1:1000 dilution or anti-rabbit; SWANT, 7697; 1:4000 dilution) and interneurons with GAD 67 (anti-mouse; Millipore, MAB 5406; 1:500 dilution), GAD 65/67 (anti-rabbit; Chemicon, AB 11070; 1:500 dilution), or gephyrin (anti-mouse; SYSY 147111; 1:500 dilution).

Following this, slices were washed two times (10 min each) with PBS and secondary antibodies (goat anti-rabbit AF 555, goat anti-rabbit AF 647, goat anti-mouse AF

555, goat anti-mouse AF 647; Invitrogen; 1:500 dilution in 0.5% Triton X-100, PBS) were applied for 3 h at room temperature. Finally, slices were washed three times (10 min each) in PBS and mounted on glass slides in mounting medium Fluoroshield with 4',6-diamidino-2-phenylindole (DAPI; Sigma).

Reconstructions and morphologic analysis

Mounted slices were visualized on a fluorescent microscope (10× objective, 0.3 N.A.; Leica) to identify and select the biocytin-filled neurons located in the aPCx for further reconstruction. Only neurons that displayed homogenous filling with biocytin and lacked obvious amputation of the dendritic tree by slicing were analyzed. Therefore, not all neurons chosen for electrophysiology were also chosen for morphologic reconstruction and vice versa. Selected slices were then imaged on an upright Leica TCS SP5 confocal microscope (Leica Microsystems) through a 20× immersion objective (0.7 N.A.; Leica) with 405-nm (diode), 488-nm (argon), 568-nm (solid state), and 633-nm (helium-neon) laser lines. For biocytin-filled neurons, the perisomatic field of view was further imaged through a 63× immersion objective (1.4 N.A.; Leica) to validate the spine density. Cells were selected and classified according to their position in layer 2 of the aPCx using FIJI (https://imagej.nih.gov/ij/). The position in layer 2 was defined as the smallest distance from the soma to the border between layer 1b and layer 2a, normalized to the total width of layer 2 for each neuron. The border between layers 1a and 1b was traced to later classify the apical dendrites according to their synaptic inputs. Neuronal morphologies were then reconstructed with neuTube software (Feng et al., 2015) and exported as SWC files. Morphometric parameters were extracted with L-measure software (Scorcioni et al., 2008) and analyzed with R studio and Python using btmorph v2 (Torben-Nielsen, 2014) and SciPy packages.

Ca^{2+} imaging

For population Ca^{2+} imaging of neonatal spontaneous synchronous network events (Fig. 4), we used the genetically encoded Ca^{2+} indicator (GECI) GCaMP6F. NEX-Cre mice (Goebbels et al., 2006) were crossed with Ai95 animals (https://www.jax.org/strain/024105; Madisen et al., 2015) for constitutive GCaMP6F expression in excitatory cells only.

For experiments involving spontaneous network activity, Ca^{2+} imaging was performed using a Yokogawa CSU-22 spinning disk microscope at 5000 rpm. The spinning disk confocal permitted the generation of a large field of view time series at a high acquisition rate. A 488-nm laser was focused onto the field of view using a 40× objective. Emission light was filtered using a 515 ± 15-nm bandpass filter. Fluorescence was detected using an Andor Ixon DU-897D back-illuminated CCD, with a pixel size of 16 μm. Andor iQ software was used for data acquisition. Population Ca^{2+} imaging was performed at 10 Hz when single cells were measured. For measuring of larger regions of interest (ROIs) incorporating layer 2, 10-Hz data were pooled with a dataset acquired at 40 Hz.

For analyzing dendritic spikes using 2P-imaging, 30 μM AF 594 and 500 μM Fluo-5F were added to the intracellular solution. A Femto 2D two-photon laser scanning system (Femtonics Ltd.) equipped with a femtosecond pulsed Ti:Sapphire laser tuned to λ = 805 nm (Cameleon, Coherent) controlled by the MATLAB-based MES software package (Femtonics Ltd.) was used. Fluorescence was detected in epifluorescence mode with a water immersion objective (LUMPLFL 60×/1.0 N.A., Olympus). Transfluorescence and transmitted infra-red light were detected using an oil immersion condenser (Olympus). The average scanning speed was 300 Hz, and the intermediate sections were jumped over within 60 μs using a spline interpolated path. Dendritic Ca^{2+} transients were measured every 30 s.

Imaging analysis

For population Ca^{2+} imaging (Fig. 4), fields of view (FOVs) with at least 5 min of recordings were included in the analysis. Videos were motion corrected using Suite2p (Pachitariu et al., 2017) and analyzed using custom Python code and SamuROI (Rueckl et al., 2017). If motion artefacts were too great to be corrected, recordings were not included in the subsequent analysis. Each pixel of the raw data was normalized using the six-sample window with the lowest SD. Traces were extracted from each ROI, and event detection was conducted. Events were detected as increases in $\Delta F/F > 2.5$ SDs from baseline with a peak width of at least two consecutive samples. The results were manually curated with the user free to exclude events based on the interevent interval, amplitude, signal-to-noise ratio, and peak width. Incomplete events at the start or end of each recording were excluded from analysis. The rates of false positives and negatives were 4.5% and 5.1%, respectively, calculated from a random subset of the data (100 cells, three mice).

The upper and lower boundaries of layer 2 were manually defined based on cell density. For detection of global events, we measured the average change in fluorescence for all pixels of layer 2 piriform cortex, including the neuropil, using a rectangular ROI defined by the upper and lower boundaries of layer 2.

For single-cell analysis, we used a semi-automated method based on image segmentation with Ilastik (Sommer et al., 2011). This was required because a large number of cells were inactive, or closely packed and/or synchronous in their activity. Ilastik was trained to segment z-projection sum images of a subset of FOVs to produce a five-label image (nuclei, somata, bright debris, dark debris, and background). Cells were detected using the nuclei label with false positives manually rejected. Using these cell locations, the somata image was divided into territories using watershed segmentation, and only the nearest pixels to each nucleus were included. ROIs with fewer than 70 pixels were rejected. We calculated the $\Delta F/F$ for each ROI and subtracted an estimate of the local neuropil contribution using an equal number of randomly selected non-cell pixels within a fixed radius of 70 pixels.

Modeling

For the model in Figure 7, we assumed that the density of synapses on the branches of a dendrite is constant, i.e., depends linearly on the length of a branch. We assumed that on odor exposure a maximum of 70 active synapses can arrive at a single neuronal dendrite. Following recent experimental measurements (Srinivasan and Stevens, 2018), we considered 3700 glomeruli, 9.7×107 synapses between all glomeruli and all layer 2 neurons, and a total of 41,000 layer 2 neurons. Hence, we dealt with an average $9.7 \times 107/41{,}000 = 2366$ synapses between all glomeruli and one neuron. Thus, for 70 synapses to be activated on odor exposure, we assumed that 109 glomeruli are activated per odor ($=3700 \times 70/2366$).

We characterized the morphology of a neuron through its mean branch length (BL), which we found to range from 40 to 110 μm (mean is 72 μm; see Results). The total dendritic BL (TDBL) on average is ~1800 μm.

For simplicity, we approximated the length of any branch by the mean values of the respective neurons. Accordingly, dendrites could have a maximum of $1800/40 = 45$ (short-branched neuron) and a minimum of $1800/110 = 16$ branches (long-branched neuron).

We distinguished the two cases of clustered (n_{clus}) and distributed (n_{dist}) stimulation. We assumed that a neuron fires if it is exposed to more than $n_{dist} = 40$ active input synapses or $n_{clus} = 10$ active inputs arriving on the same branch. The excitation behavior is schematically illustrated in Figure 7*A*, showing a simplified version of the nonlinear dendritic integration scheme proposed by Poirazi et al. (2003). Specifically, we considered every neuron as a two-layered network that may or may not produce a network response (express a somatic AP) to a presented stimulus set. This response is triggered in cases when the distributed input reaches a certain threshold number (reflecting a number of active input synapses), which can be understood as a linear integration scheme of the neuron. In addition, the network may produce a response to a dendritic spike. In our model, dendritic spikes led to the nonlinear integration of synaptic input, which is mimicked through the activation gates on every branch of the neuron (first layer of the network). In Figure 7*A*, this first layer of the network is shown as blue circles. The green circle represents the soma. The magnification insets illustrate the stimulus-response relationship of the separate branches and the soma, respectively. The model was constructed such that a somatic response is expressed if the distributed stimulation crosses the threshold value n_{dist} or if one of the branches expresses a dendritic spike, which relates to the number of active synapses on the branch crossing the threshold number of clustered stimulation n_{clus}.

Using this described model, we investigated the additional response probability that is introduced through considering clustered stimulation. We supposed the number of odor-activated synapses (which we refer to as λ) connected to a given neuron to be random. The probability of finding a neuron that is connected to n or more odor activated synapses can then be approximated as

$$P(\lambda, n) = 1 - \sum_{k=1}^{n-1} \frac{\lambda^k e^{-\lambda}}{k!}. \quad (1)$$

Equation 1 allowed us to map the response probability of a neuron to a presented stimulus. In the case of clustered stimulation, this picture is slightly different: Instead of the mean number of synapses per neuron, the mean number of synapses per branch is the relevant quantity. The mean number of branches (NB) is approximately the TDBL divided by the mean BL. We took the distribution of BL into account as we reasoned that longer branches optimize the input-output relationship in case of clustered stimulation. At p12–p14, the length of the dendritic branches ranged from 40 to 110 μm. The response probability for clustered stimulation is modeled as following:

$$P(\lambda, n) = 1 - \left(1 - \sum_{k=1}^{n-1} \frac{\lambda^k e^{-\lambda}}{k!}\right)^{\frac{\text{TDBL}}{\text{BL}}}, \quad \text{with } \lambda = S\frac{\text{BL}}{\text{TDBL}}. \quad (2)$$

It is important to note that under such a scheme, stimulation of any dendritic branch can be sufficient to excite the neuron.

Code accessibility

The code underlying the calculations and plot in Figure 7 is available as Extended Data 1 and via GitHub (https://github.com/mkahne/DendriticBranches). The code was executed using Python 3.7.3 on a MacBook Pro running on MacOs 10.15.4.

Statistics

Data were first tested for normality. Statistical tests were performed as indicated using GraphPad Prism, the SciPy library, and the DABEST package in Python and R (Ho et al., 2019). We used the paired (normally distributed direct comparisons) and unpaired *t* test (normally distributed single comparisons), Wilcoxon test (not normally distributed direct comparisons), Mann–Whitney test (not normally distributed single comparisons), one-way ANOVA with Holm–Sidak's multiple comparisons test (normally distributed multiple comparisons) or Kruskal–Wallis test with Dunn's multiple comparison as a *post hoc* test (not normally distributed multiple comparisons) as indicated in the text. Extended Data Table 1-2 contains all applied tests and the exact *p* values. Additionally, the Spearman correlation test was used to measure the association between cell position and branch-length in Figure 1*C* (statistical details can be found in Extended Data Table 1-2). Numerical values are given as mean and SEM unless otherwise stated. To facilitate the interpretation of our results and the narrative flow of the paper, we followed the convention of defining $p < 0.05$ as significant in the text. However, to facilitate the realistic evaluation of our data and its interpretation, we omitted

Table 1: Intrinsic electrical properties of layer 2a and layer 2b neurons at p12–p14 and >p30

	12–14 pd		>30 pd		
	SL	SP	SL	SP	
Vm (mV)	–75.32 ± 1.96	–73.48 ± 2.86	–71.88 ± 1.89	–72.23 ± 2.01	
Rin (MΩ)	233.35 ± 40.24	147.52 ± 27.07	168.71 ± 22.65	235.29 ± 51.62	
Tau (ms)	25.65 ± 2.94	22.98 ± 4.24	20.79 ± 1.98	22.53 ± 1.48	
Cm (pF)	123.17 ± 11.86	156.30 ± 10.44	135.89 ± 9.66	114.52 ± 10.43	
Threshold (mV)	–35.97 ± 1.50	–39.37 ± 1.17	–40.28 ± 1.52	–40.35 ± 1.07	
fAHP (mV)	7.75 ± 1.30	5.65 ± 1.51	10.83 ± 1.59	7.96 ± 0.77	
Instant firing freq (Hz)	37.99 (22.69–108.13)	34.81 (29.90–104.40)	44.87 (30.83–197.12)	68.78 (29.42–88.44)	Median (IQR)

SL refers to layer 2a neurons, SP to layer 2b neurons. See Extended Data Table 1-1, Table 1-2 for further details.

significance stars from the majority of the plots. Wherever possible, we used estimation-based statistics with mean-difference plots instead (Ho et al., 2019).

Results

Layer identification in postnatal development

In acute horizontal mouse brain slices, we performed whole cell patch clamp recordings of randomly sampled excitatory neurons over the whole vertical extent of layer 2 including the layer 2/3 transition zone. Excitatory neurons were distinguished from interneurons by at least one of the three criteria: firing profile (Suzuki and Bekkers, 2010), morphology, and a negative *post hoc* staining for interneuron markers. During patching, neurons were filled with biocytin for later morphologic reconstructions (Fig. 1*A1*).

For analysis, the extent of layer 2 was delineated using a DAPI stain (Fig. 1*A2*). Layer 2 was divided into layer 2a (upper third) and layer 2b (deep two-thirds and layer 2/3 transition zone; Choy et al., 2017; Martin-Lopez et al., 2019). We chose this division into sublayers for categorization although there is a postulated gradient of the electrophysiological and morphologic differences between deep and superficial neurons (Suzuki and Bekkers, 2011; Wiegand et al., 2011). Our rationale behind this hard segregation is the clear distribution of genetic markers in layer 2 and the necessity to find a criterion applicable to all age groups studied. All published genetic markers for superficial or layer 2a neurons seemed to display a clear and selective expression profile in the upper third of layer 2 (Diodato et al., 2016; Choy et al., 2017; Bolding et al., 2019). In addition, functional analysis of neurons expressing genetic markers of layer 2a neurons display reduced recurrent circuit incorporation (Choy et al., 2017; Bolding et al., 2019).

We confirmed the location of the aPCx by staining the LOT and layer 1a fibers with calretinin (Sarma et al., 2011; Fig. 1*A3*). The calretinin staining also permitted clear delineation of dendritic segments terminating in layer 1a (Fig. 1*A4*, see Fig. 5). 3D reconstructions using neutube (Feng et al., 2015) of layer 2a ($n = 46/25$ neurons/mice; Fig. 1*B1*) and layer 2b ($n = 43/27$ neurons/mice; Fig. 1*B2*) neurons were analyzed at four time windows: right after birth (p1–p2, layer 2a: $n = 6/4$; layer 2b: $n = 12/6$; neurons/mice), at the end of the first postnatal week (p6–p8, layer 2a: $n = 10/5$; layer 2b: $n = 10/7$; neurons/mice), during the critical period of heightened sensory synaptic and structural plasticity (p12–p14, layer 2a: $n = 11/8$; layer 2b: $n = 9/8$; neurons/mice; Franks Kevin and Isaacson 2005; Poo and Isaacson 2007), and after the critical period (>p30, layer 2a: $n = 19/6$; layer 2b: $n = 12/6$; neurons/mice; Fig. 1*B*).

Neurons in sublayers 2a and 2b are distinct

Electrophysiological characterization was performed for a subset of neurons at p12–p14 (layer 2a: $n = 10/6$; layer 2b: $n = 8/7$; neurons, mice) and at >p30 (layer 2a: $n = 14/7$; layer 2b: $n = 9/6$; neurons, mice). When sampling the whole extent of layer 2a and layer 2b, we did not find statistically significant electrophysiological differences between neurons in the layers 2a and 2b at both ages (Table 1; Extended Data Table 1-1, Table 1-2; see Discussion).

In addition to previously reported electrophysiological differences, the less complex basal dendritic tree of superficial layer 2a cells compared with deeper neurons in layer 2b is a prominent distinctive feature (Bekkers and Suzuki, 2013). As basal dendritic length most likely scales with local recurrent wiring (Haberly, 1985), this is a good indicator of a layer 2 neuron's recurrent circuit incorporation, which is central to this study. After the first postnatal week, we saw differences in the architecture of the basal dendritic tree between layer 2a neurons and layer 2b neurons. When plotting the normalized cell depth in layer 2 against the total dendritic branch length (TDBL) of each neuron's basal tree, we observed a stable superficial to deep gradient of basal dendritic tree length and complexity over postnatal development [p1–p2 ($r = 0.62$, $p < 0.01$), p6–p8 ($r = 0.68$, $p < 0.01$), p12–p14 ($r = 0.84$, $p < 0.0001$), and >p30 ($r = 0.54$, $p < 0.01$); Spearman correlation test; Fig. 1*C*; Extended Data Fig. 1-1]. When using our positional grouping approach, the number of basal branches (NB) and the total basal dendritic branch length (BL) were significantly smaller in layer 2a than in layer 2b neurons starting in postnatal week 1 (see also Fig. 3*A*; NB: layer 2a vs layer 2b: p6–p8: $p < 0.001$, p12–p14: $p < 0.0001$, >p30: $p < 0.01$; total basal dendritic length: layer 2a vs layer 2b: p6–p8: $p < 0.01$, p12–p14: $p < 0.0001$, >p30: $p < 0.05$; ANOVA with Holm–Sidak's multiple comparisons test). We conclude that the morphologic parameter basal dendritic length justifies the distinction between a superficial (layer 2a) and deep (layer 2b) population of aPCx layer 2 neurons in our dataset.

Distinct growth phases in apical and basal dendrites

We chose a set of morphometric parameters to describe the growth of the apical (Fig. 2) and basal (Fig. 3)

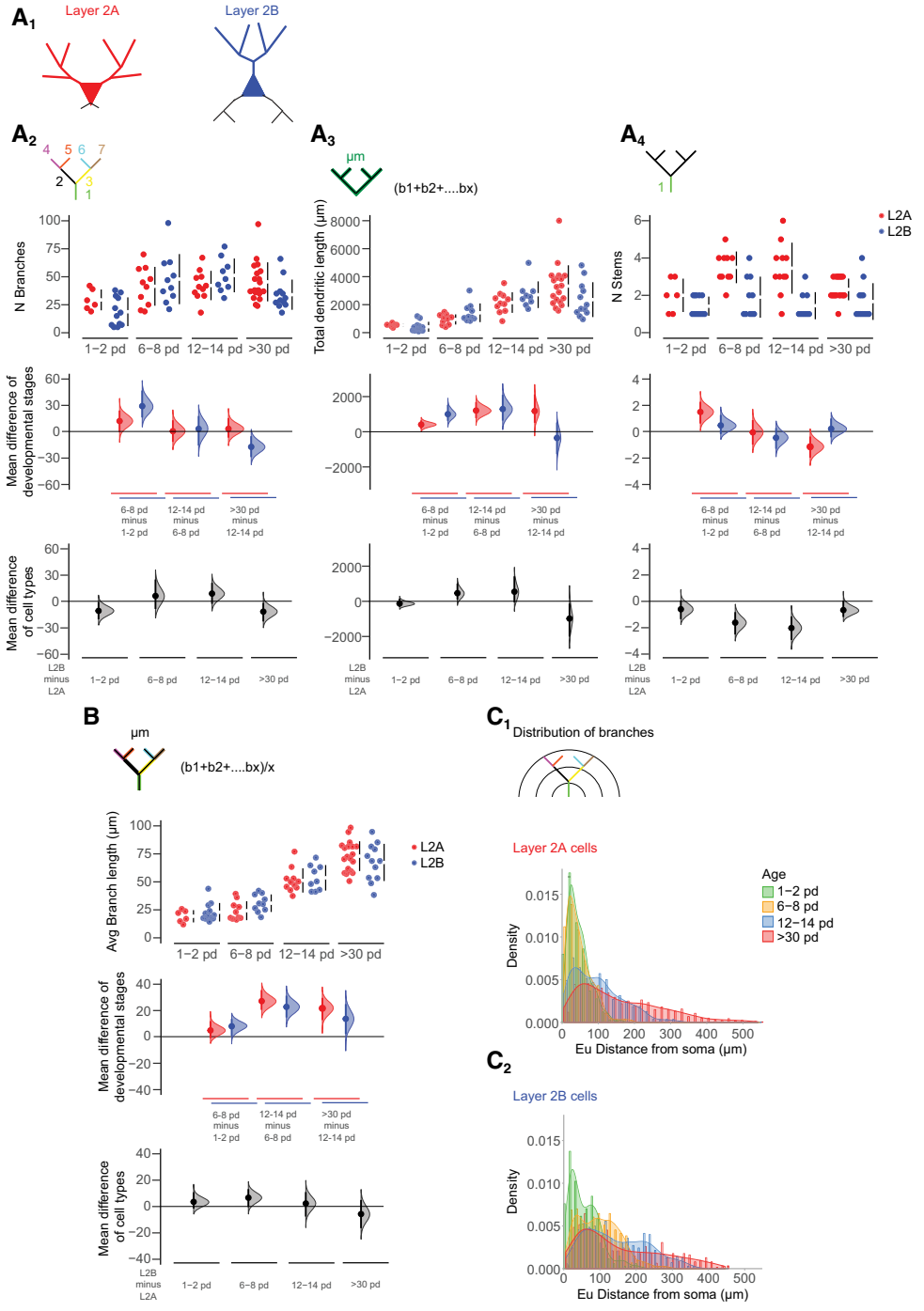
A1
Layer 2A
Layer 2B
A2
A3
µm
(b1+b2+....bx)
A4
N Branches
Total dendritic length (µm)
N Stems
L2A
L2B
1–2 pd
6–8 pd
12–14 pd
>30 pd
Mean difference of developmental stages
6-8 pd minus 1-2 pd
12-14 pd minus 6-8 pd
>30 pd minus 12-14 pd
Mean difference of cell types
L2B minus L2A
B
µm
(b1+b2+....bx)/x
Avg Branch length (µm)
C1
Distribution of branches
Layer 2A cells
Age
1–2 pd
6–8 pd
12–14 pd
>30 pd
Density
Eu Distance from soma (µm)
C2
Layer 2B cells

continued

Figure 2. Developmental changes in the morphology of the apical dendritic tree. ***A1***, Visual representation of layer 2a (L2A, top, red) and layer 2b (L2B, bottom, blue) neurons. Morphologic parameters are used to described growth patterns of the apical trees of these cells during development at four different ages (expressed as postnatal days, pd). Four measurements were extracted from the reconstructed cells and are displayed in Cumming estimation plots: (***A2***) total number of apical branches per cell; (***A3***) total apical dendritic length per cell; (***A4***) total number of apical stems per cell; and (***B***) average apical branch-length per cell in micrometers. The raw data are plotted on the upper axes; mean differences between developmental stages are plotted on the middle axes and mean differences between the cell types are plotted on the lower axes, as a bootstrap sampling distribution. Mean differences are depicted as dots and the 95% confidence intervals are indicated by the ends of the vertical error bars. Red dots represent layer 2a neurons (L2A), blue dots represent layer 2b neurons (L2B). ***C***, Densities of the distributions of apical branches for layer 2a (***C1***) and layer 2b (***C2***) are plotted as function of the Euclidean distance from the soma at four time windows: 1–2 pd (green), 6–8 pd (yellow), 12–14 pd (blue), and >30 pd (red). See Extended Data Table 1-2 for statistical details.

Figure Contributions: Laura Moreno-Velasquez performed the experiments. Laura Moreno-Velasquez, Malte Kaehne, and Friedrich W. Johenning analyzed the data.

dendritic tree: NB, TDBL, number of stems, average individual BL, and branch density as a function of distance from the soma. Using these parameters, we defined three distinct developmental phases. In apical dendrites of both layer 2a and layer 2b neurons, we observed the largest fractional increase in branch number in the first postnatal week (layer 2a: 75% of total increase in branch number; layer 2b: 90% of total increase in branch number; Fig. 2*A2*). For layer 2b neurons, we observed a significant increase in apical branch number between p0–p2 and p6–p8 (layer 2b neurons: p1–p2 vs p6–p8: $p < 0.001$, p12–p14 vs >p30: $p < 0.05$; ANOVA with Holm–Sidak's multiple comparisons test; Fig. 2*A2*). Layer 2a neurons displayed a significant addition of proximal stems in the first postnatal week only (layer 2a neurons: p1–p2 vs p6–p8: $p < 0.01$, p12–p14 vs >p30: $p < 0.01$; ANOVA with Holm–Sidak's multiple comparisons test; Fig. 2*A4*). Layer 2b neuron basal branches displayed a similar developmental pattern (Fig. 3*A2*). Here, we observed a statistically significant increase in branch number in the first postnatal week (layer 2b: 64% of total increase in branch number; Fig. 3*A2*). In the shorter and less complex basal tree of layer 2a neurons (Fig. 3*A*, bottom panels), significant branch addition was only evident when compared over the whole developmental period observed (layer 2b neurons: p1–p2 vs p6–p8: $p < 0.01$, p12–p14 vs >p30: $p < 0.05$; layer 2a neurons: p1–p2 vs p30: $p < 0.05$; ANOVA with Holm–Sidak's multiple comparisons test; Fig. 3*A2*).

After this initial determination of branch complexity by branch addition (developmental phase 1), dendrites grew by branch elongation (developmental phase 2). In layer 2a neurons, we observed statistically significant increases of the total apical dendritic BL in the second postnatal week and between weeks 2 and 5 (Fig. 2*A3*). In layer 2b apical dendrites, the TDBL increased significantly in the first and second postnatal weeks (layer 2a neurons: p6–p8 vs p12–p14: $p < 0.05$, p12–p14 vs >p30: $p < 0.05$; layer 2b neurons: p1–p2 vs p6–p8: $p < 0.05$, p6–p8 vs p12–p14: $p < 0.01$; ANOVA with Holm–Sidak's multiple comparisons test; Fig. 2*A3*). In basal dendrites of layer 2b neurons, we observed increases in TDBL in developmental phase 2 until p12–p14 (Fig. 3*A3*). In the shorter and less complex basal tree of layer 2a neurons, significant length growth was again only evident when comparing over the whole developmental period observed (layer 2a neurons: p1–p2 vs >p30: $p < 0.05$; layer 2b neurons: p0–p2 vs p6–p8: $p < 0.05$, p6–p8 vs p12–p14: $p < 0.001$, p12–p14 vs >p30: $p < 0.001$; ANOVA with Holm–Sidak's multiple comparisons test; Fig. 3*A3*).

Increases in the TDBL are a combined effect of branch addition and elongation of individual branch segments. The dichotomy between branch addition in developmental phase 1 and the length growth of existing branches in developmental phase 2 became apparent when examining the average BL per neuron (Figs. 2*B*, 3*B*). In layer 2a and layer 2b neuron apical and basal branches, the average BL per neuron did not increase in the first postnatal week. In the second postnatal week and between weeks 2 and 5, layer 2a and layer 2b neurons both displayed significant increases in the average apical BL per neuron (layer 2a neurons: p6–p8 vs p12–p14: $p < 0.0001$, p12–p14 vs >p30: $p < 0.0001$; layer 2b neurons: p6–p8 vs p12–p14: $p < 0.001$, p12–p14 vs >p30: $p < 0.05$; ANOVA with Holm–Sidak's multiple comparisons test; Fig. 2*B*).

Layer 2b basal branches exhibited a similar pattern, the average BL only increased significantly in the second postnatal week but not in the first postnatal week (Fig. 3*B*). In layer 2a neuron basal dendrites, length increase was only significant when comparing over the whole developmental period observed (layer 2b: p6–p8 vs p12–p14: $p < 0.001$; layer 2a: p1–p2 vs >p30: $p < 0.01$; ANOVA with Holm–Sidak's multiple comparisons test; Fig. 3*A3*).

It is obvious from Figure 3*B* that the relatively small length increase in layer 2a neuron basal dendrites predominantly occurred in the second postnatal week and between postnatal weeks 2 and 5. In sum, our measurements permitted us to clearly distinguish branch addition in developmental phase 1 followed by elongation of individual branch segments in developmental phase 2 for layer 2a and layer 2b dendrites.

We identified a third developmental phase in the interval between the end of the second postnatal week (p12–p14) and the fifth postnatal week (>p30). We observed a 34% reduction in the number of apical branches in layer 2b neurons and a 33% reduction in the number of stems in layer 2a neurons (Fig. 2*A2*,*A4*). In layer 2b neurons, this pruning was accompanied by a halt in the increase of TDBL (Fig. 2*A3*) despite a significant increase in the average BL per neuron (Fig. 2*B*). This resulted in a diverging developmental trajectory of the apical dendrite between layer 2a and layer 2b neurons. While the TDBL was similar

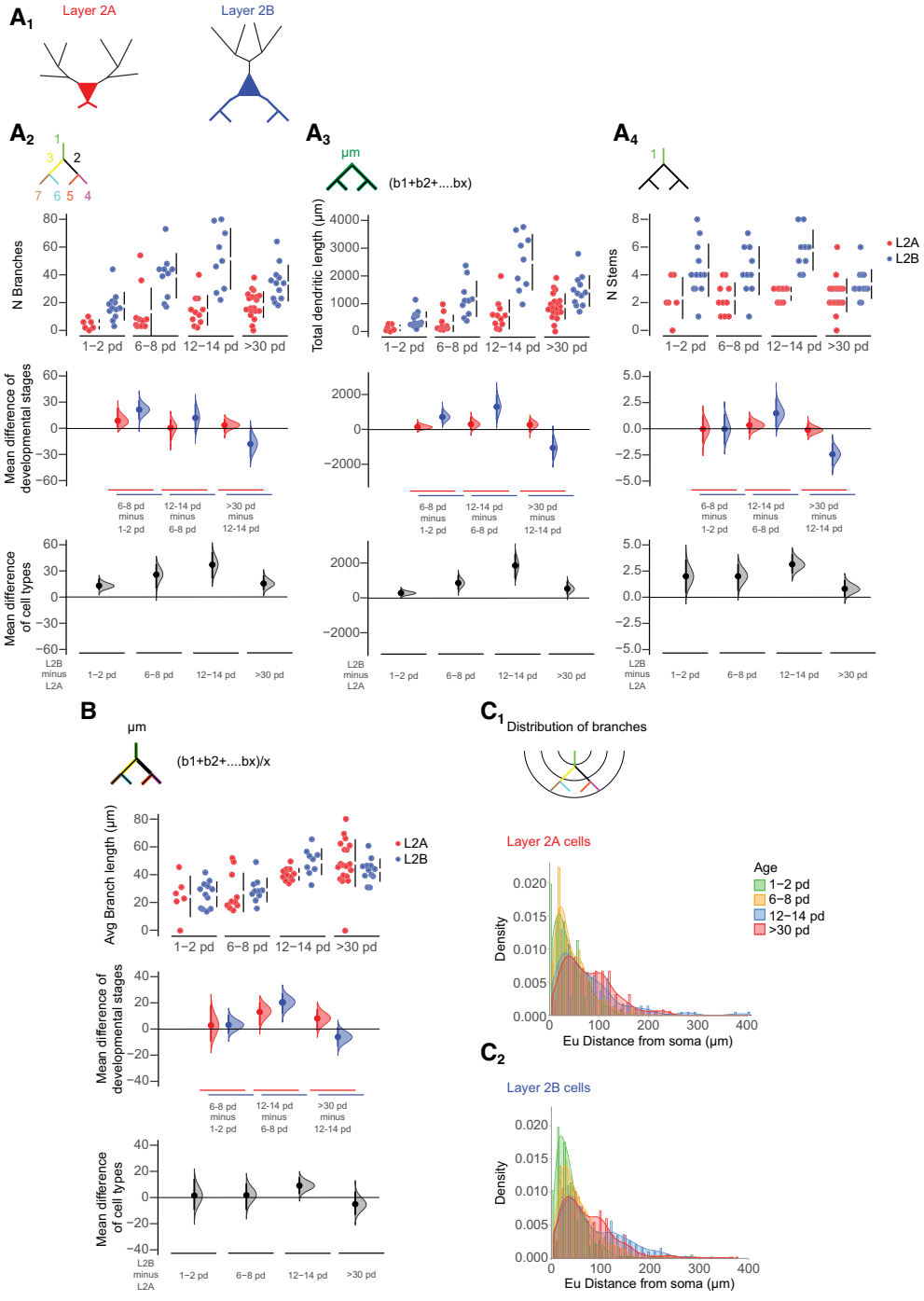
A1
Layer 2A
Layer 2B
A2
A3
µm
(b1+b2+....bx)
A4
N Branches
Total dendritic length (µm)
N Stems
L2A
L2B
1–2 pd
6–8 pd
12–14 pd
>30 pd
Mean difference of developmental stages
6-8 pd minus 1-2 pd
12-14 pd minus 6-8 pd
>30 pd minus 12-14 pd
Mean difference of cell types
L2B minus L2A
B
µm
(b1+b2+....bx)/x
Avg Branch length (µm)
C1
Distribution of branches
Layer 2A cells
Age
Density
Eu Distance from soma (µm)
C2
Layer 2B cells

continued

Figure 3. Developmental changes in the morphology of the basal dendritic tree. ***A1***, Visual representation of layer 2a (L2A, top, red) and layer 2b (L2B, bottom, blue) neurons. Morphologic parameters are used to described growth patterns of the basal dendritic trees of layer 2a (L2A, red) and layer 2b (L2B, blue) neurons during development at four different ages (expressed as postnatal days, pd). Four measurements were extracted directly from the reconstructed cells and are shown in Cumming estimation plots: (***A2***) total number of basal branches per cell; (***A3***) total basal dendritic length per cell in micrometers; (***A4***) total number of basal stems per cell; and (***B***) average basal branch-length per cell in micrometers. The raw data are plotted on the upper axes; mean differences between developmental stages are plotted on the middle axes and mean differences between the cell types are plotted on the lower axes, as a bootstrap sampling distribution. Mean differences are depicted as dots and the 95% confidence intervals are indicated by the ends of the vertical error bars. Red dots represent layer 2a neurons (L2A), blue dots represent layer 2b neurons (L2B). ***C***, Densities of the distributions of basal branches for layer 2a (***C1***) and layer 2b (***C2***) are plotted as function of the euclidean distance from the soma at four time windows: p1–p2 (green), p6–p8 (yellow), p12–p14 (blue), and >p30 (red). See Extended Data Table 1-2 for statistical details.
Figure Contributions: Laura Moreno-Velasquez performed the experiments. Laura Moreno-Velasquez, Malte Kaehne, and Friedrich W. Johenning analyzed the data.

until week 2, the two different developmental patterns of layer 2a and layer 2b neurons resulted in a significantly shorter apical dendritic tree in layer 2b neurons at five weeks (layer 2a vs layer 2b at >p30: $p < 0.05$; ANOVA with Holm–Sidak's multiple comparisons test; Fig. 2*A3*). Similar to their apical dendrites, layer 2b neuron basal dendrites pruned significantly after p12–p14, both with respect to TDBL and branch number (Fig. 3*A2*,*A3*). Between postnatal weeks 2 and 5, we therefore defined a third developmental phase of pruning for apical and basal dendrites of layer 2b neurons and apical stems of layer 2a neurons.

To see how the three distinct developmental phases affected the spatial arrangement of branches, we plotted the distribution of branch densities as a function of distance from the soma. We observed differences between apical dendrites of layer 2a and layer 2b neurons during the first two postnatal weeks. In developmental phase 1, layer 2a neurons branched close to the soma, the distribution was single-peaked (Fig. 2*C1*). In contrast, layer 2b neurons also displayed a second peak of distal branching right after birth (p1–p2), and during the first developmental phase determining dendritic complexity (p6–p8; Fig. 2*C2*). During the second developmental phase of dendritic elongation, no branches were added in layer 2a and layer 2b neurons. At the same time, we observed a right shift of the peaks of apical branch density to larger distances from the soma. This indicated that length growth was not limited to dendritic tips but also affected intermediate branches. Pruning in developmental phase 3 resulted in a reduction of the second, distal peak of the layer 2b neurons, approximating the apical branch distributions of layer 2a and layer 2b neurons. The distribution of basal branch density as a function of distance from the soma was similar for both cell types, with a right shift for layer 2b neurons (Fig. 3*C*).

In sum, circuit-specific differences in dendritic development between layer 2a and layer 2b neurons were observed in developmental phases one (branch addition) and three (pruning). While differences in basal branch number between layer 2a and layer 2b neurons were determined in developmental phase 1, development of the apical dendritic tree diverged during pruning in phase 3.

Functional connectivity during early spontaneous network activity at the mesoscale population level reflects morphologic differences

The complexity of both the apical and the basal dendritic tree is determined in the first postnatal week by branch addition (developmental phase 1). As dendritic structure and neuronal activity are interdependent, our next aim was to compare neuronal activity patterns during the first postnatal week between layer 2a and layer 2b neurons.

We analyzed differences between the two cell types at the mesoscale population level during immature slow spontaneous network activity patterns. Similar to the somatosensory cortex, immature slow spontaneous network activity patterns in aPCx coexist with and can be triggered by sensory inputs starting at p0 (Hoffpauir et al., 2009; Leighton and Lohmann, 2016). In acute brain slices, slow spontaneous network activity is preserved as a default state of the intrinsic recurrent network (Rigas et al., 2015).

In the juvenile circuit, layer 2a neurons are less likely to be incorporated into recurrent circuits than layer 2b neurons (Suzuki and Bekkers, 2011; Wiegand et al., 2011). To date, it is unclear whether immature spontaneous network activity reflects mature connectivity patterns or acts as an unstructured global signal. Observing spontaneous network activity in the aPCx, we therefore next wanted to test whether immature spontaneous network activity early in development differentially incorporates layer 2a and layer 2b neurons. Here, we used data from Ai95-NexCre mice as this mouse line is specific for glutamatergic neurons. To assess functional connectivity between neurons, we identified all visible neurons (4755/50/39/23 neurons/fields of view/slices/mice). Based on Ca^{2+}-mediated changes of the fluorescence signals, events were defined as activity-related Ca^{2+} signals distinguishable from baseline noise following the criteria stated in Materials and Methods. Cells displaying events were defined as active. For neurons that were active, we extracted all events of each individual neuron. For each neuron and each event, we calculated which percentage of layer 2 neurons was coactive in the same field of view at the same time. These percentage values were then averaged over all events observed in a neuron. We plotted neuronal depth in layer 2 against the average percentage of coactive neurons in the whole layer 2 field of view. Coactivity was significantly stronger in the deep layer 2b neurons (deep third of layer 2) than in layer 2a neurons [superficial third of layer 2 (Fig. 4*D*); 1/3 layer 2 vs 3/3 layer 2: $p < 0.01$; unpaired t test]. This was even more pronounced for the small fraction of neurons recorded in layer 1b and in layer 3 (Fig. 4*C*). The degree of coactivity is an

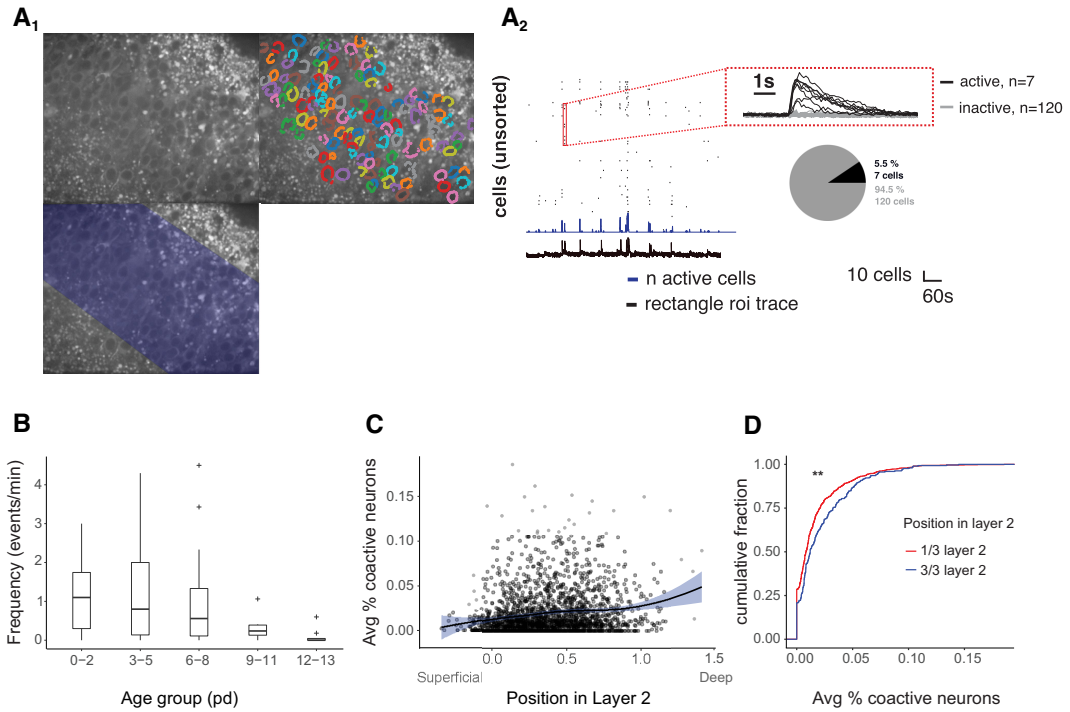

Figure 4. Comparison of spontaneous network activity in layer 2a and layer 2b neurons. ***A1***, Example of a baseline GCaMP-fluorescence image from an Ai95-NexCre mice. The field of view covers layer 2 in aPCx. Top right, Detected cells in layer 2. Bottom, Rectangular ROI defined by the upper and lower boundaries of layer 2 for detecting global activity. ***A2***, Corresponding traces from the global events measured from the rectangular ROI (fluorescence: black trace, bottom) and the active cells (raster plot, blue trace for number of active cells, red inset for fluorescent traces from individual neurons in raster plot). The proportion of active versus inactive cells is indicated by pie chart for one event. ***B***, Frequency of spontaneous events per minute measured at five different age groups (expressed as postnatal days, pd; $n = 70/59/36$ fields of view/slices/mice). ***C***, For each active neuron, the average percentage of coactive neurons (based on the total number of neurons in the field of view) was plotted against the position of the active neuron in layer 2 in the aPCx (data are fitted with a local polynomial regression and pooled from the first postnatal week). ***D***, Layer 2 was divided in three parts. Cumulative distribution of the average percentage of coactive neurons from ***C*** was plotted for the superficial third (red, 1/3 layer 2, corresponds to layer 2a neurons) and the deep third (blue, 3/3 layer 2, corresponds to layer 2b neurons); $^{**}p < 0.01$. See Extended Data Table 1-2 for statistical details.
Figure Contributions: Stephen Lenzi performed the experiments and analyzed the data.

indirect measure of functional connectivity. Already during the first postnatal week, we observed higher local functional connectivity in layer 2b than in layer 2a neurons. Morphologically, this scales with the more complex basal dendritic tree receiving more recurrent inputs (Haberly, 1985). We conclude that divergence of the basal dendritic tree complexity between layer 2a and layer 2b neurons is already evident in the first postnatal week and reflected by differences in functional connectivity during early spontaneous network activity.

Pruning in layer 1a during the early critical period of sensory plasticity

Next, we wanted to further understand differences in the developmental pattern of the apical dendritic tree. Here, the most pronounced differences occurred between the end of postnatal week 2 and the fifth postnatal week (developmental phase 3). In this period, we observed selective pruning of layer 2b neuron apical dendrites, which did not occur in layer 2a neurons (see Fig. 2).

The distinct organization of synaptic inputs to aPCx apical dendrites enabled us to relate pruning to specific circuits by grouping dendritic branches based on their position (layer 1a for branches receiving sensory inputs and layer 1b/2 for recurrent inputs). We therefore analyzed the growth and pruning patterns of apical dendrites with respect to the synaptic input layer the segments terminated in. Apical branches were categorized as branches terminating in layer 2, layer 1b (both recurrent), and layer 1a (sensory) for both cell types (Fig. 5*A*). Calretinin staining was used as a marker to delineate layer 1a (Fig. 1*A3*,*A4*).

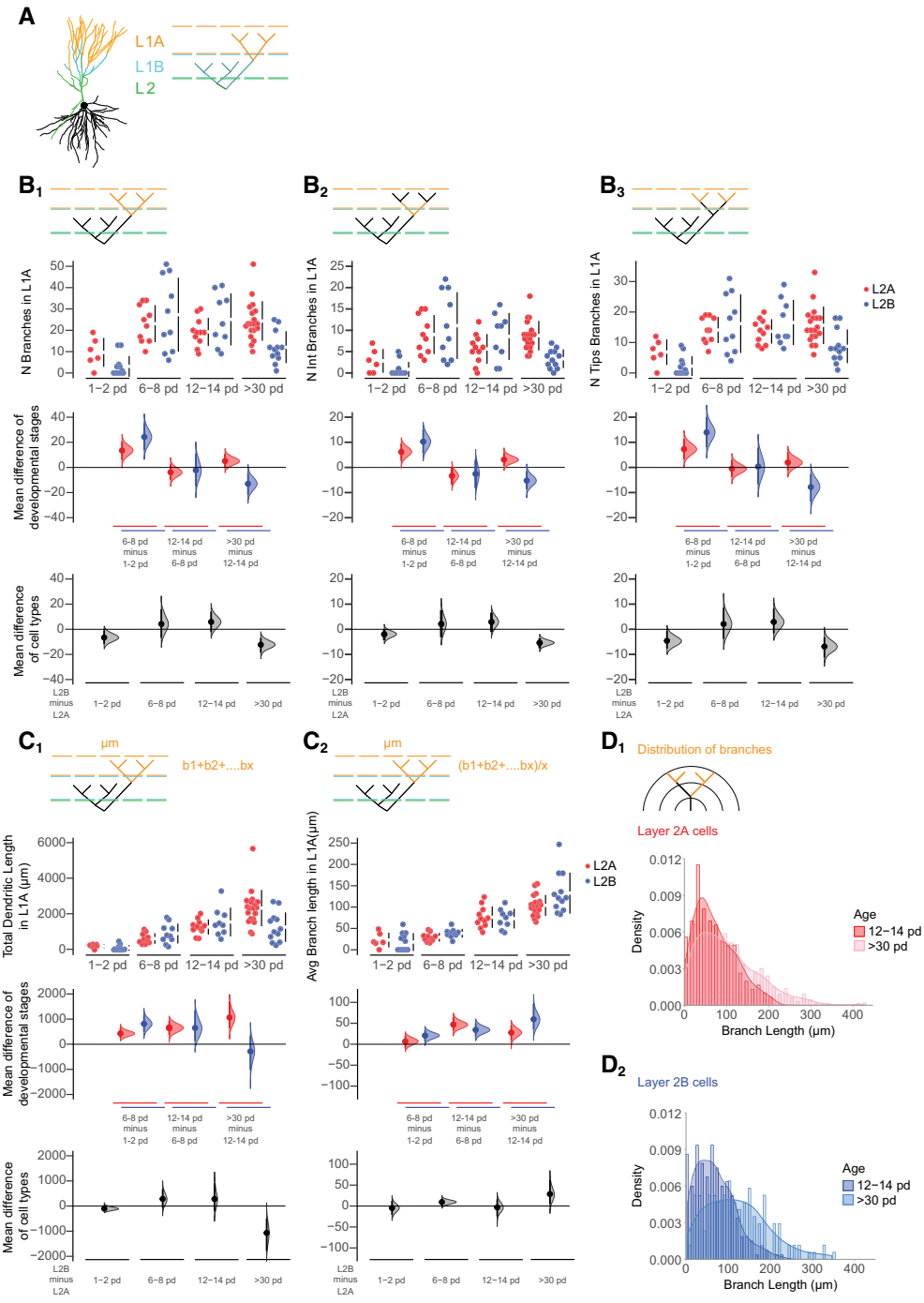
A
L1A
L1B
L2
B1
B2
B3
N Branches in L1A
N Int Branches in L1A
N Tips Branches in L1A
L2A
L2B
1–2 pd
6–8 pd
12–14 pd
>30 pd
Mean difference of developmental stages
6-8 pd minus 1-2 pd
12-14 pd minus 6-8 pd
>30 pd minus 12-14 pd
Mean difference of cell types
L2B minus L2A
C1
C2
µm
b1+b2+....bx
(b1+b2+....bx)/x
Total Dendritic Length in L1A (µm)
Avg Branch length in L1A(µm)
D1
Distribution of branches
Layer 2A cells
D2
Layer 2B cells
Density
Branch Length (µm)
Age
12–14 pd
>30 pd

continued

Figure 5. Differences in growth pattern of apical dendrites in response to layer-specific synaptic inputs. ***A***, Example of a reconstructed cell shows the classification of the apical dendrites into three categories: branches terminating in layer 2 (L2, green), layer 1b (L1B cyan), and layer 1a (L1A, orange). ***B***, Growth patterns of the apical branches terminating in layer 1a are shown in Cumming estimation plots, including total NB per cell (***B1***), total number of intermediate branches per cell (***B2***), total number of tips per cell (***B3***), total dendritic length per cell (***C1***), and average BL per cell (***C2***). The raw data are plotted on the upper axes; mean differences between developmental stages (expressed as postnatal days, pd) are plotted on the middle axes and mean differences between the cell types are plotted on the lower axes, as a bootstrap sampling distribution. Mean differences are depicted as dots and the 95% confidence intervals are indicated by the ends of the vertical error bars. Red dots represent layer 2a neurons (L2A), blue dots represent layer 2b neurons (L2B). ***D***, Densities of the distributions of the layer 1a branches for layer 2a (***D1***) and layer 2b (***D2***) neurons plotted as function of BL at two time windows: 12–14 pd (red and blue, respectively) and >30 pd (pink and light blue, respectively). See Extended Data Table 1-2 for statistical details and Extended Data Figure 5-1 for growth patterns in layer 1b and layer 2.

Figure Contributions: Laura Moreno-Velasquez performed the experiments. Laura Moreno-Velasquez, Malte Kaehne, and Friedrich W. Johenning analyzed the data.

While basal branches of layer 2b neurons displayed clear pruning (see Fig. 3), reduction of the proximal apical branches only receiving recurrent input in layers 1b and 2 did not reach statistical significance (Kruskal–Wallis test with Dunn's multiple comparison; Extended Data Fig. 5-1). Only in layer 2b neurons, distal branches that constituted sensory layer 1a circuits pruned significantly between p12–p14 and >p30 (layer 2b neurons: p12–p14 vs p30: $p < 0.05$; ANOVA with Holm–Sidak's multiple comparisons test; Fig. 5*B1*). Here, pruning resulted both in a significant reduction of the number of layer 1a intermediate branches and tips (intermediate branches: layer 2b neurons p12–p14 vs > p30: $p < 0.05$; tips: layer 2b neurons p12–p14 vs > p30: $p < 0.05$; ANOVA with Holm–Sidak's multiple comparisons test; Fig. 5*B2*,*B3*). Branch numbers in superficial layer 2a neurons remained stable over this developmental period (Fig. 5*B*). The reduction in branch number was accompanied by a significantly shorter layer 1a total dendritic length when comparing layer 2a and layer 2b neurons (layer 2a vs layer 2b neurons at >p30: $p < 0.001$; ANOVA with Holm–Sidak's multiple comparisons test; Fig. 5*C1*). Pruning was therefore limited to a specific compartment in a subpopulation of neurons.

To further understand circuit and cell-type-specific pruning of the apical dendrite, we compared the average individual BL per neuron in layer 1a of layer 2a and layer 2b neurons between postnatal weeks 2 and 5. We observed significant branch elongation of individual layer 1a branches for both cell types (Fig. 5*C2*). When comparing layer 2a and layer 2b neurons, the average layer 1a BL per neuron was similar after the second postnatal week. However, after the pruning phase, layer 1a branches in layer 2b neurons were significantly longer (p6–p8 vs p12–p14: layer 2a neurons: $p < 0.0001$, layer 2b neurons: $p < 0.05$; p12–p14 to <p30: layer 2a neurons: $p < 0.01$ layer 2b neurons: $p < 0.001$; layer 2a neurons vs layer 2b neurons at >p30: $p < 0.05$; ANOVA with Holm–Sidak's multiple comparisons test; Fig. 5*C2*). When analyzing the distribution change of average BLs during the pruning phase, we saw a shift toward longer 1a branches in both cell types, with a more pronounced shift in 2b neurons (Fig. 5*D1*,*D2*). In layer 2a neurons, we did not observe layer 1a branch loss. Here, the length increase could be explained by branch elongation, which is a consequence of cortical growth. However, when interpreting the distribution shift in layer 2b neurons, we had to consider the pruning-related branch loss. The stronger right shift of the distribution toward longer branches in comparison to layer 2a neurons was accompanied by a significant decrease in branch number. This implied that pruning of sensory layer 1a branches in layer 2b neurons predominantly affected short branches or that surviving branches underwent enhanced length growth.

NMDA-spikes are more pronounced in layer 1a dendrites of layer 2b neurons

We next investigated the connection between the preferential pruning of short layer 1a branches and the recent discovery of supralinear dendritic integration of sensory inputs in layer 1a branches of PCx layer 2b neurons. As was recently shown in rat aPCx layer 2b neurons, clustering of synaptic inputs on the same branch as opposed to distributed input to the entire dendritic arbor significantly modified the stimulus-response behavior. Clustered (same branch) input triggered supralinear stimulus-response behavior defined as NMDAR-mediated Ca^{2+} spikes (NMDA-spikes). Supralinear stimulus-response behavior resulted in large local dendritic depolarization and associated Ca^{2+} influx. Distributed inputs of similar strength evoked substantially lower levels of dendritic depolarization (Kumar et al., 2018).

We would like to relate these findings to our morphologic data. Our experiments demonstrated that during postnatal development, pruning of the apical dendrites was mainly based on the loss of short layer 1a branches (Fig. 5*C*,*D*). We hypothesize that the selection bias toward longer branch segments in the sensory synaptic input space of layer 2b neurons could be a developmental mechanism supported by supralinear stimulus-response behavior. A selection bias for long branches would optimize the efficiency of the neuronal input-output function by promoting the growth and survival of branches with a higher probability of receiving clustered (same branch) input.

So far, NMDAR-dependent supralinear stimulus-response behavior has only been demonstrated in the aPCx of rats older than four weeks (Kumar et al., 2018). Here, we hypothesize that supralinear stimulus-response behavior may play a role in the developmental branch selection observed in layer 1a dendrites of layer 2b neurons during the critical period (p12–p14 to >p 30). To substantiate our hypothesis, we first wanted to test whether supralinear stimulus-response behavior also occurs in in

distal apical layer 1a dendrites of layer 2b neurons during postnatal week 3. We chose a developmental interval between our morphologic observation points (p12–p14 and >p30) as we propose that this is the time interval where supralinear stimulus-response behavior has an impact on the pruning mechanism. In contrast to layer 2b neurons, layer 2a neurons did not show pruning of short branches but equally distributed growth. If supralinear dendritic stimulus-response behavior enhanced selective pruning in distal apical dendrites of layer 2b neurons, another experimentally testable prediction would be an absence of supralinear stimulus-response behavior in layer 2a neurons.

We therefore performed combined somatic whole cell patch clamp recordings and two-photon Ca^{2+} imaging in apical layer 1a branches of layer 2a ($n = 5/5/5$, neurons/slices/mice) and layer 2b ($n = 5/5/5$, neurons/slices/mice) neurons. Synaptic stimulation was achieved by focal electrical stimulation with θ-glass electrodes (Fig. 6*A4*,*B4*). Using Ca^{2+} imaging, we first identified a focal stimulation spot. Stimulation strength was then linearly increased. When plotting the area under the curve (AUC) of the EPSP in layer 2b neurons, we observed a distinct supralinear increase at specific stimulation strengths, which was abolished after washing in of the NMDAR-antagonist APV (Fig. 6*A3*). In addition, this increase displayed the typical shape of an NMDA-spike (Fig. 6*A1*). We performed Ca^{2+} imaging in parallel and could further observe that the nonlinear enhancement of the EPSP AUC was accompanied by a branch-specific increase in spatial spread and amplitude of the Ca^{2+} transient (Fig. 6*A5*). These hallmarks of supralinear dendritic NMDA-spikes were not observed in layer 2a neurons (Fig. 6*B*). Next, we plotted the AUC and the amplitude of layer 2a and layer 2b neuron EPSPs before and after wash-in of APV. We observed a significant decrease of both parameters in layer 2b neurons. In contrast, NMDAR-block by APV did not affect AUCs and amplitudes of EPSPs in layer 2a neurons (layer 2b, AUC: pre vs post: $p < 0.05$; layer 2a, pre vs post: $p = 0.18$; amplitude: layer 2a, pre vs post: $p < 0.05$; layer 2b, pre vs post: $p = 0.7$; paired *t* test; Fig. 6*C1*,*C2*). At the stimulation site, the stimulation-evoked Ca^{2+} signal of both layer 2a and layer 2b neurons was significantly reduced by APV (layer 2b, pre vs post: $p < 0.01$; layer 2a, pre vs post: $p < 0.05$; ratio paired *t* test; Fig. 6*D*). Under NMDAR-block by APV, the AUC and the amplitude of the EPSP constitute a readout of the AMPA-type glutamate receptor-mediated depolarization. Consequently, the absolute value of the AUC and the amplitude in APV reflected the synaptic input strength of our stimulation. These values were not significantly different between layer 2a and layer 2b neurons in our sample, indicating comparable stimulation strength for both cell types (AUC: layer 2a post vs layer 2b post: $p = 0.92$; amplitude: layer 2a post vs layer 2b post: $p = 0.25$, *t* test; Fig. 6*C*).

We conclude that, in contrast to layer 2b neurons, layer 2a neurons do not display supralinear stimulus-response behavior in layer 1a at comparable input strengths. In layer 2b neurons, supralinear stimulus-response behavior can be observed during the developmental period of dendritic pruning of short dendritic segments. In layer 2a neurons, we neither observe pruning nor supralinear stimulus-response behavior in the same developmental period.

We next applied computational modeling to test whether the probability of supralinear integration by clustered inputs could indeed scale with BL over the range of BLs measured in this study. As a quantitative framework, we used the range of average BLs we observed at the beginning of the critical period (p12–p14; 40–110 μm). The average TDBL (1800 μm) was set constant for all model neurons. We estimated the layer 1a input density based on a recent comprehensive quantitative description of mouse piriform cortex (Srinivasan and Stevens, 2018). Based on Srinivasan and Stevens, we extrapolated that the whole population of 3700 bulbar glomeruli makes 2366 synapses with each individual neuron. Consequently, one glomerulus makes on average 0.64 synapses with each neuron. A total of 109 coincidently activated glomeruli would therefore activate 70 synapses on a layer 2b neuron, which we defined as the upper limit of coincident inputs. Figure 7*B* displays the results of our calculation. We plotted the probability of dendritic NMDA-spikes evoked by clustering of >10 synapses on an individual branch as a function of the average BL per neuron. This was repeated for different numbers of coincident synaptic inputs (for details, see Materials and Methods). The dendritic spike probability increased with increasing BL. Within our parameter space, clustering probability and the resulting dendritic spiking increased from close to 0% to up to 17% when comparing the shortest and longest average BL we observed in our dataset. Quantitatively, our results suggest that, during our developmental time window, dendritic NMDA-spikes are more likely to occur in long dendritic segments than short ones. It is therefore plausible that the supralinear stimulus-response behavior observed exclusively in layer 2b neurons could constitute a selection mechanism optimizing the efficiency of the neuronal input-output function. This would occur by promoting the growth and survival of branches with a higher probability of receiving clustered (same branch) input.

Discussion

Here, we performed a morphometric and functional analysis of postnatal dendritic development in aPCx sensory and recurrent circuits. We compared developmental patterns of excitatory neurons in the sublayers 2a and 2b. The two neighboring sublayers differ with respect to sensory and recurrent wiring. We could identify a timeline defined by three developmental phases: (1) branch addition (developmental phase 1, postnatal week 1); (2) branch elongation (developmental phase 2, postnatal week 2); and (3) branch pruning (developmental phase 3, postnatal weeks 3–5). We discovered circuit and sublayer-specific differences in dendritic development in developmental phases 1 and 3. In developmental phase 1, layer 2a neuron basal dendrites incorporated in recurrent circuits branched significantly less than layer 2b neuron basal dendrites. This was accompanied by lower functional connectivity of layer 2a neurons during spontaneous immature network activity. In developmental phase 3,

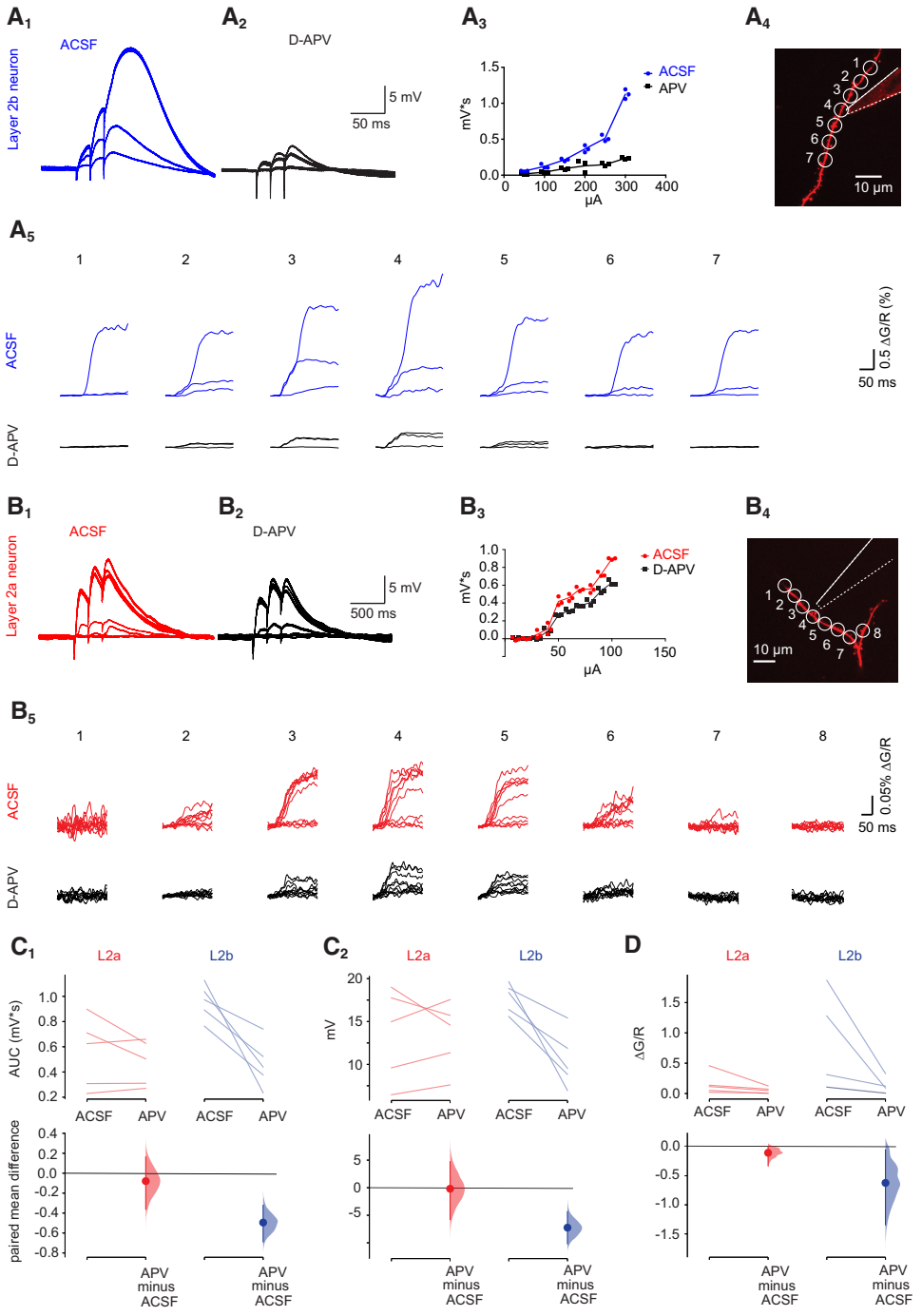
A1
A2
A3
A4
ACSF
D-APV
Layer 2b neuron
5 mV
50 ms
mV*s
μA
ACSF
APV
10 μm
A5
1
2
3
4
5
6
7
ACSF
D-APV
0.5 ΔG/R (%)
50 ms
B1
B2
B3
B4
Layer 2a neuron
5 mV
500 ms
D-APV
8
0.05% ΔG/R
C1
C2
D
L2a
L2b
AUC (mV*s)
mV
ΔG/R
paired mean difference
APV minus ACSF

continued

Figure 6. Dendritic NMDA-spikes can only be observed in layer 2b neurons. Representative layer 2b neuron (***A***) and representative layer 2a neuron (***B***). ***A1***, ***B1***, Overlay of electric responses measured at the soma on electrical stimulation with linear strength increase in layer 1a. ***A2***, ***B2***, Response to same stimulus after application of APV. ***A3***, ***B3***, Plot of stimulation strength against AUC from the same cell. ***A4***, ***B4***, Imaged dendritic branch and position of the stimulation electrode. ***A5***, ***B5***, Fluorescence traces of Ca2+ responses at ROIs outlined in A4/B4 under baseline conditions (upper rows, blue and red) and after application of APV (lower rows, black). Increasing stimulation strengths are overlaid. ***C***, ***D***, Cell-type-specific changes to NMDAR-block with APV are plotted as Cumming estimation plots. The raw data are plotted on the upper axes, each pair is connected by a line; each mean difference is plotted on the lower axes as a bootstrap sampling distribution. Mean differences are depicted as dots and the 95% confidence intervals are indicated by the ends of the vertical error bars. Red dots represent layer 2a neurons (L2a), blue dots represent layer 2b neurons (L2b). ***C1***, AUC before and after application of APV in layer 2a neurons (L2a, red) and layer 2b neurons (L2b, blue). ***C2***, EPSP amplitude before and after application of APV in layer 2a neurons (red) and layer 2b neurons (blue). ***D***, Fluorescent Ca^{2+} response before and after application of APV in layer 2a neurons (red) and layer 2b neurons (blue). Please note that we measured Ca^{2+} responses in five layer 2b neurons; however, the datapoints of two measurements were very close and occlude each other. See Extended Data Table 1-2 for statistical details.

Figure Contributions: Hung Lo performed the experiments and analyzed the data.

pruning of apical dendrites receiving layer 1a sensory inputs was only observed in layer 2b neurons, but not in layer 2a neurons. Pruning was clearly biased toward shorter dendritic branches. Using electrophysiology, Ca^{2+} imaging and modeling, we demonstrated how NMDAR-dependent supralinear stimulus-response behavior during phase 3 could support the survival and growth of long dendritic branches. Nonlinear dendritic properties could therefore be involved in dendritic development.

Distinction between layer 2a and layer 2b neurons

Distinguishing principle cell types in layer 2 poses a "lumping versus splitting" problem. Our hard segregation into layer 2a and layer 2b neurons based on location on the vertical axis qualifies as a "lumping" approach. Along the vertical axis of layer 2, we can distinguish at least two different types of principal cells based on their position, connectivity and morphology. Based on this distinction, principal neurons in layer 2 have been hypothesized to represent two parallel streams of olfactory information processing. Superficial neurons receive predominantly sensory inputs, whereas deep neurons receive both sensory and recurrent inputs (Suzuki and Bekkers, 2011; Wiegand et al., 2011). When segregating layers 2a and 2b as done here, this dichotomy is complicated by the observation that there seems to be a vertical gradient between so-called semilunar cells with no basal dendrites and superficial pyramidal cells with elaborate basal dendrites (Bekkers and Suzuki, 2013). Our detailed morphologic reconstructions and analysis support the idea of a continuum between these differentially wired types of neurons. We observed short or absent basal dendrites in layer 2a and increasing basal dendritic complexity in layer 2b. It is established that basal dendrites primarily receive local recurrent connections (Luskin and Price, 1983; Haberly, 1985). Therefore, basal dendritic complexity is a robust criterion for distinguishing between neuronal subtypes receiving different amounts of recurrent input. We were

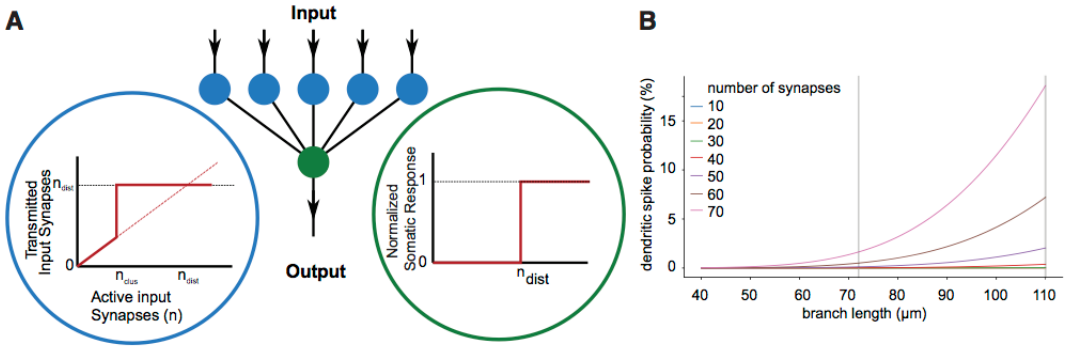

Figure 7. ***A***, Schematic neuron model as two-layered neural network, consisting of a dendritic activation layer (blue circles) and a somatic activation layer (green circles). The activation functions for the respective layers are shown in the insets. The activation of the soma is modeled as simple step function (if the input surpasses a certain threshold, the soma responds). The activation of every separate dendrite branch is modeled as an overlay of a linear response and a (nonlinear) step function, to mimic the excitability of dendritic branches. If a dendritic branch is excited (due to a large enough number of same branch active input synapses), it transmits, triggering a somatic response. ***B***, The response probability increases as function of the BL, an effect that becomes more apparent for different increasing numbers of active input synapses S.

Figure Contributions: Malte Kaehne performed all computations.

therefore able to differentiate between neurons in layer 2a and layer 2b on a vertical axis. This is important, as the intrinsic properties we observed along the vertical axis of layer 2 were more homogenous, which is different from previously published results in mice (Suzuki and Bekkers, 2006, 2011) and rats (Wiegand et al., 2011). Of all our age groups, our p12–p14 data most closely match the p13–p30 observation window used for the initial description of electrophysiological differences between superficial and deep layer 2 neurons in a mouse strain closely related to ours (Suzuki and Bekkers, 2006). While we found a similar trend regarding the difference in IR and AP threshold, our cell population segregated less clearly regarding the initial firing frequency. In addition, superficial neurons in our dataset were as hyperpolarized as deep neurons, whereas more depolarized superficial layer 2 neurons were recorded in earlier studies (Table 1; Extended Data Table 1-1). We can list a number of reasons that could underly the observed differences: differences in sampling (covering the whole extent of layer 2 in our case rather than focusing on the lower layer 2/3 and upper border as has been done previously, a more stringent definition of the deep layer 2 border that minimizes layer three neurons displaying more pronounced bursting); different positions on the anterior-posterior axis; holding potential (as opposed to earlier studies, our layer 2b neurons were characterized at –60 mV, where the burst-mediating T-type Ca^{2+} channels are most likely inactivated; Joksimovic et al., 2017); slicing angle and changes in intrinsic electrical properties when using a KMESO4-based intracellular solution as opposed to a KGLUC-based intracellular solution in our case (Kaczorowski et al., 2007).

Recent studies have extended the parameter space for splitting aPCx layer 2 neurons: long-range tracing studies identified layer-specific differences in axonal projection patterns (Chen et al., 2014; Diodato et al., 2016; Mazo et al., 2017). Different excitatory cell types have also been identified at the level of genetic markers. Genetic marker expression profiles of superficial neurons constituting layer 2a further support the “hard” location-based segregation principle applied here, as, based on published representative examples, they clearly seem to delineate a layer2a/layer2b border (Diodato et al., 2016; Choy et al., 2017; Bolding et al., 2019).

Critical period imprinting and pruning of layer 2b neuron dendrites in the non-topographic aPCx

The aPCx is a sensory brain region with a simple and evolutionary conserved structure that predates the development of the sensory neocortex (Bekkers and Suzuki, 2013). A central difference between sensory neocortex (auditory, visual, and somatosensory) and the aPCx is the spatial organization of afferent input. Sensory neocortex is a topographic circuit: nearby peripheral neurons share similar and predictable representations of sensory space and contact neighboring cortical neurons. These neighboring neurons have a high degree of local connectivity. In contrast, the PCx is a distributed, non-topographic circuit, where both the representation of sensory space and the recurrent connectivity are unpredictable and dispersed (Srinivasan and Stevens, 2018). This diffuse organization of the palaeocortical PCx is likely to reflect the primordial structure of cerebral cortices in reptiles before the evolution of isocortex in synapsids and later mammals (Fournier et al., 2015). These differences in the afferent input structure could affect dendritic growth patterns in palaeocortex and neocortex. In the following, we would therefore like to compare our data with published neocortical patterns of dendritic growth.

The determination of branch complexity during the first postnatal week corresponds to dendritic growth patterns identified in layer 2/3 and layer 5 pyramidal neurons in rodent neocortex (Petit et al., 1988; Maravall et al., 2004; Romand et al., 2011). The determination of branch complexity in the first postnatal week can therefore be considered a common design principle of neocortex and palaeocortex.

As in our palaeocortical dataset, length increase of neocortical dendrites was significant between the first and second postnatal week both in basal and apical dendrites. In the neocortex, there was no further increase in the period until p30 (Petit et al., 1988; Romand et al., 2011). The developmental trajectories of neocortex and palaeocortex diverge in developmental phase 3 during the critical period of sensory plasticity in the aPCx (between p12–p14 and >p30): in the palaeocortical aPCx, we observed a reduction in total dendric length and in dendritic branch number in apical and basal dendrites between p12–p14 and p30. In neocortical layer 5 neurons, a decrease in branch number was observed earlier, before the onset of the critical period between p7 and p14 in apical but not in basal dendrites and was attributed to filopodial, not dendritic pruning (Romand et al., 2011).

We propose that an overabundance of dendrites at the beginning of the critical period in aPCx could be a consequence of the requirements of a non-topographic afferent input structure. Overabundance of distal apical layer 1a dendrites increases the combinatorial space for different glomerular input combinations. A surplus of basal dendrites results in more recurrent connections. We would have a larger probability of generating circuit motifs of recurrently connected neurons sharing similar sensory inputs. The enlarged combinatorial space maybe necessary in a distributed circuit like the PCx. In contrast, the topographic neocortex displays local clustering of similar inputs. This will result in a higher probability of the clustering of similar inputs on interconnected neurons. An effect of neocortical topographical organization may therefore be the effective wiring of significant features of sensory space. This would obviate the need for the metabolically expensive generation of superfluous dendritic branches during neocortical development. In the palaeocortical aPCx, the overabundance of dendrites combined with pruning could therefore enhance the initial combinatorial space and compensate for the lack of effective wiring by topography biases. Interestingly, the time window of pruning in layer 1a matches the critical period of NMDAR-dependent circuit-specific sensory synaptic plasticity in layer 1a (Franks Kevin and Isaacson, 2005; Poo and Isaacson, 2007). We therefore propose that in layer 2b neurons, the critical period in the aPCx is accompanied by circuit-specific pruning

and remodeling of the distal apical dendritic tree receiving sensory inputs in layer 1a. In the future, it will be interesting to test whether initial dendritic overabundance followed by pruning is a general feature of non-topographically ordered cortices.

Possible contribution of supralinear dendritic integration to pruning

In layer 2b neurons, the enlargement of the olfactory coding space at the beginning of the critical period is followed by a reduction of dendritic branches. Here, we hypothesize that dendritic NMDAR-dependent supralinear stimulus-response behavior could serve as an underlying mechanism for this pruning process. Our rationale is that assuming constant synaptic density in layer 1a, longer dendritic branches will result in a higher probability for regenerative NMDA-spikes evoked by clustered inputs. This is backed by a recent publication demonstrating that inputs clustered on the same layer 1a branch in aPCx result in supralinear integration regardless of the distance between the inputs. In addition, large NMDAR-mediated Ca^{2+} signals occur during NMDA-spikes (Kumar et al., 2018). NMDAR-mediated Ca^{2+} signals are generally considered to promote dendritic growth during development (Konur and Ghosh, 2005). Our data therefore are compatible with an NMDA-spike-dependent selection and optimization process for apical dendritic layer 1a branches of layer 2b neurons. NMDA-spikes occur with a higher probability on longer branches, the related Ca^{2+} rise would serve as a dendritotrophic signal. Such a mechanism could promote the observed survival and elongation of long branches at the expense of short branches. The result would be the structural self-amplification of dendritic NMDA-spikes by promoting branches with a higher probability for clustered inputs.

Although our Ca^{2+} imaging data in layer 1a strongly suggest local dendritic NMDA-spikes in layer 1a, our experiments do not exclude a significant contribution of recurrent inputs to the enlarged EPSP amplitudes we interpret as dendritic NMDA-spikes. With respect to pattern completion in the aPCx, such a mechanism is plausible. Supralinear stimulus-response behavior of layer 1a input evoked by coincident sensory and recurrent inputs recruited by our extracellular stimulation would also generate large local Ca^{2+} transients in the activated dendritic branches. This would both be the case when the inputs share the same (long) branch and project onto different branches. It is therefore also possible that supralinear stimulus-response behavior could be based on coincident activity between distal and proximal dendritic compartments. The supralinear integration of sensory and recurrent inputs could serve as a plasticity inducing coincidence detection mechanism. This mechanism would be comparable to the plateau potential evoked by coincident proximal and distal inputs in hippocampal CA1 pyramidal neurons (Takahashi and Magee, 2009). In the aPCx, such a mechanism would amplify synaptic connections between ensembles of recurrently connected neurons that share similar sensory inputs. Interestingly, we also observed an overabundance of the recurrently connected basal dendrites in layer 2b neurons. These basal dendrites underwent pruning together with layer 1a dendrites. It is tempting to speculate that pruning skips apical and basal branches of interconnected layer 2b neurons sharing similar sensory inputs. This could optimize the input-output function of dendritic branches coding for relevant features in interconnected neurons sharing sensory and recurrent inputs. Ideally, longitudinal *in vivo* studies of dendritic Ca^{2+} dynamics and the related dendritic growth during the critical period would be needed to further support this hypothesis.

In contrast, layer 2a neuron apical dendrites in layer 1a do neither display supralinear stimulus-response behavior of layer 1a inputs nor pruning. In addition, they have a larger dendritic tree in the sensory layer 1a. This fits well with the stronger incorporation into sensory circuits these neurons display (Suzuki and Bekkers, 2011; Wiegand et al., 2011) and may result in larger olfactory receptive fields that are developmentally hardwired.

In sum, we provide evidence for circuit-specific mechanisms of dendritic development in the aPCx. We demonstrated that different developmental trajectories of the dendritic tree in layer 2a and layer 2b neurons relate to differences in circuit incorporation. Our data therefore support the concept that structural and functional differences between layer 2a and layer 2b neuron dendritic trees determine their distinct functions in the aPCx.

References

Bekkers JM, Suzuki N (2013) Neurons and circuits for odor processing in the piriform cortex. Trends Neurosci 36:429–438.

Bolding KA, Nagappan S, Han B, Wang F, Franks KM (2019) Pattern recovery by recurrent circuits in piriform cortex. bioRxiv 51:418–458.

Chen CF, Zou DJ, Altomare CG, Xu L, Greer CA, Firestein SJ (2014) Nonsensory target-dependent organization of piriform cortex. Proc Natl Acad Sci USA 111:16931–16936.

Choy JMC, Suzuki N, Shima Y, Budisantoso T, Nelson SB, Bekkers JM (2017) Optogenetic mapping of intracortical circuits originating from semilunar cells in the piriform cortex. Cereb Cortex 27:589–601.

Demir R, Haberly LB, Jackson MB (2001) Epileptiform discharges with in-vivo-like features in slices of rat piriform cortex with longitudinal association fibers. J Neurophysiol 86:2445–2460.

Diodato A, de Brimont MR, Yim YS, Derian N, Perrin S, Pouch J, Klatzmann D, Garel S, Choi GB, Fleischmann A (2016) Molecular signatures of neural connectivity in the olfactory cortex. Nat Commun 7:12238.

Feng L, Zhao T, Kim J (2015) Neutube 1.0: a new design for efficient neuron reconstruction software based on the swc format. eNeuro 2:ENEURO.0049-14.2014.

Fournier J, Müller CM, Laurent G (2015) Looking for the roots of cortical sensory computation in three-layered cortices. Curr Opin Neurobiol 31:119–126.

Franks Kevin M, Isaacson JS (2005) Synapse-specific downregulation of NMDA receptors by early experience: a critical period for plasticity of sensory input to olfactory cortex. Neuron 47:101–114.

Goebbels S, Bormuth I, Bode U, Hermanson O, Schwab MH, Nave K-A (2006) Genetic targeting of principal neurons in neocortex and hippocampus of NEX-Cre mice. genesis 44:611–621.

Haberly LB (1985) Neuronal circuitry in olfactory cortex: anatomy and functional implications. Chem Senses 10:219–238.

Hagiwara A, Pal SK, Sato TF, Wienisch M, Murthy VN (2012) Optophysiological analysis of associational circuits in the olfactory cortex. Front Neural Circuits 6:18.

Ho J, Tumkaya T, Aryal S, Choi H, Claridge-chang A (2019) Moving beyond P values: data analysis with estimation graphics. Nat Methods 16:565–566.
Hoffpauir BK, Marrs GS, Mathers PH, Spirou GA (2009) Does the brain connect before the periphery can direct?: a comparison of three sensory systems in mice. Brain Res 1277:115–129.
Johenning FW, Beed PS, Trimbuch T, Bendels MHK, Winterer J, Schmitz D (2009) Dendritic compartment and neuronal output mode determine pathway-specific long-term potentiation in the piriform cortex. J Neurosci 29:13649–13661.
Joksimovic SM, Eggan P, Izumi Y, Joksimovic SL, Tesic V, Dietz RM, Orfila JE, DiGruccio MR, Herson PS, Jevtovic-Todorovic V, Zorumski CF, Todorovic SM (2017) The role of T-type calcium channels in the subiculum: to burst or not to burst? J Physiol 595:6327–6348.
Kaczorowski CC, Disterhoft J, Spruston N (2007) Stability and plasticity of intrinsic membrane properties in hippocampal CA1 pyramidal neurons: effects of internal anions. J Physiol 578:799–818.
Kanari L, Ramaswamy S, Shi Y, Morand S, Meystre J, Perin R, Abdellah M, Wang Y, Hess K, Markram H (2019) Objective morphological classification of neocortical pyramidal cells. Cereb Cortex 29:1719–1735.
Konur S, Ghosh A (2005) Calcium signaling and the control of dendritic development. Neuron 46:401–405.
Kumar A, Schiff O, Barkai E, Mel BW, Poleg-Polsky A, Schiller J (2018) NMDA spikes mediate amplification of inputs in the rat piriform cortex. Elife 7:e38446.
Lanoue V, Cooper HM (2018) Branching mechanisms shaping dendrite architecture. Dev Biol 451:1–9.
Leighton AH, Lohmann C (2016) The wiring of developing sensory circuits—from patterned spontaneous activity to synaptic plasticity mechanisms. Front Neural Circuits 10:219.
Luskin MB, Price J (1983) The laminar distribution of intracortical fibers originating in the olfactory cortex of the rat. J Comp Neurol 216:292–302.
Madisen L, Garner AR, Shimaoka D, Chuong AS, Klapoetke NC, Li L, van der Bourg A, Niino Y, Egolf L, Monetti C, Gu H, Mills M, Cheng A, Tasic B, Nguyen TN, Sunkin SM, Benucci A, Nagy A, Miyawaki A, Helmchen F, et al. (2015) Transgenic mice for intersectional targeting of neural sensors and effectors with high specificity and performance. Neuron 85:942–958.
Maravall M, Koh IYY, Lindquist WB, Svoboda K (2004) Experience-dependent changes in basal dendritic branching of layer 2/3 pyramidal neurons during a critical period for developmental plasticity in rat barrel cortex. Cereb Cortex 14:655–664.
Martin-Lopez E, Ishiguro K, Greer CA (2019) The laminar organization of piriform cortex follows a selective developmental and migratory program established by cell lineage. Cereb Cortex 29:1–16.
Mazo C, Grimaud J, Shima Y, Murthy VN, Geoffrey Lau C (2017) Distinct projection patterns of different classes of layer 2 principal neurons in the olfactory cortex. Sci Rep 7:8282.
Pachitariu M, Stringer C, Schröder S, Dipoppa M, Rossi LF, Carandini M, Harris KD (2017) Suite2p: beyond 10,000 neurons with standard two-photon microscopy. bioRxiv. doi:https://doi.org/10.1101/061507.
Petit TL, LeBoutillier JC, Gregorio A, Libstug H (1988) The pattern of dendritic development in the cerebral cortex of the rat. Brain Res 469:209–219.
Poirazi P, Brannon T, Mel BW (2003) Pyramidal neuron as two-layer neural network. Neuron 37:989–999.
Poo C, Isaacson JS (2007) An early critical period for long-term plasticity and structural modification of sensory synapses in olfactory cortex. J Neurosci 27:7553–7558.
Rigas P, Adamos DA, Sigalas C, Tsakanikas P, Laskaris NA, Skaliora I (2015) Spontaneous Up states in vitro: a single-metric index of the functional maturation and regional differentiation of the cerebral cortex. Front Neural Circuits 9:219.
Romand S, Wang Y, Toledo-Rodriguez M, Markram H (2011) Morphological development of thick-tufted layer V pyramidal cells in the rat somatosensory cortex. Front Neuroanat 5:1–27.
Rueckl M, Lenzi SC, Moreno-Velasquez L, Parthier D, Schmitz D, Ruediger S, Johenning FW (2017) SamuROI, a Python-based software tool for visualization and analysis of dynamic time series imaging at multiple spatial scales. Front Neuroinform 11:1014–1059.
Sarma AA, Richard MB, Greer CA (2011) Developmental dynamics of piriform cortex. Cereb Cortex 21:1231–1245.
Scorcioni R, Polavaram S, Ascoli GA (2008) L-Measure: a web-accessible tool for the analysis, comparison and search of digital reconstructions of neuronal morphologies. Nat Protoc 3:866–876.
Sommer C, Straehle C, Kothe U, Hamprecht FA (2011) Ilastik: interactive learning and segmentation toolkit. Eighth IEEE International Symposium on Biomedical Imaging (ISBI 2011) Proceedings, pp 230–233. Chicago, IL: IEEE.
Srinivasan S, Stevens CF (2018) The distributed circuit within the piriform cortex makes odor discrimination robust. J Comp Neurol 526:2725–2743.
Suzuki N, Bekkers JM (2006) Neural coding by two classes of principal cells in the mouse piriform cortex. J Neurosci 26:11938–11947.
Suzuki N, Bekkers JM (2010) Inhibitory neurons in the anterior piriform cortex of the mouse: classification using molecular markers. J Comp Neurol 518:1670–1687.
Suzuki N, Bekkers JM (2011) Two layers of synaptic processing by principal neurons in piriform cortex. J Neurosci 31:2156–2166.
Takahashi H, Magee JC (2009) Pathway interactions and synaptic plasticity in the dendritic tuft regions of CA1 pyramidal neurons. Neuron 62:102–111.
Torben-Nielsen B (2014) An efficient and extendable Python library to analyze neuronal morphologies. Neuroinformatics 12:619–622.
Wiegand HF, Beed P, Bendels MHK, Leibold C, Schmitz D, Johenning FW (2011) Complementary sensory and associative microcircuitry in primary olfactory cortex. J Neurosci 31:12149–12158.
Wilson DA, Sullivan RM (2011) Cortical processing of odor objects. Neuron 72:506–519.

Extended Data

Extended Data Figure 1-1

Statistical analysis of the correlation between the total basal dendritic length and the vertical position of the cells in layer 2 at four time windows: 1-2 pd, 6-8 pd, 12-14 pd and >30 pd.

Data	Type of Test	Comparison	r	P-value	Significant
Figure 1C1	Spearman r	Location L2 vs Basal Length P1-2	0.6161	0.0065	**
Figure 1C2	Spearman r	Location L2 vs Basal Length P6-8	0.6793	0.001	***
Figure 1C3	Spearman r	Location L2 vs Basal Length P12-14	0.8358	< 0.0001	****
Figure 1C4	Spearman r	Location L2 vs Basal Length P>30	0.5442	0.0016	**

Extended Data Table 1-1

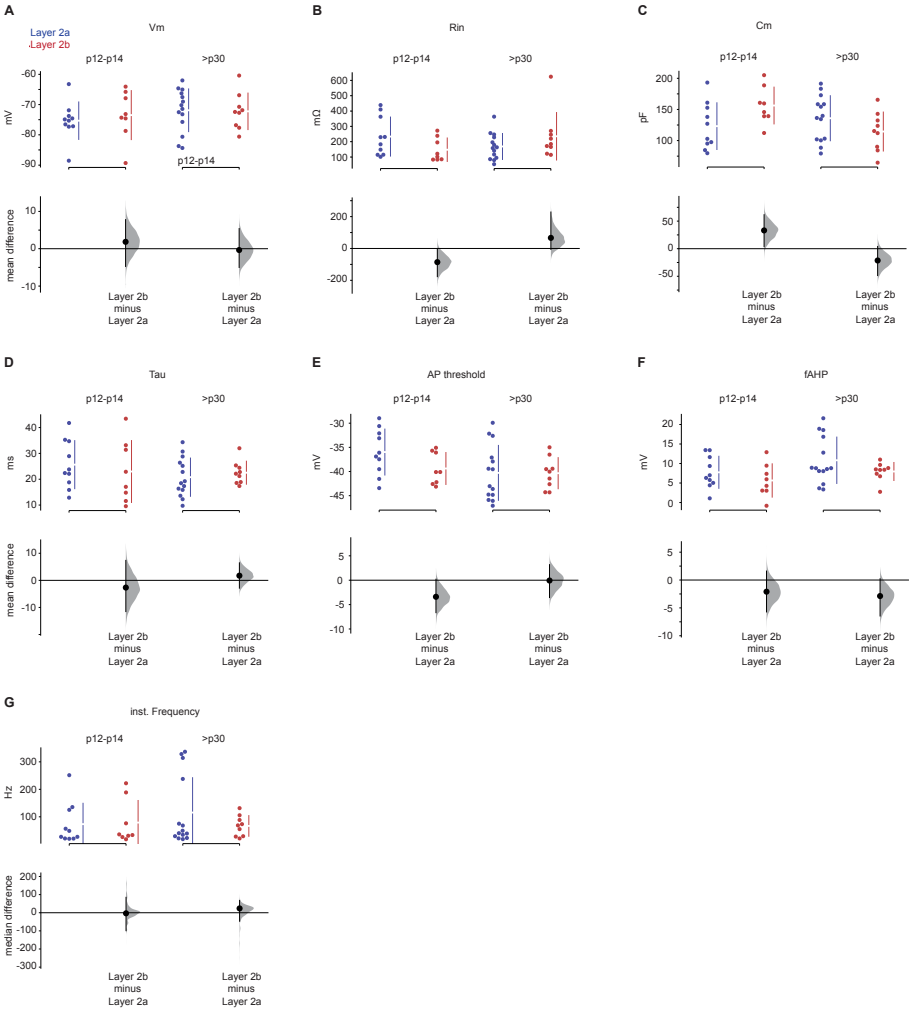

A to F: The mean differences of intrinsic electrophysiological parameters of layer 2a (blue) and layer 2b (red) neurons at p12-14 (left) and at >p30 (right) are shown in Cumming estimation plots. The raw data is plotted on the upper axes; each mean difference is plotted on the lower axes as a bootstrap sampling distribution. Mean differences are depicted as dots and the 95% confidence intervals are indicated by the ends of the vertical error bars. (A) refers to resting membrane potential Vm, (B) to the input resistance Rin, (C) to the membrane capacitance Cm, (D) to the membrane time constant tau, (E) to the AP threshold and (F) to the fast afterhyperpolarizing potential fAHP. (G) The median differences of the instantaneous firing frequency of layer 2a (blue) and layer 2b (red) neurons at p12-14 (left) and at >p30 (right) are shown in Cumming estimation plots. The raw data is plotted on the upper axes; each median difference is plotted on the lower axes as a bootstrap sampling distribution. Median differences are depicted as dots and the 95% confidence intervals are indicated by the ends of the vertical error bars.

Extended Data Table 1-2

Statistical analysis of the intrinsic electrical properties and morphological parameters of layer 2a and layer 2b neurons at p12-14 and > p30.

Data	Normal distribution	Type of Test	Post hoc Test	Comparison	P-value	Significant
Table 1: Vm	Yes	ANOVA	Holm-Sidak	2A 12-14 vs. 2B 12-14	0.9228	ns
				2A 30 vs. 2B 30	0.9228	ns
				2A 12-14 vs. 2A 30	0.6544	ns
				2B 12-14 vs. 2B 30	0.9228	ns
Table 1: Rin	Yes	ANOVA	Holm-Sidak	2A 12-14 vs. 2B 12-14	0.3939	ns
				2A 30 vs. 2B 30	0.3939	ns
				2A 12-14 vs. 2A 30	0.3939	ns
				2B 12-14 vs. 2B 30	0.3939	ns
Table 1: Tau	Yes	ANOVA	Holm-Sidak	2A 12-14 vs. 2B 12-14	0.8834	ns
				2A 30 vs. 2B 30	0.8834	ns
				2A 12-14 vs. 2A 30	0.5356	ns
				2B 12-14 vs. 2B 30	0.9123	ns
Table 1: Cm	Yes	ANOVA	Holm-Sidak	2A 12-14 vs. 2B 12-14	0.14	ns
				2A 30 vs. 2B 30	0.2833	ns
				2A 12-14 vs. 2A 30	0.3765	ns
				2B 12-14 vs. 2B 30	0.0654	ns
Table 1: Threshold	Yes	ANOVA	Holm-Sidak	2A 12-14 vs. 2B 12-14	0.3356	ns
				2A 30 vs. 2B 30	0.9743	ns
				2A 12-14 vs. 2A 30	0.113	ns
				2B 12-14 vs. 2B 30	0.8885	ns
Table 1: FAHP	Yes	ANOVA	Holm-Sidak	2A 12-14 vs. 2B 12-14	0.5225	ns
				2A 30 vs. 2B 30	0.3886	ns
				2A 12-14 vs. 2A 30	0.3813	ns
				2B 12-14 vs. 2B 30	0.5225	ns
Table 1: Instan Firing Freq	No	Kruskal-Wallis	Dunn	2A 12-14 vs. 2B 12-14	> 0.9999	ns
				2A 30 vs. 2B 30	> 0.9999	ns
				2A 12-14 vs. 2A 30	> 0.9999	ns
				2B 12-14 vs. 2B 30	> 0.9999	ns
Figure 2A2: Apical N branches	Yes	ANOVA	Holm-Sidak	2A 1-2 vs. 2A 6-8	0.3652	ns
				2A 6-8 vs. 2A 12-14	0.9212	ns
				2A 12-14 vs. 2A 30	0.8258	ns
				2B 1-2 vs. 2B 6-8	0.0004	***
				2B 6-8 vs. 2B 12-14	0.6565	ns
				2B 12-14 vs. 2B 30	0.0401	*
				2A 1-2 vs. 2B 1-2	0.4625	ns
				2A 6-8 vs. 2B 6-8	0.4625	ns
				2A 12-14 vs. 2B 12-14	0.4625	ns
				2A 30 vs. 2B 30	0.1986	ns
Figure 2A3: Apical dendritic length	Yes	ANOVA	Holm-Sidak	2A 1-2 vs. 2A 6-8	0.4547	ns
				2A 6-8 vs. 2A 12-14	0.0237	*
				2A 12-14 vs. 2A 30	0.0151	*
				2B 1-2 vs. 2B 6-8	0.0215	*
				2B 6-8 vs. 2B 12-14	0.0078	**
				2B 12-14 vs. 2B 30	0.3651	ns
				2A 1-2 vs. 2B 1-2	0.8141	ns
				2A 6-8 vs. 2B 6-8	0.4914	ns
				2A 12-14 vs. 2B 12-14	0.4914	ns
				2A 30 vs. 2B 30	0.0321	*
Figure 2A4: Apical N stems	Yes	ANOVA	Holm-Sidak	2A 1-2 vs. 2A 6-8	0.0063	**
				2A 6-8 vs. 2A 12-14	0.9102	ns
				2A 12-14 vs. 2A 30	0.0063	**
				2B 1-2 vs. 2B 6-8	0.4802	ns
				2B 6-8 vs. 2B 12-14	0.4802	ns
				2B 12-14 vs. 2B 30	0.5603	ns
				2A 1-2 vs. 2B 1-2	0.1932	ns
				2A 6-8 vs. 2B 6-8	0.0004	***
				2A 12-14 vs. 2B 12-14	< 0.0001	****
				2A 30 vs. 2B 30	0.0996	ns
Figure 2B: Avg Apical dendritic length	Yes	ANOVA	Holm-Sidak	2A 1-2 vs. 2A 6-8	0.3912	ns
				2A 6-8 vs. 2A 12-14	< 0.0001	****
				2A 12-14 vs. 2A 30	< 0.0001	****
				2B 1-2 vs. 2B 6-8	0.116	ns
				2B 6-8 vs. 2B 12-14	0.0004	***
				2B 12-14 vs. 2B 30	0.0229	*
				2A 1-2 vs. 2B 1-2	0.779	ns
				2A 6-8 vs. 2B 6-8	0.5553	ns
				2A 12-14 vs. 2B 12-14	0.779	ns
				2A 30 vs. 2B 30	0.5553	ns
Figure 3A2: Basal N branches	Yes	ANOVA	Holm-Sidak	2A 1-2 vs. 2A 6-8	0.3469	ns
				2A 6-8 vs. 2A 12-14	0.8511	ns
				2A 12-14 vs. 2A 30	0.588	ns
				2A 1-2 vs. 2A 30	0.0478	*
				2B 1-2 vs. 2B 6-8	0.0066	**
				2B 6-8 vs. 2B 12-14	0.0949	ns
				2B 12-14 vs. 2B 30	0.0299	*
				2A 1-2 vs. 2B 1-2	0.0587	ns
				2A 6-8 vs. 2B 6-8	0.0002	***
				2A 12-14 vs. 2B 12-14	< 0.0001	****
				2A 30 vs. 2B 30	0.0055	**
Figure 3A3: Basal dendritic length	Yes	ANOVA	Holm-Sidak	2A 1-2 vs. 2A 6-8	0.4705	ns
				2A 6-8 vs. 2A 12-14	0.2269	ns
				2A 12-14 vs. 2A 30	0.2269	ns
				2A 1-2 vs. 2A 30	0.0017	**

				2B 1-2 vs. 2B 6-8	0.0115	*
				2B 6-8 vs. 2B 12-14	0.0002	***
				2B 12-14 vs. 2B 30	0.0018	**
				2A 1-2 vs. 2B 1-2	0.2701	ns
				2A 6-8 vs. 2B 6-8	0.0017	**
				2A 12-14 vs. 2B 12-14	< 0.0001	****
				2A 30 vs. 2B 30	0.0151	*
Figure 3A4: Basal N stems	Yes	ANOVA	Holm-Sidak	2A 1-2 vs. 2A 6-8	0.9587	ns
				2A 6-8 vs. 2A 12-14	0.8718	ns
				2A 12-14 vs. 2A 30	0.9587	ns
				2B 1-2 vs. 2B 6-8	0.9613	ns
				2B 6-8 vs. 2B 12-14	0.0983	ns
				2B 12-14 vs. 2B 30	0.0037	**
				2A 1-2 vs. 2B 1-2	0.009	**
				2A 6-8 vs. 2B 6-8	0.0048	**
				2A 12-14 vs. 2B 12-14	< 0.0001	****
				2A 30 vs. 2B 30	0.1137	ns
Figure 3B: Avg Basal dendritic length	Yes	ANOVA	Holm-Sidak	2A 1-2 vs. 2A 6-8	0.7039	ns
				2A 6-8 vs. 2A 12-14	0.1208	ns
				2A 12-14 vs. 2A 30	0.2627	ns
				2A 1-2 vs. 2A 30	0.0034	**
				2B 1-2 vs. 2B 6-8	0.421	ns
				2B 6-8 vs. 2B 12-14	< 0.0001	****
				2B 12-14 vs. 2B 30	0.2488	ns
				2A 1-2 vs. 2B 1-2	0.9307	ns
				2A 6-8 vs. 2B 6-8	0.9307	ns
				2A 12-14 vs. 2B 12-14	0.3307	ns
				2A 30 vs. 2B 30	0.5864	ns
Figure 4D: Avg % coactive neurons	Yes	Unpaired t-test		1/3 L2 vs 3/3 L2	0.001801	**
Figure 5B1: Apical N branches in L1A	Yes	ANOVA	Holm-Sidak	2A 1-2 vs. 2A 6-8	0.0093	**
				2A 6-8 vs. 2A 12-14	0.2966	ns
				2A 12-14 vs. 2A 30	0.2116	ns
				2B 1-2 vs. 2B 6-8	< 0.0001	****
				2B 6-8 vs. 2B 12-14	0.6689	ns
				2B 12-14 vs. 2B 30	0.0218	*
				2A 1-2 vs. 2B 1-2	0.4472	ns
				2A 6-8 vs. 2B 6-8	0.4472	ns
				2A 12-14 vs. 2B 12-14	0.4472	ns
				2A 30 vs. 2B 30	0.0038	**
Figure 5B2: Apical N int branches in L1A	Yes	ANOVA	Holm-Sidak	2A 1-2 vs. 2A 6-8	0.0066	**
				2A 6-8 vs. 2A 12-14	0.0606	ns
				2A 12-14 vs. 2A 30	0.0606	ns
				2B 1-2 vs. 2B 6-8	< 0.0001	****
				2B 6-8 vs. 2B 12-14	0.2506	ns
				2B 12-14 vs. 2B 30	0.0337	*
				2A 1-2 vs. 2B 1-2	0.4658	ns
				2A 6-8 vs. 2B 6-8	0.4658	ns
				2A 12-14 vs. 2B 12-14	0.3362	ns
				2A 30 vs. 2B 30	0.0033	**
Figure 5B3: Apical N tips branches in L1A	Yes	ANOVA	Holm-Sidak	2A 1-2 vs. 2A 6-8	0.0258	*
				2A 6-8 vs. 2A 12-14	0.8365	ns
				2A 12-14 vs. 2A 30	0.522	ns
				2B 1-2 vs. 2B 6-8	< 0.0001	****
				2B 6-8 vs. 2B 12-14	0.9079	ns
				2B 12-14 vs. 2B 30	0.0222	*
				2A 1-2 vs. 2B 1-2	0.3281	ns
				2A 6-8 vs. 2B 6-8	0.4732	ns
				2A 12-14 vs. 2B 12-14	0.4732	ns
				2A 30 vs. 2B 30	0.0088	**
Figure 5C1: Apical dendritic length in L1A	Yes	ANOVA	Holm-Sidak	2A 1-2 vs. 2A 6-8	0.2541	ns
				2A 6-8 vs. 2A 12-14	0.084	ns
				2A 12-14 vs. 2A 30	0.0009	***
				2B 1-2 vs. 2B 6-8	0.0149	*
				2B 6-8 vs. 2B 12-14	0.0644	ns
				2B 12-14 vs. 2B 30	0.3158	ns
				2A 1-2 vs. 2B 1-2	0.7608	ns
				2A 6-8 vs. 2B 6-8	0.7295	ns
				2A 12-14 vs. 2B 12-14	0.7295	ns
				2A 30 vs. 2B 30	0.0002	***
Figure 5C1: Avg Apical dendritic length in L1A	Yes	ANOVA	Holm-Sidak	2A 1-2 vs. 2A 6-8	0.5613	ns
				2A 6-8 vs. 2A 12-14	< 0.0001	****
				2A 12-14 vs. 2A 30	0.0031	**
				2B 1-2 vs. 2B 6-8	0.1166	ns
				2B 6-8 vs. 2B 12-14	0.0351	*
				2B 12-14 vs. 2B 30	0.0002	***
				2A 1-2 vs. 2B 1-2	0.9215	ns
				2A 6-8 vs. 2B 6-8	0.8023	ns
				2A 12-14 vs. 2B 12-14	0.9215	ns
				2A 30 vs. 2B 30	0.0142	*
Figure 6C1: AUC ACSF vs. APV	Yes (but n=5)	Paired t-test		L2A ACSF vs L2A APV	0.294	ns
				L2B ACSF vs L2B APV	0.0126	*
		Wilcoxon		L2A ACSF vs L2A APV	0.686	ns
				L2B ACSF vs L2B APV	0.043	*
Figure 6C1: AUC L2A APV vs. L2B APV	Yes (but n=5)	Unpaired t-test		L2A APV vs L2B APV	0.924	ns

		Mann-Whitney			L2A APV vs L2B APV	1	ns
Figure 6C2: Amp ACSF vs. APV	Yes (but n=5)	Paired t-test			L2A ACSF vs L2A APV	0.891	ns
					L2B ACSF vs L2B APV	0.0117	*
		Wilcoxon			L2A ACSF vs L2A APV	0.893	ns
					L2B ACSF vs L2B APV	0.043	*
Figure 6C2: Amp L2A APV vs. L2B APV	Yes (but n=5)	Unpaired t-test			L2A APV vs L2B APV	0.248	ns
		Mann-Whitney			L2A APV vs L2B APV	0.296	ns
Figure 6D: ΔG/R ACSF vs. APV	Yes (but n=5)	Ratio paired t-test			L2A ACSF vs L2A APV	0.0187	*
					L2B ACSF vs L2B APV	0.0025	**
		Wilcoxon test			L2A ACSF vs L2A APV	0.043	*
					L2B ACSF vs L2B APV	0.043	*
Figure S2B: Apical N tips branches in L2	Yes	ANOVA	Holm-Sidak		2A 1-2 vs. 2A 6-8	0.5659	ns
					2A 6-8 vs. 2A 12-14	0.8522	ns
					2A 12-14 vs. 2A 30	0.8522	ns
					2B 1-2 vs. 2B 6-8	0.4691	ns
					2B 6-8 vs. 2B 12-14	0.9603	ns
					2B 12-14 vs. 2B 30	0.9603	ns
Figure S2C: Apical N tips branches in L1B	No	Kruskal-Wallis	Dunn	2	A 1-2 vs. 2A 6-8	0.0459	*
					2A 6-8 vs. 2A 12-14	0.2791	ns
					2A 12-14 vs. 2A 30	> 0.9999	ns
					2B 1-2 vs. 2B 6-8	> 0.9999	ns
					2B 6-8 vs. 2B 12-14	0.0078	**
					2B 12-14 vs. 2B 30	0.263	ns
					2A 1-2 vs. 2B 1-2	0.003	**
					2A 6-8 vs. 2B 6-8	> 0.9999	ns
					2A 12-14 vs. 2B 12-14	> 0.9999	ns
					2A 30 vs. 2B 30	0.1112	ns

Extended Data Figure 5-1

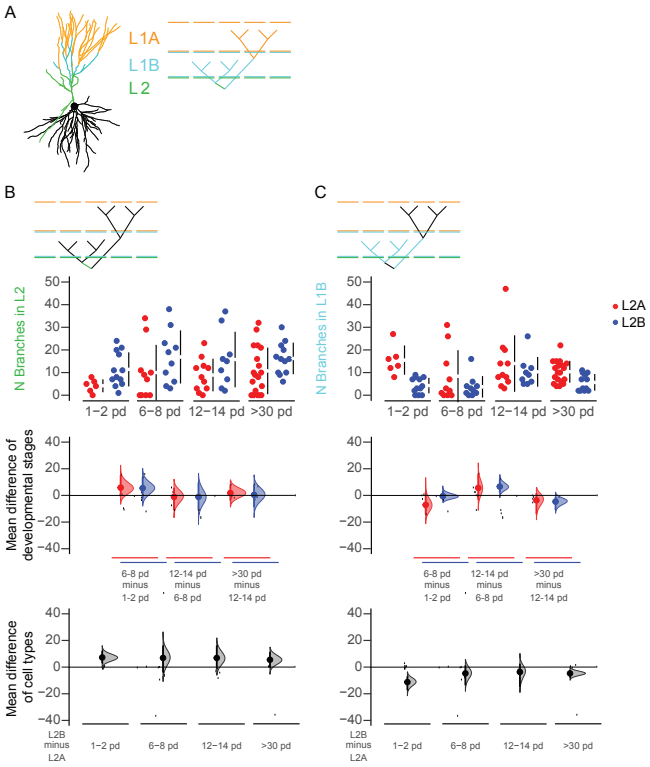

Layer specific terminating branches

(A) Example of a reconstructed cell shows the classification of the apical dendrites into three categories: branches terminating in layer 2 (L2, green), layer 1b (L1B cyan) and layer 1a (L1A, orange).

(B-C) The total number of branches terminating in layer 2 (B) and layer 1b (C) for layer 2a (L2A, red) and layer 2b (L2B, blue) neurons are shown in Cumming estimation plots. The raw data is plotted on the upper axes; mean differences between developmental stages are plotted on the middle axes and mean differences between the cell types are plotted on the lower axes, as a bootstrap sampling distribution. Mean differences are depicted as dots and the 95% confidence intervals are indicated by the ends of the vertical error bars.

14. Journal Summary List (ISi Web of KnowledgeSM): Publication 2

Journal Data Filtered By: **Selected JCR Year: 2016** Selected Editions: SCIE,SSCI
Selected Categories: **"NEUROSCIENCES"** Selected Category Scheme: WoS
Gesamtanzahl: 258 Journale

Rank	Full Journal Title	Total Cites	Journal Impact Factor	Eigenfactor Score
1	NATURE REVIEWS NEUROSCIENCE	36,952	28.880	0.071380
2	NATURE NEUROSCIENCE	54,399	17.839	0.160740
3	Annual Review of Neuroscience	13,211	15.630	0.020660
4	TRENDS IN COGNITIVE SCIENCES	23,273	15.402	0.046360
5	BEHAVIORAL AND BRAIN SCIENCES	8,195	14.200	0.010940
6	NEURON	82,253	14.024	0.227070
7	PROGRESS IN NEUROBIOLOGY	12,163	13.217	0.018020
8	MOLECULAR PSYCHIATRY	17,452	13.204	0.049670
9	ACTA NEUROPATHOLOGICA	16,462	12.213	0.037060
10	BIOLOGICAL PSYCHIATRY	41,859	11.412	0.067400
11	TRENDS IN NEUROSCIENCES	19,178	11.124	0.029690
12	JOURNAL OF PINEAL RESEARCH	7,278	10.391	0.008040
13	BRAIN	48,061	10.292	0.077590
14	ANNALS OF NEUROLOGY	34,215	9.890	0.057310
15	FRONTIERS IN NEUROENDOCRINOLOGY	3,516	9.425	0.006600
16	SLEEP MEDICINE REVIEWS	4,980	8.958	0.009730
17	NEUROSCIENCE AND BIOBEHAVIORAL REVIEWS	20,452	8.299	0.047230
18	NEUROSCIENTIST	4,325	7.391	0.009890
19	Molecular Neurodegeneration	2,946	6.780	0.009540
20	CEREBRAL CORTEX	27,496	6.559	0.063240
21	NEUROPSYCHOPHARMACOLOGY	23,920	6.403	0.046670
22	NEUROPSYCHOLOGY REVIEW	2,478	6.352	0.004650
23	GLIA	12,781	6.200	0.021920
24	Alzheimers Research & Therapy	1,699	6.196	0.007180
25	MOLECULAR NEUROBIOLOGY	7,338	6.190	0.017440
26	NEUROSIGNALS	653	6.143	0.000670
27	CURRENT OPINION IN NEUROBIOLOGY	13,188	6.133	0.036730
28	Brain Stimulation	3,905	6.078	0.013020
29	JOURNAL OF NEUROSCIENCE	171,800	5.988	0.319910
30	BRAIN BEHAVIOR AND IMMUNITY	10,719	5.964	0.026460
31	NEUROIMAGE	85,630	5.835	0.173210
32	PAIN	35,333	5.445	0.044460
33	NEUROPATHOLOGY AND APPLIED NEUROBIOLOGY	3,413	5.347	0.006400
34	NEURAL NETWORKS	8,741	5.287	0.010250
35	BRAIN PATHOLOGY	4,580	5.272	0.008450
36	JOURNAL OF NEUROTRAUMA	12,787	5.190	0.021640
37	Neurotherapeutics	3,451	5.166	0.008220
38	JOURNAL OF PSYCHIATRY & NEUROSCIENCE	2,759	5.165	0.004970
39	NEUROBIOLOGY OF AGING	20,010	5.117	0.046250

Rank	Full Journal Title	Total Cites	Journal Impact Factor	Eigenfactor Score
40	Journal of Neuroinflammation	7,946	5.102	0.023970
41	JOURNAL OF CEREBRAL BLOOD FLOW AND METABOLISM	16,998	5.081	0.029520
42	Frontiers in Molecular Neuroscience	1,979	5.076	0.008520
43	NEUROBIOLOGY OF DISEASE	14,554	5.020	0.031140
44	NEUROPHARMACOLOGY	18,559	5.012	0.040280
45	SLEEP	18,127	4.923	0.026090
46	Multiple Sclerosis Journal	9,727	4.840	0.023240
47	Molecular Autism	1,294	4.833	0.006320
48	PSYCHONEUROENDOCRINOLOGY	14,409	4.788	0.028830
49	Neuropsychiatry	149	4.778	0.000740
50	JOURNAL OF PHYSIOLOGY-LONDON	48,567	4.739	0.047830
51	INTERNATIONAL JOURNAL OF NEUROPSYCHOPHARMACOLOGY	6,082	4.712	0.015310
52	EXPERIMENTAL NEUROLOGY	19,445	4.706	0.027440
53	CURRENT OPINION IN NEUROLOGY	5,258	4.699	0.011490
54	Brain Structure & Function	4,325	4.698	0.014300
55	Frontiers in Cellular Neuroscience	6,088	4.555	0.027500
56	BIPOLAR DISORDERS	5,323	4.531	0.009660
57	HUMAN BRAIN MAPPING	18,139	4.530	0.041900
58	JOURNAL OF PAIN	8,312	4.519	0.018540
59	Frontiers in Aging Neuroscience	3,477	4.504	0.013020
60	Developmental Cognitive Neuroscience	1,483	4.321	0.007490
61	CORTEX	8,200	4.279	0.021370
62	EUROPEAN NEUROPSYCHOPHARMACOLOGY	6,575	4.239	0.015920
63	PROGRESS IN NEURO-PSYCHOPHARMACOLOGY & BIOLOGICAL PSYCHIATRY	9,740	4.187	0.016310
64	JOURNAL OF PSYCHOPHARMACOLOGY	5,518	4.179	0.012020
65	JOURNAL OF NEUROCHEMISTRY	35,279	4.083	0.030170
66	EUROPEAN JOURNAL OF NEUROLOGY	9,137	3.988	0.018850
67	Dialogues in Clinical Neuroscience	2,348	3.976	0.005480
68	HIPPOCAMPUS	8,694	3.945	0.016170
69	Social Cognitive and Affective Neuroscience	5,263	3.937	0.020160
70	CNS Neuroscience & Therapeutics	2,615	3.919	0.007370
71	Annals of Clinical and Translational Neurology	902	3.901	0.004880
72	ACS Chemical Neuroscience	3,084	3.883	0.011020
73	Frontiers in Neuroinformatics	1,377	3.870	0.006310
74	CLINICAL NEUROPHYSIOLOGY	17,871	3.866	0.021920
75	NUTRITIONAL NEUROSCIENCE	1,192	3.765	0.001900
76	GENES BRAIN AND BEHAVIOR	3,385	3.743	0.006820
77	JOURNAL OF ALZHEIMERS DISEASE	14,542	3.731	0.036370

15. Publication 2: SamuROI, a Python-Based Software Tool for Visualization and Analysis of Dynamic Time Series Imaging at Multiple Spatial Scales

frontiers in Neuroinformatics

METHODS
published: 29 June 2017
doi: 10.3389/fninf.2017.00044

SamuROI, a Python-Based Software Tool for Visualization and Analysis of Dynamic Time Series Imaging at Multiple Spatial Scales

*Martin Rueckl[1†], Stephen C. Lenzi[1,2†], Laura Moreno-Velasquez[2,3], Daniel Parthier[2], Dietmar Schmitz[2,4,5,6,7], Sten Ruediger[1] and Friedrich W. Johenning[2,3,4]**

[1] Institute of Physics, Humboldt Universität Berlin, Berlin, Germany, [2] Neuroscience Research Center, Charité Universitätsmedizin Berlin, Berlin, Germany, [3] Berlin Institute of Health (BIH), Berlin, Germany, [4] Einstein Center for Neuroscience, Berlin, Germany, [5] Bernstein Center for Computational Neuroscience, Berlin, Germany, [6] Cluster of Excellence 'Neurocure', Berlin, Germany, [7] DZNE-German Center for Neurodegenerative Disease, Berlin, Germany

The measurement of activity *in vivo* and *in vitro* has shifted from electrical to optical methods. While the indicators for imaging activity have improved significantly over the last decade, tools for analysing optical data have not kept pace. Most available analysis tools are limited in their flexibility and applicability to datasets obtained at different spatial scales. Here, we present SamuROI (Structured analysis of multiple user-defined ROIs), an open source Python-based analysis environment for imaging data. SamuROI simplifies exploratory analysis and visualization of image series of fluorescence changes in complex structures over time and is readily applicable at different spatial scales. In this paper, we show the utility of SamuROI in Ca^{2+}-imaging based applications at three spatial scales: the micro-scale (i.e., sub-cellular compartments including cell bodies, dendrites and spines); the meso-scale, (i.e., whole cell and population imaging with single-cell resolution); and the macro-scale (i.e., imaging of changes in bulk fluorescence in large brain areas, without cellular resolution). The software described here provides a graphical user interface for intuitive data exploration and region of interest (ROI) management that can be used interactively within Jupyter Notebook: a publicly available interactive Python platform that allows simple integration of our software with existing tools for automated ROI generation and post-processing, as well as custom analysis pipelines. SamuROI software, source code and installation instructions are publicly available on GitHub and documentation is available online. SamuROI reduces the energy barrier for manual exploration and semi-automated analysis of spatially complex Ca^{2+} imaging datasets, particularly when these have been acquired at different spatial scales.

Keywords: calcium imaging, analysis software, Python programming, Open Source Software, microscopy, fluorescence

OPEN ACCESS

Edited by:
Andrew P. Davison, Centre National de la Recherche Scientifique (CNRS), France

Reviewed by:
Michael Denker, Forschungszentrum Jülich, Germany
Malinda Lalitha Suvimal Tantirigama, University of Otago, New Zealand

****Correspondence:***
Friedrich W. Johenning
friedrich.johenning@charite.de

[†]These authors have contributed equally to this work.

Received: *07 April 2017*
Accepted: *13 June 2017*
Published: *29 June 2017*

Citation:
Rueckl M, Lenzi SC, Moreno-Velasquez L, Parthier D, Schmitz D, Ruediger S and Johenning FW (2017) SamuROI, a Python-Based Software Tool for Visualization and Analysis of Dynamic Time Series Imaging at Multiple Spatial Scales. Front. Neuroinform. 11:44. doi: 10.3389/fninf.2017.00044

INTRODUCTION

Monitoring fluorescence changes of indicator molecules over time is one of the primary tools by which neuroscientists try to understand the function of neurons and neuronal networks. Small molecule indicators including Ca^{2+} and direct voltage sensors can be used to read out the spatiotemporal code of neuronal activity in a non-invasive way (Scanziani and Häusser, 2009)

and are now routinely used in the study of brain activity at different spatial scales (Grienberger and Konnerth, 2012). As technological improvements allow imaging datasets to increase in their complexity (larger fields of view, longer permissible recording times, better temporal resolution, parallel use of different indicators at different wavelength), there is a growing need for tools that enable efficient data exploration. Furthermore, these tools must be applicable to datasets acquired at different spatial scales, because scientific questions increasingly require an understanding of processes at many scales sequentially or, if technically feasible, simultaneously.

Here, we would like to distinguish three spatial scales based on the existing terminology and the physical boundaries in conventional fluorescence microscopy with respect to resolution and field of view size: the subcellular or micro-scale, which includes subcellular structures like dendrites and spines (Jia et al., 2010; Kleindienst et al., 2011; Takahashi et al., 2012); the meso-scale, which comprises populations of individual cell bodies (Garaschuk et al., 2000; Stettler and Axel, 2009; Sofroniew et al., 2016); and the macro-scale, which is imaging of activity over several brain regions without cellular resolution (Conhaim et al., 2010; Busche et al., 2015). Datasets from each of these scales pose a different analytical challenge when extracting meaningful information about neuronal activity patterns from spatially defined regions of interest (ROIs).

In the last decade, we have seen major technical advances of genetically encoded Ca^{2+} indicators (GECIs) and the refinement of the multi cell bolus loading technique for *in vivo* Ca^{2+} imaging (Stosiek et al., 2003). These technical developments have led to a surge of Ca^{2+} imaging data at the meso-scale. Manual analysis of these datasets is labor intensive and can be prone to bias. This has driven the development of a wide variety of excellent tools that permit automated event detection and structure recognition for defining ROIs at the meso-scale (Junek et al., 2009; Mukamel et al., 2009; Tomek et al., 2013; Kaifosh, 2014; Hjorth et al., 2015; Pnevmatikakis et al., 2016).

While being tailor-made for meso-scale population Ca^{2+} imaging, these tools do not cover the requirements of other spatial scales. Batch processing and automation have enabled time-effective data analysis for large populations of cells, but similar advances have not been made in terms of data exploration and visualization of spatiotemporal structure. Both quality control (Harris et al., 2016) and manual identification of patterns in imaging data require intuitive and effective visualization. As far as we are aware, few analytical tools exist that provide users with an analysis environment that can be applied at different spatial scales. We hope that a user's proficiency in handling data with SamuROI in a Python-based environment at one scale will greatly facilitate data analysis at other scales. This way, users should be able to reduce time and resources necessary to acquaint themselves with different analysis packages.

Furthermore, technological advances in microscopy have enabled longer observation periods in larger fields of view (Sofroniew et al., 2016), which together permit acquisition of spatiotemporally complex datasets. For example, it will soon be possible to routinely image thousands of cells at once (Harris et al., 2016). In this context, it becomes possible to address questions about spontaneous patterns of activity across multiple brain regions at different scales. The informational structure in spontaneous datasets is less predictable or manageable, and exploratory analysis is an essential step in making sense of the data. Data browsing tools are limited in this domain, and there is a need for tools that allow scientists to efficiently identify spatiotemporal structure within their data. We developed SamuROI to fill this niche: to provide a tool that enables analysis at multiple scales, and convenient data visualization for datasets with complex spatiotemporal structure.

SamuROI was designed for use on a standard desktop PC or laptop and focuses on intuitive data exploration and effective semi-automated ROI management. The built-in graphical user interface (GUI) displays data in the space, time and amplitude domains in a way that allows the user to easily connect fluorescence changes with their morphological location of origin and vice versa. This makes data inspection and manual curating of automated ROI generation easier and facilitates the rapid identification of data patterns during exploratory analysis. SamuROI has been designed to work alongside other software, and to link analytical tools developed for the micro-, meso-, and macro-scales. ROIs generated from other tools can be imported, and also modified manually. Datasets can be saved as hdf5 files in which both structural and dynamic information can be organized together. Hdf5 is also a suitable format for automated post-processing of the analyzed data using Python or other scripting languages. We take advantage of the interactive workflow provided by Jupyter Notebook, which allows seamless integration of the SamuROI GUI with custom pre- and post-processing analysis pipelines. This way, SamuROI bridges the gap between batch processing and data inspection while providing a versatile analysis environment for application in a range of imaging applications at different scales. SamuROI source code is publicly available on GitHub[1] and licensed under the MIT license. Detailed installation instructions and usage documentation are also available online[2]. In this paper, we describe the software architecture and the general data processing workflow. We also provide examples of its application at the micro-, meso-, and macro-scale using Ca^{2+} imaging data obtained in acute slices.

MATERIALS AND METHODS

Experimental Procedures

Experimental data used to demonstrate and evaluate the functionality of SamuROI was generated in accordance with the national and international guidelines. All procedures were approved by the local health authority and the local ethics committee (Landesamt für Gesundheit und Soziales, Berlin; animal license number T100/03).

Dendritic and spine calcium signals were obtained in layer 2 cells of the medial entorhinal cortex (MEC) in acute brain slices. Slices were prepared from juvenile Wistar rats (postnatal day 16 to 25) following the procedures as described in Beed et al. (2010).

[1]https://github.com/samuroi/SamuROI

[2]https://samuroi.readthedocs.io

To provide optimal imaging conditions for small subcellular structures, we filled single cells with synthetic dyes. For dye filling, we either performed whole-cell patch clamp recordings or single cell electroporation for measurements where we did not want to interfere with the intracellular composition of the cell. The intracellular solution for filling patch clamp pipettes (3–6 MΩ) contained: 130 K-gluconate, 20 KCl, 10 HEPES, 4 MgATP, 0.3 NaGTP, and 10 phosphocreatine (in mM; pH: 7.3) and 30 μM Alexa 594 and 100 μM Oregon-Green BAPTA-6F (OGB6F). Electroporation pipettes were filled with 1 mM Oregon-Green BAPTA-1 (OGB1) and 150 μM Alexa 594 dissolved in ddH2O. The single 10 V electroporation pulse lasted 10 ms (Lang et al., 2006; Nevian and Helmchen, 2007).

For population Ca^{2+} imaging of neonatal spontaneous synchronous network events, we used the genetically encoded Ca^{2+} indicator (GECI) GCaMP6f. NEX-Cre mice (Goebbels et al., 2006) were crossed with Ai95 animals[3] (Madisen et al., 2015) for constitutive GCaMP6f expression in excitatory cells only. Neonatal slices were cut horizontally for piriform cortex and sagittally for the parahippocampal formation at p0-10. We used the same ringer at all stages of preparation and recording. This solution consists of 125 mM NaCl, 25 $NaHCO_3$, 10 mM glucose, 4 mM KCl, 1.25 mM NaH_2PO^4, 2 mM $CaCl_2$ and 1 mM $MgCl_2$, bubbled with carbogen (5% CO2 and 95% O2).

For all experiments, Ca^{2+} imaging was performed using a Yokogawa CSU-22 spinning disk microscope at 5000 rpm. The spinning disk confocal permitted the generation of a large field of view time series at a high acquisition rate. A 488 nm LASER was focused onto the field of view using a 4×, 40×, or 60× objective. Emission light was filtered using a 515 ± 15 nm band-pass filter. Fluorescence was detected using an Andor Ixon DU-897D back-illuminated CCD, with a pixel size of 16 μm. Andor iQ software was used for data acquisition. In order to prevent photo bleaching while producing the clearest images possible, we minimized the illumination power.

Software Architecture

Requirements for Running SamuROI

In order to provide maximum backward compatibility, SamuROI is completely developed and tested using Python version 2.7. It should be possible to use SamuROI with Python versions 3.x but we have not tested this specifically. The efficient and effective use of SamuROI depends on four freely available python libraries:

- Numpy and scipy are libraries for dealing with numerical data in Python. They provide numerical routines for array manipulation and are capable of handling large datasets.
- PyQt, the bindings for the C++ widget library Qt is used for putting together windows, widgets, and other GUI elements.
- Matplotlib, a plotting library which allows plots to be embedded in PyQt widgets.

All four modules are widely used, under active development and have been rigorously tested and validated by the open source community. Throughout the development of SamuROI, we tried to build on top of the most recent versions of those projects. The source code of SamuROI is publicly available on GitHub[4] (see README.md for installation instructions). SamuROI is licensed under the MIT license. The documentation of SamuROI is automatically built via Sphinx and available online[5]. Unit tests and a continuous integration pipeline of new releases are currently not available. Contributions in the form of bug reports, pull requests and proposed improvements are highly appreciated.

Basic Software Design of SamuROI

When designing SamuROI, a key objective was to provide easy extensions for custom functionality such as data pre- and post-processing, visualization and data curation. For this, toggling between the GUI and python code is central. We therefore encourage running SamuROI from a Jupyter Notebook, which provides easy access to all aspects of data management.

We did not want the user to have to keep modifications via the GUI and the Jupyter Notebook in sync. For coordinating the different levels of interaction with the data via widgets in the GUI and the Jupyter Notebook, we implemented a strict separation of data and its presentation. Technically speaking, we used the "document-view" also known as "model view (controller)" design pattern (Gamma et al., 2015). In document view, data (Document in **Figure 1A**, i.e., the SamuROIData class), and its presentation to the user (Views in **Figure 1A**, i.e., the GUI and its widgets) do not depend on one another. For communication between these parts we use a signal slot pattern (as in Qt, sometimes also called "Observer pattern") (Gamma et al., 2015) (**Figure 1A**). As data is mutated, the data object calls all slots of the respective signal, i.e., it informs all 'listeners' that some aspect of the data has changed.

The right hand side of **Figure 1A** represents a set of different views. All views 'listen' to signals of the data that are of relevance for their visualized content upon application start up, which means they are slots of the signal. If the data changes, signals will be emitted to all slots and, consequently, all listening views will be notified and will modify their presentation to the user accordingly.

The SamuROIData class on the left hand side of **Figure 1A** holds all relevant data and provides functionality for mutating and extracting subsets of data (**Figure 1A**, left). The most important data members of this class are:

- the 3D numpy array containing the video data
- the 2D numpy array containing the overlay mask
- multiple python containers holding user defined ROI objects

The extensive use of python properties within the SamuROIData class allows mutations of the data to be intercepted and the respective signals to be triggered. For the full API of the SamuROIData class and the mask sets, the reader is referred to the online documentation, especially the examples section. The signals provided by the SamuROIData class are trivially implemented as lists of python functions where the arguments of the signal invocation get perfectly forwarded to

[3]https://www.jax.org/strain/024105

[4]https://github.com/samuroi/SamuROI

[5]https://samuroi.readthedocs.io

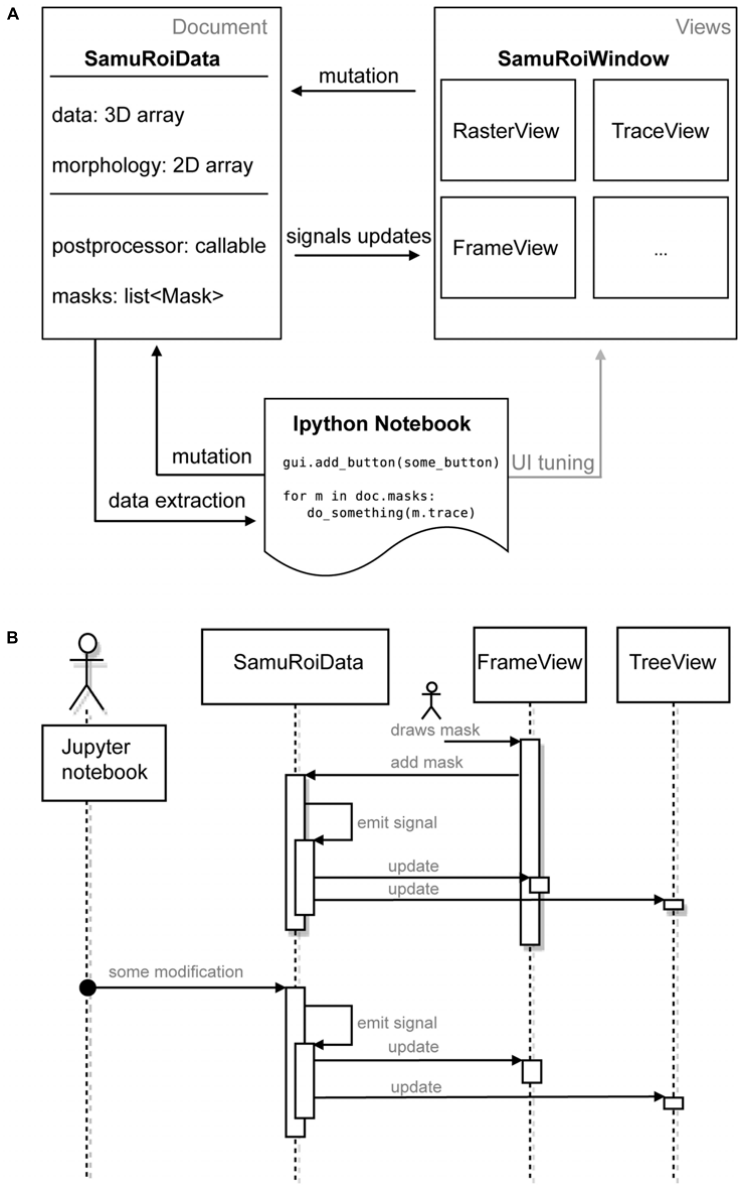

FIGURE 1 | Software Architecture. **(A)** Diagram depicting the components of SamuROI in the document view pattern. SamuROI is split up into a data or document class (SamuRoiData) and multiple widgets which display the data (views). Communication between those classes takes place via callbacks (termed mutation, signals updates and data extraction in the diagram). This allows the user to update both, document and view by an interactive shell (here Ipython, bottom) without having to worry about keeping document and view in sync. **(B)** Flowchart to illustrate the process of signaling between widgets, data and interactive shell. User interactions are symbolized with the stickman.

all functions contained in the list:

```
class Signal(list):
    def __call__(self,*args,**kwargs):
        for func in self:
            func(*args,**kwargs)
# usage example
def do_something(message):
    print message
sig = Signal()
sig.append(do_something)
sig("hello world")
```

The above class is not to be mistaken with the Qt signals that are used to connect to events originating from user input. The rationale behind using two different signal types is simple: the SamuROIData class was designed such that it is independent of any user frontend, and hence must not have a dependency on Qt.

This document view based design pattern permits the desired synchronized cooperation between the GUI and the Jupyter Notebook: as can be seen in **Figure 1A**, the Jupyter Notebook permits tuning of the GUI as well as data mutation and extraction via the SamuROIData class at the document level. Further, if user interaction with the GUI updates the SamuROIData class the same signal cascade as described above will be triggered.

To give an example of signal slot communication, we would like to describe in detail what happens during ROI mask addition. When a user adds a ROI mask to the data using the GUI widget, the widget's Qt signal is triggered, which adds the ROI mask to the SamuROIData class, triggers its internal signal and notifies all interested listeners (for example the widget which displays the list of masks as a tree structure; upper part of **Figure 1B**). The widget, which adds the ROI mask, therefore, does not need to know about other components which also require notification: the logic is confined in the signals from the SamuRoiData object.

Because of this signaling structure, updates originating from the interactive shell will invoke the same mechanism and update relevant GUI elements (lower part of **Figure 1B**). On the other hand, one can also use the interactive shell to add custom GUI elements to an existing window, or connect post-processing and export functions to the data (see example in the online documentation). Another advantage of the separation between data and view is the future possibility to reuse the GUI code, e.g., in a cloud computing scenario. Then the data object behind the client GUI would simply defer all calculations and memory limitations to a server and present only 2D slices and the calculated traces of the data to the GUI.

Performance Considerations

For a smooth user experience and fast calculation of traces from the defined ROIs SamuROI always holds the full 3D video array in memory. With the use of double precision floating points and an assumed video size of 512 × 512 pixels and 1000 frames this results in about 2 GB of required RAM. Hence, long-term recordings with high frame rates are likely to exceed an average workstations system memory. Since features as memory mapped files are not supported in SamuROI, such datasets need to be split to fit into memory.

Calculating the time series of ROIs makes extensive use of numpy routines and has negligible CPU cost: due to numpy's underlying C implementation a decent machine needs only a couple of milliseconds per ROI. Further, calculated traces get cached by SamuROI and hence need not be calculated twice. The only relevant computation times arise from the pre-processing of data (stabilization, filtering and/or renormalization) which can grow up to a couple of minutes per dataset. However, because pre-processing is usually run from an interactive python shell, it can easily be done in batch mode or distributed to dedicated machines. Then, the saved pre-processed data can be loaded into the GUI with minimal delay.

FUNCTIONALITY AND RESULTS

We will now illustrate the functionality of SamuROI by describing the general workflow of data processing. After explaining data import and pre-processing, we describe the different widgets of the GUI and explain data export. We then provide three application cases at the micro-, meso- and macro-scale. We provide the most detailed description of micro-scale imaging, as we are not aware of any standardized freeware software solutions facilitating the analysis of fluorescence changes in complex dendritic structures.

General Workflow

The first step of any image analysis software is the conversion of the acquired raw data into a format compatible with the analysis software. Depending on the data acquisition system used, dynamic image series are saved in a variety of data formats. We therefore needed to define a format that works with SamuROI. As an interface with SamuROI, we chose multiple image tif files. When it becomes necessary to convert data from other time series formats into multiple image tif files, we recommend the use of Fiji (Schindelin et al., 2012).

The first step after loading the multiple image tif file into SamuROI is the conversion into a 3D numpy array. This is a convenient format that allows a whole range of computations to be applied to the data. Usually, a couple of pre-processing steps are applied to the raw fluorescence images. Pre-processing can be performed in Python on this numpy array. SamuROI comes with a set of standard pre-processing functions. These include image stabilization [via opencv (Bradski, 2000), stabilization consists of rigid and warpaffine transformations to align each image to a given reference frame of the video provided], background subtraction, bandstop filtering and transformation of the raw

fluorescence data into a ΔF/F dataset (see Supplementary Methods for details on the underlying algorithms). Usage of these functions requires the use of an interactive shell like Jupyter. With a basic working knowledge of Python, users can also implement their own custom pre-processing routines for the 3D numpy array.

Next, a SamuRoiData object is created from the pre-processed data. The SamuRoiData object can be visualized with its associated GUI. This data object can be accessed and manipulated from within this GUI or directly using python commands in the interactive shell or with stand-alone python scripts. The current version of the GUI can be used for ROI mask generation, smoothing, detrending, and thresholding.

We would now like to provide an overview of the current SamuROI GUI with all functional widgets. Our example data displays a dendritic segment with adjacent spines in a layer 2 cell of the MEC. The cell was in whole-cell patch clamp mode, the fluorescent Ca^{2+} signal corresponds to a doublet of backpropagating action potentials evoked by current injection.

The GUI is built using the PyQt library and consists of four interactive widgets and a toolbar (**Figures 2A–E**). The central ImageView panel (**Figure 2D**) displays a morphological grayscale image of the structure underlying the dynamic image series. A thresholding overlay mask defines the relevant pixels of the morphology image, which are above a user-defined threshold (see Supplementary Methods for details on the underlying algorithm). On top of the composite morphological grayscale and thresholding overlay mask image, a heatmap encodes the frame-specific fluorescence detected in each pixel. The threshold for the thresholding overlay mask can be set manually in the mask tab in the toolbar (**Figure 2A**) and a slider permits the user to explore the frame-specific fluorescence detected in each pixel frame by frame. After loading the dynamic image series into the GUI, the user can define specific ROI masks for further analysis of location-specific changes of fluorescence over time. The SamuROI toolbar supports creation of four types of ROI masks: branches, polygons, circles and pixel groups. Further, predefined segmentations [e.g., ROI masks exported from ilastik (Sommer et al., 2011) or swc files denoting dendritic structures from Neutube (Feng et al., 2015)] can be loaded via the interactive shell. The TreeView widget lists individually created or imported ROI masks (**Figure 2C**). While TreeView automatically generates names for individual ROI masks, the user can change names interactively. Selecting an item from the list in TreeView will display the corresponding trace of averaged intensity per frame in the TraceView widget (**Figure 2E**). Individual or all branch masks can be further subdivided into pixel-sized sub-segments using the 'split' tabs in the toolbar (**Figure 2A**). Individual sub-segments can be selected as children of individual branchmasks in the TreeView widget. The RasterView widget displays individual segments. The relative fluorescence of each segment is color coded and plotted against frame number (**Figure 2B**).

Within the GUI, SamuROI offers different post-processors like detrending and smoothing tabs or a pull-down menu item for event detection. Examples for how the interactive Jupyter shell can be used for additional post-processing of SamuRoiData objects are provided in the online documentation.

After defining and curating the ROIs and performing the necessary post-processing steps, the user needs to save the data. It is possible to document the analysis by saving the Jupyter Notebooks underlying individual experiments. In addition, we provide the option to export most of the relevant data stored in the SamuRoiData to hdf5 files. A pull-down menu in the GUI can be used directly to save the set of variables that is to be exported. At the moment this includes the threshold used to construct the thresholding overlay mask, ROI location and identity with the corresponding calcium imaging traces and the original 3D numpy dataset. User-specific post-processing results like those related to event detection can be incorporated into the hdf5 file, but this must be done outside of the GUI in Python. The hdf5 file is modeled on the structure of the SamuRoiData object, structured according to the masklist displayed in the TreeView widget. The analysis environment can be reconstructed from stored hdf5 files, which can be loaded into SamuROI as SamuRoiData objects. The hdf5 file structure allows the user to selectively import parts of a previous analysis environment, which makes it possible to easily reapply stored sets of ROI masks to a new dataset.

One key motivation for using the hdf5 file structure is that in large datasets, it often becomes necessary to identify individual events in different segments using automated procedures. Here, we define an event as form of electrical neuronal activity (an action potential or a synaptic response or a combination of both) that results in a temporary brightness change of the fluorescence indicator that can be clearly differentiated from baseline noise. Usually, events occur in different spatially confined segments of the data (e.g., different cell bodies at the meso-scale). Analyzed data, exported as hdf5 files, can be used for automated batch analysis in Python or other analysis environments. Batch processing of large datasets should best be performed on hdf5 files of individual experiments exported from SamuROI. However, for definition of the settings used for event detection and quality control, the SamuROI GUI is built to facilitate visualization of event detection. As a starting point, SamuROI offers standard, built-in event detection functionality based on template matching of a bi-exponential function. Briefly, this approach is based on defining a template of a typical event signal. This template then slides along the fluorescence trace and is scaled to fit the data at each point. This way, a point-by-point detection criterion is generated based on the optimal scaling factor and the quality of the fit. The user has to define the threshold above which the detection criterion defines an event (Clements and Bekkers, 1997). While originally developed for analysing electrophysiological data, this approach can also be applied in imaging applications (Tantirigama et al., 2017). Time constants, which define the fit parameters of representative 'bait' traces, must be obtained from other software solutions; we recommend the use of Stimfit (Schmidt-Hieber, 2014). Importing traces from hdf5 into Stimfit is relatively straightforward, which can then be used for curve fitting. Detected events are highlighted in the Treeview, Rasterview and TraceView widgets. Once the event detection settings (in our case time constants and detection criterion) have been optimized in the GUI, they can be performed in the Jupyter Notebook on larger datasets.

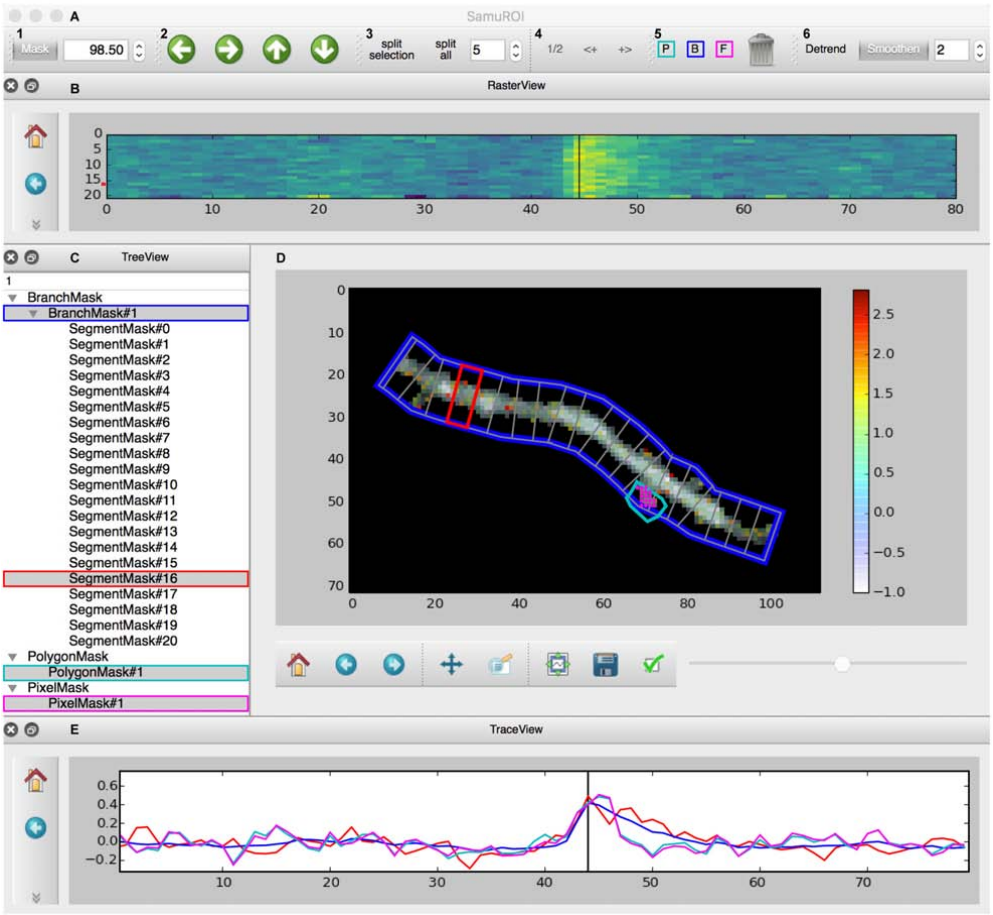

FIGURE 2 | Screenshot of the GUI. **(A)** Toolbar: (A1) Allows the user to set a numeric cut-off value for the thresholding overlay mask. The thresholding overlay mask defines irrelevant background fluorescence and spares relevant pixels in the morphology image. (A2) Permits pixel-wise shifting of selected ROI masks in the direction of the arrows. (A3) Defines the width of branch sub-segments arranged perpendicular to the all BranchMasks (split all) or only the selected BranchMask (split selection). (A4) Permits grouping adjacent segments or splitting the selected segments in half. In tab (A5), the different mask drawing tools for PixelMasks (P, turquoise), BranchMasks (B, blue) and freehand PolygonMasks (F, magenta) can be selected. Selected masks can be deleted using the trashcan icon in this tab. Tab (A6) hosts the Detrend and Smoothen postprocessors. The degree of smoothing (moving average filter) can be defined using the number tab. **(B)** The RasterView widget visualizes the temporal and spatial distribution of the fluorescent Ca^{2+} signal over the segments of a selected BranchMask. Points on the *y*-axis corresponds to the segment number, the *x*-axis defines the frame number. The amplitude of the averaged fluorescent signal of a given segment is color-coded. The vertical black line between frames 40 and 50 corresponds to the slider button and the currently selected frame in **(D)** and the line in the TraceView **(E)**. The panel on the left gives access to standard matplotlib functions like for example zooming, panning or exporting of subplots as image files. Similar panels can be found in the FrameView **(D)** and TraceView **(E)** widgets. **(C)** The TreeView widget gives access to the ROI mask list. Different types of masks are grouped and selected masks are highlighted in gray. Names of the different ROI masks are indexed by default, but can be changed directly in the TreeView widget. **(D)** The image in the FrameView widget is a composite of the grayscale image of the morphology object with the thresholding overlay mask and the color-coded pixel brightness of the currently selected frame. The x- and y-scale corresponds to single pixels. ROI masks are projected on this image in light gray, selected ROI masks are highlighted in colors corresponding to traces demonstrated in **(E)**. The corresponding color code in **(C)** and (A5) is just for illustration. The scale bar on the right illustrates the color code for frame-specific pixel brightness. **(E)** In the TraceView widget, the relative change in brightness (in our example, the $\Delta F/F$ value) of the selected ROI mask(s) is plotted against the frame number.

Application Cases

Subcellular Imaging

One intended use for SamuROI is the generation and visualization of temporal and spatial profiles of neuronal activity related Ca^{2+} signals from complex dendritic structures and spines (**Figure 3**). Specifically, this includes analysis of the spatial distribution of spontaneous synaptic events reflected by Ca^{2+} 'hotspots' on dendrites or spines. See Jia et al. (2010), Kleindienst et al. (2011) or Takahashi et al. (2012) for example research questions requiring this analysis approach. Another example is the identification and demarcation of spontaneous release from intracellular stores in dendrites. Related research questions can be found in Larkum et al. (2003), Miyazaki and Ross (2013) and Lee et al. (2016).

In our example, we would like to illustrate how SamuROI can be used to visually identify and localize a spontaneously occurring Ca^{2+} transient or 'hotspot' in a single spine on a long dendritic segment. Here, a layer 2 cell in the MEC has been electroporated with the Ca^{2+} indicator OGB1. A morphological image was generated as a maximum projection along time of the motion- corrected 3D dataset. Then, the motion-corrected 3D data set is transformed into $\Delta F/F$ data. SamuROI then transfers both, the morphology image and the $\Delta F/F$ 3D numpy array, into a SamuRoiData object. In the online supplements, we provide a Jupyter Notebook that includes a step-by-step description of data import, the pre-processing steps and the generation of the SamuRoiData object and the corresponding GUI.

Manual drawing of ROIs delineating subcellular structures like dendrites and spines requires the investigator to manually trace the boundary between the structure and the background, which is a time-consuming and tedious task. In SamuROI, we implemented a functionality that speeds this process up significantly. Based on the morphology image, SamuROI generates a 'thresholding overlay mask.' The software implements a thresholding algorithm (see Supplementary Methods) that defines above background pixels incorporated into the further analysis. Compare the raw morphological image **Figure 3A1** (top left) and the thresholded image **Figure 3A2** (top right). SamuROI ignores the masked out black pixels in ROIs, which only contain background fluorescence. ROI masks, irrespective of whether they are generated as tubes using the SamuROI branch tool or incorporated from somewhere else, can therefore be larger than the structure of interest. This speeds up manual ROI generation significantly and also facilitates the import of ROI masks from for example swc files, as ROI masks can include regions where no pixels are analyzed. Small inter-experimental changes in ROI shape are automatically incorporated, so that the same ROI can be used for consecutive sweeps of the same structure. Using of the same ROI mask for consecutive sweeps is further facilitated by an alignment tab (**Figure 2A2**) that permits shifting of selected ROIs. Together with the example Jupyter Notebook in the online supplements we also offer an example swc file from the freeware software Neutube together with an instruction how to generate swcs in Neutube that can be used by SamuROI and incorporated directly as branch ROIs.

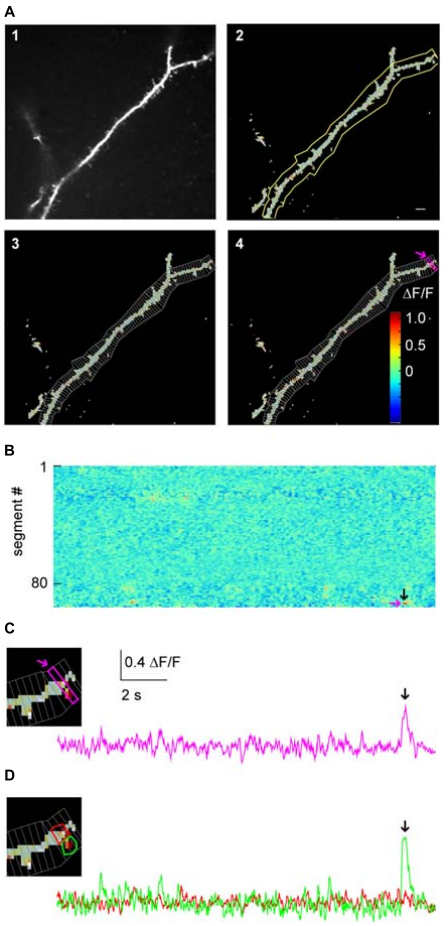

FIGURE 3 | Micro-scale imaging example for using SamuROI on a dendritic structure. **(A)** (A1) The morphological image of a dendritic segment from an electroporated layer 2 cell in the MEC. (A2) The corresponding FrameView image from SamuROI, a composite of the thresholding overlay mask defining relevant pixels of the grayscale morphological image and color-coded frame specific brightness values of the relevant pixels. The yellow outline was generated using the BranchMask tool. The scale bar corresponds to 2 μm. (A3) Depicts how the BranchMask from (A2) is divided into SegmentMasks by SamuROI. **(B)** RasterView of segments from the dendritic branch corresponding to **(A)**. Time on the *x*-axis is defined by the scale bar in **(C)**. $\Delta F/F$ is color-coded as in (A4). The magenta arrow corresponds to the point on the *y*-axis representing the magenta-colored segment both in (A4) and in **(C)**. The black arrow corresponds to the time point indicated by arrows in **(C)** and **(D)** and defines the frame depicted in (A4). **(C)** The inset on the left magnifies the distal part of the dendrite shown in **(A)**. The trace corresponds to the SegmentMask outlined in the inset and (A4). **(D)** Based on the distribution of pixel brightness at the time point defined by the black arrow in **(B)**, ROI masks are defined manually as freehand PolygonMasks. The local Ca^{2+} transient in the spine (green) can be differentiated from the dendritic segment (red).

The key objective of our application example is the detection of spontaneously occurring local hotspots of activity on a large dendritic structure. For this task, it is necessary to subdivide dendritic branches into segments and visualize fluorescence changes in each individual segment. Again, manual ROI drawing tools that are typically implemented in analysis software would now require the user to manually draw a large number of evenly spaced ROIs. For this task, it is necessary to subdivide dendritic branches into segments and visualize fluorescence changes in each individual segment. In SamuROI, the split tool (**Figure 2A3**) automatically divides tubular branchmasks into identically spaced sub-segments oriented perpendicular to the longitudinal axis of the dendritic branch (**Figures 3A3,4**). The spacing of these segments is a user-defined number of pixels. This adaptability is important, as signal to noise improves when the number of pixels in a segment corresponds to the number of pixels active in a hotspot. In each segment, the thresholding overlay mask defines pixels that will be averaged. Further, a pixel's surface fraction, which resides within the ROI mask, determines its weight. Pixels in the interior of the ROI will have a weight of 1, boundary pixels will have a weight of less than 1.

After SamuROI has calculated the average for all segments, it is necessary for the experimenter to identify and localize hotspots of activity. The usual output of ROI-Data are fluorescence traces. Visually screening large numbers of fluorescence traces derived from individual dendritic segments is tedious and prohibits immediate recognition of temporal and spatial patterns. Therefore, the RasterView widget (**Figure 3B**) provides a linescan-based color-coded display of the intensity time-course of each segment in a branch.

This approach enables the investigator to rapidly visualize the spatial and temporal activity pattern and identify a hotspot of activity in our example. In addition, once the putative hotspot has been identified in the RasterView widget, we want to know the exact position in on our morphological image in the frame view widget and visualize the underlying fluorescence trace to evaluate qualitative parameters of the signal which get lost in a heatmap. SamuROI offers a solution to this problem that imaging signals need to be displayed in different formats synchronously for evaluation. Our software permits intuitive browsing of the data by synchronizing different widgets in the GUI: in our example, clicking a temporally and spatially defined hotspot in the RasterView widget (arrows in **Figure 3B**) highlights the corresponding ROI mask in the FrameView widget (**Figure 3A4**) and the segment in TreeView. It also triggers the display of the corresponding sweep in TraceView (**Figure 3C**). We are now able to locate the signal at the distal tip of the dendritic segment and estimate the time course and the signal to noise ratio looking at the trace.

By definition, our segment masks are stereotyped and may not capture the perimeter of a hotspot or spine correctly. SamuROI enables the visualization of the exact spatial extent of the hotspot we detected in our example. By selecting the time points of interest in the RasterView widget at the event peak, the $\Delta F/F$ color-coded pixels are overlaid on the morphological image in FrameView (see inset in **Figure 3C**) and the corresponding frame is marked in the TraceView widget (**Figure 3C**, black arrow).

It is now necessary to define the hotspot in greater detail. For this purpose, we generated tools for ROI definition using freehand drawn polygons or individually selected pixel groups. In our example, the RasterView permits immediate identification of a hotspot and its localization in the FrameView widget. The intensity color-code in the FrameView widget demonstrates that the active pixels correspond to a dendritic spine (see the inset in **Figure 3C**). By drawing a freehand polygon around primarily active pixels in the FrameView widget, we manually generate a ROI mask that only incorporates the isolated hotspot (**Figure 3D**).

Using this example that illustrates the core functionality of SamuROI, we would now like to explain the options for further data processing offered by our hdf5 file based data format. From identification of a hotspot, one could save the adapted set of ROI masks (branch masks, segments and the newly generated polygon) and apply it to a different image series from the same structure. This way, it would be possible to identify and analyze all hotspots in a set of image series from the same structure. Additionally, one could use the detected signal as a 'bait' to generate a template for a typical signal and use this for automated event detection in this dataset. Once all image series are analyzed, the hdf5 files will not only contain all traces underlying labeled structures but also the spatial information related to these structures, which will be helpful when analysing spatial aspects of activity. One could for example analyze if hotspots tend to be spatially clustered or if they are distributed randomly.

Meso-scale Imaging

One of the goals of population imaging is to identify and describe structure in the activity of populations of cells. Specifically, single-cell Ca^{2+} signals representing action potential firing can be spatially and temporally related to each other during spontaneous network activity as for example in Namiki et al. (2013), or following extracellular synaptic stimulation as in Johenning and Holthoff (2007). *In vivo*, these cellular activity patterns are often related to behavior, one of many examples can be seen in Heys et al. (2014).

It is common in this kind of data exploration to have no hypothesis regarding where activity will be located or how it will be temporally structured within a population of cells. For this type of analysis the SamuROI GUI can be used for data visualization with generic ROI masks from a variety of software for interactive display of different groups of cells. In addition, the SamuROI GUI offers convenient functionality for manual curation of ROIs and for the testing of event detection parameters.

We would now like to give a specific example to highlight unique functionalities of SamuROI. In our example, we imaged immature spontaneous synchronized network events in a neonatal slice preparation of the olfactory cortex. In these network events, there is high synchrony between a subset of cells, which are hard to identify as single cells by established variance-based measurements relying on sparse firing (Hjorth et al., 2015; see discussion for details). Here, we present a workflow for measuring activity in densely packed cell populations that fire

synchronously. We also show how our workflow can be used to provide a read out of the number of cells that are silent for the total duration of the recording.

For Ca^{2+} indication, constitutive GCaMP6f expression in post-mitotic excitatory neurons is achieved in the AI95/NexCre mouse line. The first step is to generate sets of ring-shaped ROI masks for GCaMP expressing cells that are based on pixel classification segmentation using ilastik (Sommer et al., 2011) and watershed segmentation using the scikit-image module in Python (van der Walt et al., 2014). In GCaMP-based datasets, the main underlying morphological feature is the ring shape of GCaMP6f expression, with a fluorescent cytosolic rim and a dark central nucleus (**Figure 4A**), and we present a segmentation approach specified for this morphological pattern. The generated ROIs are illustrated in **Figure 4B**.

In the online supplements, we provide an example Jupyter Notebook for using these functions to generate single cell segmentation ROI masks and opening them in SamuROI. In the documentation we also outline how to generate ROI masks using ilastik. After automated ROI generation in ilastik, we implemented a manual correction step for adding and deleting single cells. The user input required is essentially a mouse click on the dark nuclear center of a ring shaped cell. The final outcome of our segmentation is a 2 dimensional array in which each cell is denoted by a different number (i.e., every pixel belonging to cell 1 is denoted by a 1 in the image). This array is then imported into the SamuROI GUI. SamuROI works with these segmentations and treats them just as though they were a set of individual ROIs.

Basic GUI functionality of meso-scale population ROI masks is similar to that described above for micro-scale data. The GUI displays the mean fluorescence of all pixels in each mask and displays this through RasterView and TraceView as can be seen in **Figures 4C,D**. RasterView reveals structured activity in cell populations and allows event selection that leads to highlighting of the cell of origin in both FrameView and TreeView, as well as plotting in TraceView. Additionally, single or multiple cells can be selected in FrameView for simultaneous viewing and comparison of activity in TraceView, which is shown in **Figure 4C**. This way, it is possible to intuitively visualize aspects like synchrony, number of cells participating and the order of neuronal activation during events. One can pick cells displaying different activity patterns in the RasterView (e.g., the blue cell showing a large number of small bursts and the green cell showing a small number of large bursts), directly visualize their location in FrameView and compare the underlying traces in TraceView. In addition, it is possible to add more ROIs using the GUI. An example how this could be used in an experiment to bridge subcellular micro- and meso-scale imaging would be simultaneous imaging of a meso-scale population and single dendritic branches of individual dye-filled cells. This example would require the addition of branch segments to the cell ROI masks, which can be easily accomplished in SamuROI.

The SamuROI GUI further permits standard post-processing and event detection functionality of population imaging data sets. Data export as hdf5 files currently needs user intervention from the Jupyter Notebook, as the standard pull down menu does not offer the export of cell-specific ROI masks. In our online Supplementary Material, we provide a short function that enables SamuROI to add cell-specific ROI masks to the hdf5 files.

Representative traces visualized in the GUI can be picked and exported to other software, such as Stimfit to generate curve templates that permit automated event detection. The GUI can then be used to test sensitivity and specificity of event detection parameters in individual experiments before batch processing the hdf5 files in Python directly. This can be done using the same functions that have been used in the GUI. Batch analyzed data will provide spatial and temporal information of detected events in the hdf5 files, which will enable the user to extract spatial and temporal correlations of network activity simultaneously.

Macro-scale Imaging

Low magnification imaging of brain-activity induced changes in Ca^{2+} indicator fluorescence (or, in principle any other indicator of neuronal activity employing changes in brightness as a readout) enables researchers to analyze the spatiotemporal spread of activity patterns over different brain regions with low spatial and high temporal resolution. Specific uses of macro-scale imaging include the spatial and temporal spread of spontaneous activity in brain slices (Easton et al., 2014) or interregional synchrony *in vivo* (Busche et al., 2015).

The generic functions of SamuROI can be used to facilitate interpretation of macro-scale datasets. In our example, we would like to demonstrate how the spatiotemporal structure of a spontaneous synchronized network event is intuitively visualized and related to different brain structures using SamuROI. GCaMP6f is expressed using the AI95/NexCre mouse line. **Figure 5A** displays a sagittal slice of the parahippocampal formation, where neonatal spontaneous synchronized network events were imaged. A question we want to answer using SamuROI in this example is how the horizontal (lateral) spread of the signal in superficial layers of the parahippocampal formation is organized in time and space. The branch ROI tool we initially developed for micro-scale imaging is especially well suited for this task, demonstrating how SamuROI can be applied for image analysis flexibly at different spatial scales. As branch ROIs can have any user-defined width and direction, it is possible to generate a ROI incorporating the adjacent brain regions subiculum, presubiculum, parasubiculum and entorhinal cortex (**Figure 5A2**). The incorporation of deep and superficial layers can be adjusted by modifying the width of the branch ROI mask. Using the segmentation tool, we then divide these cortical regions into sub-regions at arbitrary spatial resolution (**Figure 5A2**). A RasterView of the sub-regions then displays the temporal and spatial dynamics of neuronal activity reflected by changes in fluorescence (**Figure 5B**) and the user can then localize individual signaling patterns like the leading edge of a wave (**Figure 5B**, red arrow) or an oscillating structure (**Figure 5B**, green and purple arrow). After clicking on the corresponding part of the RasterView widget, the corresponding segment is localized in the FrameView widget (**Figure 5A2**). The TraceView widget displays the corresponding traces (**Figure 5C**). Based on the different spatiotemporal patterns extracted from the RasterView, it is possible to draw freehand polygon-ROIs based on different patterns. This is facilitated by the time-locked intensity color code

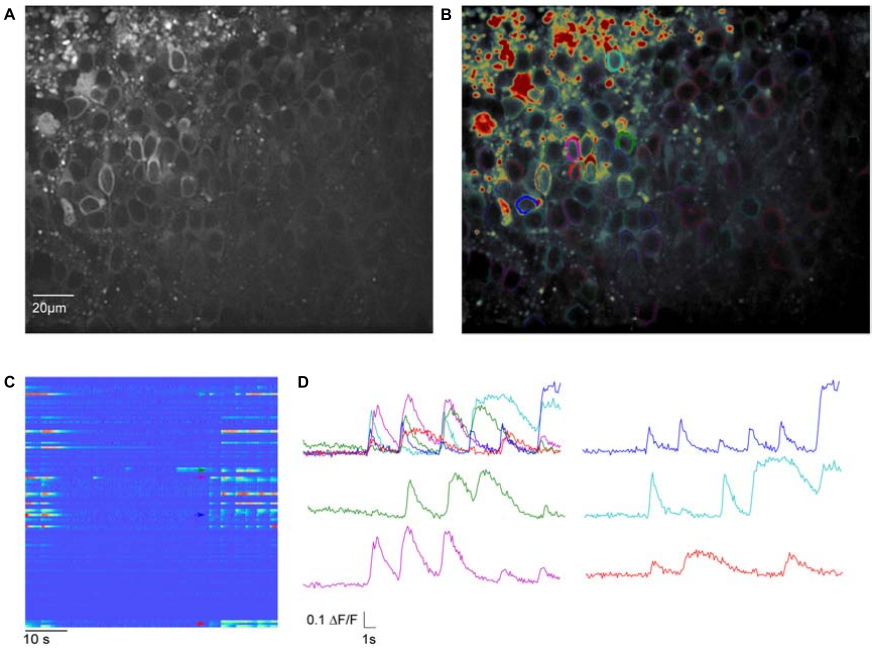

FIGURE 4 | Meso-scale imaging example for using SamuROI neuronal populations in the piriform cortex of a brain slice. **(A)** 40× magnification GCaMP6f-fluorescence summed image of a horizontal slice from the Al95/NexCre mouse in layer 2 of the piriform cortex. **(B)** The summed image loaded into SamuROI in FrameView with an overlay of color-coded cellular ROIs obtained with our mask generating function. **(C)** The RasterView displays all ROIs that are plotted. It depicts the temporal and spatial profile of neuronal activity induced changes in GCaMP6f fluorescence during a spontaneous synchronous network event. The colored arrows correspond to the highlighted cells in **(B)**. **(D)** Fluorescence traces corresponding to segments color-coded in **(B)** and **(C)**. Arrows in **(C)** depict the starting points of the corresponding traces.

in the FrameView widget. In our example, this highlights the initiation of the signal in the parasubiculum.

DISCUSSION

When studying neuronal activity with imaging, the appropriate analytical unit depends on the scientific question and size scale. Depending on spatial resolution, these analytical units could be, for example, dendritic branches, spines, single cell bodies or cortical layers and they ideally represent a unit of neuronal or network computation. Researchers aim to extract fluorescence changes specific to these analytical units, based on which they visualize, detect and localize neuronal activity patterns. Technological progress challenges researchers with the opportunity to generate increasingly complex datasets in which the ideal spatial scale is often hard to define or predict in advance.

SamuROI is built to meet the rising demand for analysis freeware. It provides an intuitive and convenient workflow for data exploration and ROI creation at arbitrary spatial scales. SamuROI is a Python-based, open source analysis environment for image series of intensity changes of fluorescent indicators over time. The software permits both data browsing and deep analysis using Python by seamlessly integrating command-line interactions with a user-friendly GUI, achieved by using Jupyter Notebooks.

As such, the software has several core strengths:

- Simplified identification of complex spatiotemporal patterns by human observation that would otherwise get lost in highly complex datasets.
- Time effective ROI management and manual curating of automatically generated ROIs from other software solutions.
- Instantaneous switching between temporal and spatial aspects of the data via interactive point and click widgets.
- Facilitation of quality control in terms of the fluorescent signal, ROI segmentation and event detection that is presented to the user.

The tool is straightforward to install. The online documentation includes code templates to illustrate usage and enable 'out of the box' use with Jupyter Notebook. While Jupyter is the recommended platform for running the GUI it

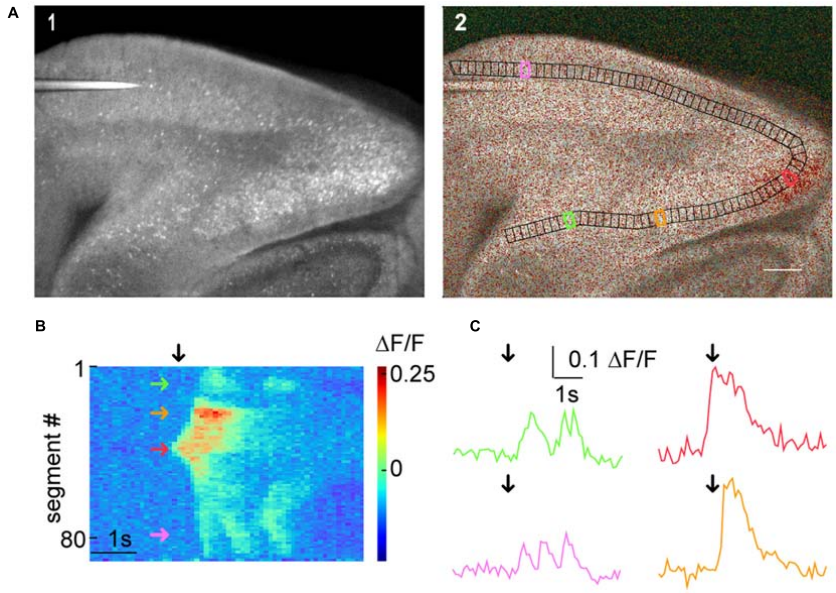

FIGURE 5 | Macro-scale imaging example for using SamuROI on different cortical regions of a brain slice. **(A)** (A1) A low magnification GCaMP6f-fluorescence image of a sagittal slice from a Al95/NexCre mouse. Different parts of the hippocampal formation are visible. (A2) Shows a morphological image with an overlay of color-coded frame specific brightness value. In black, we see a BranchMask over several hippocampal regions (subiculum, presubiculum, parasubiculum, medial entorhinal cortex, and lateral entorhinal cortex) divided into equally spaced segments. The scale bar corresponds to 200 μm. **(B)** The RasterView corresponds to the segmented BranchMask (A2). It depicts the temporal and spatial profile of neuronal activity induced changes in GCaMP6f fluorescence during a spontaneous synchronous network event. The green arrow points to a segment in the subiculum, the orange arrow to the presubiculum, the red arrow to the parasubiculum and the magenta arrow to the lateral entorhinal cortex [also see segments highlighted in corresponding colors in (A2)]. The black arrow defines the point on the *x*-axis that corresponds to the frame shown in (A2) and the time points depicted by black arrows in the traces in **(C)**. **(C)** Fluorescence traces corresponding to segments color-coded in (A2) and **(B)**.

is also possible to use SamuROI as a stand-alone application. The modularity of the pipeline permits each processing stage to be carried out independently, including pre-processing, data visualization, ROI definition, data export and event detection. Data are exported as hdf5 files, which contain all necessary information for further batch processing of the data. The package is carefully documented and open source to permit further collaborative development.

SamuROI is complementary to other existing imaging analysis software like Fiji (Schindelin et al., 2012) and SIMA (Kaifosh, 2014). These tools offer different data processing, visualization and exploration options than SamuROI. A unique feature of SamuROI is the document-view pattern based framework that permits online modification of objects in the SamuROI GUI in Python using an interactive shell like Jupyter and vice versa.

An example of integration of Fiji and SamuROI is the excellent file conversion functionality of Fiji, which enables the conversion of a larger number of file formats into Multi-tif files that can be read out by SamuROI. While Fiji offers both a neurite tracer and a ROI manager for fluorescent time series, to our knowledge there is no default way of combining the two. We found the visualization and manual curating options of ROIs generated with the Fiji ROI manager limited as there are no point and click widgets. These tools offer different visualization and exploration options to SamuROI, and can be easily used in parallel. While SIMA focuses on meso-scale population Ca^{2+} imaging *in vivo*, SamuROI aims to provide an integrated analysis environment for imaging data at what we define as the micro-scale, meso-scale and macro-scale. In addition, SIMA offers the ROI Buddy, an excellent segmentation tool for manual curating of ROIs. However, we missed an intuitive display that permits visualization and browsing of fluorescence traces. However, SamuROI by no means aims to replace any of those tools, and we encourage using these tools in parallel. For example, one might prefer to use the frame alignment procedures and ROI Buddy segmentation in SIMA as a pre-processing step followed by further analysis and visualization/exploration of the data in SamuROI. This would be an easy way to incorporate activity-based pixel correlations (Junek et al., 2009; Mukamel et al., 2009; Tomek et al., 2013; Kaifosh, 2014; Hjorth et al., 2015; Pnevmatikakis et al., 2016) to the analytical pipeline and these can be further edited in SamuROI.

One of the most critical and, when performed manually, time-consuming steps of dynamic image series analysis is the definition of ROI masks. For micro-scale Ca^{2+} imaging, we are not aware of an integrated software solution that permits both semi-automatic ROI mask generation and data browsing/analysis. On the other hand, for semiautomatic tracing of morphological data, many freeware software tools are already available for morphological segmentation of images. Software solutions like Neutube (Feng et al., 2015), Neuronstudio (Wearne et al., 2005; Rodriguez et al., 2008) or the simple neurite tracer plugin for Fiji (Longair et al., 2011) permit semi-automatic tracing of dendritic and axonal structures. SamuROI is built to interact with these, as any ROI pattern can easily be converted into an array of pixels that can be added to the attribute masks. In our online supplement, we provide examples that illustrate how ROI sets compatible with SamuROI can be generated from freeware programs validated for structure recognition. SamuROI can read SWC files (e.g., exported using Neutube (Feng et al., 2015)) and flatten these 3D dendritic tree structures into 2D branch masks. This greatly facilitates the generation of branch specific ROIs, and provides a good example how the excellent branch tracing functionality of Neutube can be combined with SamuROI.

In contrast to micro-scale imaging, there are many tools facilitating the detection of cell bodies in population Ca^{2+} imaging on the meso-scale. A number of recently developed approaches define pixels belonging to active cells based on variance in brightness using activity-based pixel correlations (Junek et al., 2009; Mukamel et al., 2009; Tomek et al., 2013; Kaifosh, 2014; Hjorth et al., 2015; Pnevmatikakis et al., 2016). These variance-based approaches work well for identifying sparsely active cells, but cannot detect silent cells nor can they always distinguish between closely packed synchronously active cells that do not fulfill the prerequisite of statistical independence. A recently published approach directly addresses this issue for postnatal early synchronous network activity (Hjorth et al., 2015). Regardless of the method used to detect cells, SamuROI can provide a useful environment for visualization and quality management of the resulting ROIs. We also provide example functions that implement polygon ROI mask creation for inactive and synchronous cells using the machine-learning based structure recognition software ilastik (Sommer et al., 2011), together with python functions based on scikit-learn and the standard python library.

Outlook

SamuROI works well with existing tools and streamlines the analysis of dynamic image series such as those acquired using Ca^{2+} indicators. SamuROI has many built in features covering a complete pipeline of data processing and analysis. While many software packages for dynamic image series analysis exist, many necessary features missing from these packages have been combined into SamuROI. Since SamuROI permits the easy import of ROI masks generated (semi-) automatically with other software tools, we do not prioritize the implementation of new segmentation algorithms in future versions of the software. Our software has been designed in such a way that event detection algorithms different from the template based algorithms based on (Clements and Bekkers, 1997) can be easily implemented. SamuROI will be used as a versatile tool for data exploration and analysis, for identifying meaningful structure in complex datasets and for convenient ROI management. SamuROI together with sophisticated structure recognition software minimizes the need for human supervision in selecting pixel-defined structures of interest. This should allow scientists to focus their attention on data scanning for recognition of meaningful patterns in the data and quality control.

AUTHOR CONTRIBUTIONS

MR and SL wrote code. FJ, LM-V, DP, and SL contributed example data. FJ, MR, and SL were involved in conceptualizing the software. FJ, LM-V, DP, SL, MR, SR, and DS designed and tested the software. FJ, SL, MR, SR, and DS prepared figures and wrote the manuscript.

FUNDING

This work was supported by the German Research Foundation (DFG), grant number JO1079/1-1, JO 1079/3-1, and SFB 665 to FJ, RU 1660, RU 1660/5-1 and IRTG 1740 to SR, Exc 257, SFB665 and SFB 958 to DS.

ACKNOWLEDGMENTS

We would like to thank Anna Vanessa Stempel and Robert Sachdev for critically reading the manuscript. In addition, we would like to thank Anke Schönherr, Susanne Rieckmann and Lisa Zuechner for excellent technical assistance.

SUPPLEMENTARY MATERIAL

The Supplementary Material for this article can be found online at: http://journal.frontiersin.org/article/10.3389/fninf.2017.00044/full#supplementary-material

REFERENCES

Beed, P., Bendels, M. H. K., Wiegand, H. F., Leibold, C., Johenning, F. W., and Schmitz, D. (2010). Analysis of excitatory microcircuitry in the medial entorhinal cortex reveals cell-type-specific differences. *Neuron* 68, 1059–1066. doi: 10.1016/j.neuron.2010.12.009

Bradski, G. (2000). The openCV library. *Dr. Dobbs J.* 25, 120–126.

Busche, M. A., Kekuš, M., Adelsberger, H., Noda, T., Förstl, H., Nelken, I., et al. (2015). Rescue of long-range circuit dysfunction in Alzheimer's disease models. *Nat. Neurosci.* 18, 1623–1630. doi: 10.1038/nn.4137

Clements, J. D., and Bekkers, J. M. (1997). Detectionof spontaneous. *Biophys. J.* 73, 220–229. doi: 10.1016/S0006-3495(97)78062-7

Conhaim, J., Cedarbaum, E. R., Barahimi, M., Moore, J. G., Becker, M. I., Gleiss, H., et al. (2010). Bimodal septal and cortical triggering and complex propagation

patterns of spontaneous waves of activity in the developing mouse cerebral cortex. *Dev. Neurobiol.* 70, 679–692. doi: 10.1002/dneu.20797

Easton, C. R., Weir, K., Scott, A., Moen, S. P., Barger, Z., Folch, A., et al. (2014). Genetic elimination of GABAergic neurotransmission reveals two distinct pacemakers for spontaneous waves of activity in the developing mouse cortex. *J. Neurosci.* 34, 3854–3863. doi: 10.1523/JNEUROSCI.3811-13.2014

Feng, L., Zhao, T., and Kim, J. (2015). neuTube 1.0: a new design for efficient neuron reconstruction software based on the SWC format. *eNeuro* 2:ENEURO.49–ENEURO.14. doi: 10.1523/ENEURO.0049-14.2014

Gamma, E., Helm, R., Johnson, R., and Vlissides, J. (2015). *Design Patterns: Elements of Reusable Object-Oriented Software*. Boston, MA: Addison-Wesley Longman Publishing Co., Inc.

Garaschuk, O., Linn, J., Eilers, J., and Konnerth, A. (2000). Large-scale oscillatory calcium waves in the immature cortex. *Nat. Neurosci.* 3, 452–459. doi: 10.1038/74823

Goebbels, S., Bormuth, I., Bode, U., Hermanson, O., Schwab, M. H., and Nave, K.-A. (2006). Genetic targeting of principal neurons in neocortex and hippocampus of NEX-Cre mice. *Genesis* 44, 611–621. doi: 10.1002/dvg.20256

Grienberger, C., and Konnerth, A. (2012). Imaging calcium in neurons. *Neuron* 73, 862–885. doi: 10.1016/j.neuron.2012.02.011

Harris, K. D., Quiroga, R. Q., Freeman, J., and Smith, S. L. (2016). Improving data quality in neuronal population recordings. *Nat. Neurosci.* 19, 1165–1174. doi: 10.1038/nn.4365

Heys, J. G., Rangarajan, K. V., and Dombeck, D. A. (2014). The functional micro-organization of grid cells revealed by cellular-resolution imaging. *Neuron* 84, 1079–1090. doi: 10.1016/j.neuron.2014.10.048

Hjorth, J. J. J., Dawitz, J., Kroon, T., Pires, J., Dassen, V. J., Berkhout, J. A., et al. (2015). Detection of silent cells, synchronization and modulatory activity in developing cellular networks. *Dev. Neurobiol.* 76, 357–374. doi: 10.1002/dneu.22319

Jia, H., Rochefort, N. L., Chen, X., and Konnerth, A. (2010). Dendritic organization of sensory input to cortical neurons in vivo. *Nature* 464, 1307–1312. doi: 10.1038/nature08947

Johenning, F. W., and Holthoff, K. (2007). Nuclear calcium signals during L-LTP induction do not predict the degree of synaptic potentiation. *Cell Calcium* 41, 271–283. doi: 10.1016/j.ceca.2006.07.005

Junek, S., Chen, T.-W., Alevra, M., and Schild, D. (2009). Activity correlation imaging: visualizing function and structure of neuronal populations. *Biophys. J.* 96, 3801–3809. doi: 10.1016/j.bpj.2008.12.3962

Kaifosh, P. (2014). SIMA: python software for analysis of dynamicfluorescence imaging data. *Front. Neuroinform.* 8:80. doi: 10.3389/fninf.2014.00080/abstract

Kleindienst, T., Winnubst, J., Roth-Alpermann, C., Bonhoeffer, T., and Lohmann, C. (2011). Activity-dependent clustering of functional synaptic inputs on developing hippocampal dendrites. *Neuron* 72, 1012–1024. doi: 10.1016/j.neuron.2011.10.015

Lang, S. B., Bonhoeffer, T., and Lohmann, C. (2006). Simultaneous imaging of morphological plasticity and calcium dynamics in dendrites. *Nat. Protoc.* 1, 1859–1864. doi: 10.1038/nprot.2006.267

Larkum, M. E., Watanabe, S., Nakamura, T., Lasser-Ross, N., and Ross, W. N. (2003). Synaptically activated Ca^{2+} waves in layer 2/3 and layer 5 rat neocortical pyramidal neurons. *J. Physiol.* 549, 471–488. doi: 10.1113/jphysiol.2002.037614

Lee, K. F. H., Soares, C., Thivierge, J.-P., and Beique, J.-C. (2016). Correlated synaptic inputs drive dendritic calcium amplification and cooperative plasticity during clustered synapse development. *Neuron* 89, 784–799. doi: 10.1016/j.neuron.2016.01.012

Longair, M. H., Baker, D. A., and Armstrong, J. D. (2011). Simple neurite tracer: open source software for reconstruction, visualization and analysis of neuronal processes. *Bioinformatics* 27, 2453–2454. doi: 10.1093/bioinformatics/btr390

Madisen, L., Garner, A. R., Shimaoka, D., Chuong, A. S., Klapoetke, N. C., Li, L., et al. (2015). Transgenic mice for intersectional targeting of neural sensors and effectors with high specificity and performance. *Neuron* 85, 942–958. doi: 10.1016/j.neuron.2015.02.022

Miyazaki, K., and Ross, W. N. (2013). Ca^{2+} sparks and puffs are generated and interact in rat hippocampal CA1 pyramidal neuron dendrites. *J. Neurosci.* 33, 17777–17788. doi: 10.1523/JNEUROSCI.2735-13.2013

Mukamel, E. A., Nimmerjahn, A., and Schnitzer, M. J. (2009). Neurotechnique. *Neuron* 63, 747–760. doi: 10.1016/j.neuron.2009.08.009

Namiki, S., Norimoto, H., Kobayashi, C., Nakatani, K., Matsuki, N., and Ikegaya, Y. (2013). Layer III neurons control synchronized waves in the immature cerebral cortex. *J. Neurosci.* 33, 987–1001. doi: 10.1523/JNEUROSCI.2522-12.2013

Nevian, T., and Helmchen, F. (2007). Calcium indicator loading of neurons using single-cell electroporation. *Pflugers. Arch.* 454, 675–688. doi: 10.1007/s00424-007-0234-2

Pnevmatikakis, E. A., Soudry, D., Gao, Y., Machado, T. A., Merel, J., Pfau, D., et al. (2016). Simultaneous denoising, deconvolution, and demixing of calcium imaging data. *Neuron* 89, 285–299. doi: 10.1016/j.neuron.2015.11.037

Rodriguez, A., Ehlenberger, D. B., Dickstein, D. L., Hof, P. R., and Wearne, S. L. (2008). Automated three-dimensional detection and shape classification of dendritic spines from fluorescence microscopy images. *PLoS ONE* 3:e1997. doi: 10.1371/journal.pone.0001997.s001

Scanziani, M., and Häusser, M. (2009). Electrophysiology in the age of light. *Nature* 461, 930–939. doi: 10.1038/nature08540

Schindelin, J., Arganda-Carreras, I., Frise, E., Kaynig, V., Longair, M., Pietzsch, T., et al. (2012). Fiji: an open-source platform for biological-image analysis. *Nat. Methods* 9, 676–682. doi: 10.1038/nmeth.2019

Schmidt-Hieber, C. (2014). Stimfit: quantifying electrophysiological data with Python. *Front. Neuroinform.* 8:16. doi: 10.3389/fninf.2014.00016

Sofroniew, N. J., Flickinger, D., King, J., and Svoboda, K. (2016). A large field of view two-photon mesoscope with subcellular resolution for in vivo imaging. *eLife* 5:e14472. doi: 10.7554/eLife.14472.001

Sommer, C., Straehle, C., and Koethe, U. (2011). "Ilastik: interactive learning and segmentation toolkit," in *Proceeding of the Biomedical Imaging: From Nano*, Chicago, IL. doi: 10.1109/isbi.2011.5872394

Stettler, D. D., and Axel, R. (2009). Representations of odor in the piriform cortex. *Neuron* 63, 854–864. doi: 10.1016/j.neuron.2009.09.005

Stosiek, C., Garaschuk, O., Holthoff, K., and Konnerth, A. (2003). In vivo two-photon calcium imaging of neuronal networks. *Proc. Natl. Acad. Sci. U.S.A.* 100, 7319–7324. doi: 10.1073/pnas.1232232100

Takahashi, N., Kitamura, K., Matsuo, N., Mayford, M., Kano, M., Matsuki, N., et al. (2012). Locally synchronized synaptic inputs. *Science* 335, 353–356. doi: 10.1126/science.1210362

Tantirigama, M. L. S., Huang, H. H. Y., and Bekkers, J. M. (2017). Spontaneous activity in the piriform cortex extends the dynamic range of cortical odor coding. *Proc. Natl. Acad. Sci. U.S.A.* 114, 2407–2412. doi: 10.1073/pnas.1620939114

Tomek, J., Novak, O., and Syka, J. (2013). Two-Photon Processor and SeNeCA: a freely available software package to process data from two-photon calcium imaging at speeds down to several milliseconds per frame. *J. Neurophysiol.* 110, 243–256. doi: 10.1152/jn.00087.2013

van der Walt, S., Schönberger, J. L., Nunez-Iglesias, J., Boulogne, F., Warner, J. D., Yager, N., et al. (2014). scikit-image: image processing in Python. *PeerJ* 2:e453. doi: 10.7717/peerj.453/fig-5

Wearne, S. L., Rodriguez, A., Ehlenberger, D. B., Rocher, A. B., Henderson, S. C., and Hof, P. R. (2005). New techniques for imaging, digitization and analysis of three-dimensional neural morphology on multiple scales. *Neuroscience* 136, 661–680. doi: 10.1016/j.neuroscience.2005.05.053

Conflict of Interest Statement: The authors declare that the research was conducted in the absence of any commercial or financial relationships that could be construed as a potential conflict of interest.

Supplementary Methods

Overlay thresholding algorithm

SamuROI can use a two-dimensional grey scale morphology image to automatically create a mask around relevant objects in the morphology.

The mask can be visualised from the GUI and has to be validated manually. It is calculated as follows:

1. compute percentile of morphology image and use it as initial threshold value
2. apply Sobel filter (from scikit image) to morphology image and create an elevation map
3. create a marker image where pixels get marked that are close to the threshold
4. run watershed algorithm (from scikit morphology)
5. user inspects result and potentially adapts threshold value

For the specific implementation see the SamuROIData implementation and the scikit image documentation.

Fluorescence renormalization

SamuROI comes with three different ways to renormalize the raw fluorescence data F which depends on space (x,y) and time (t):

1. via standard deviation: in this case the video data is segmented into different blocks, each containing B frames. Then the standard deviation is calculated for every pixel in each block over the frames of that block. Then the block with the minimum standard deviation is selected for each pixel and the baseline fluorescence is calculated as the mean of these blocks resulting in a baseline image $F_0(x,y)$
2. via a linear fit: To account for small bleaching effects a linear fit is calculated for the time series of each pixel. With the resulting slopes $m_{x,y}$ and offsets $o_{x,y}$, F_0 is defined as $F_0(x,y,t)=m_{x,y}t + o_{x,y}$.

3. via the median over individual frames: in this case F_0 does not depend on spatial coordinates and is simply defined as $F_0(t)=\text{median}(F(x,y,t))$, where the median operates on all pixels of individual frames.

In all cases the calculation of $\Delta F/F = (F-F_0)/F_0$ from the above definition is implemented via numpy's array broadcasting functionality.

16. Journal Summary List (ISi Web of KnowledgeSM): Publication 3

Journal Data Filtered By: **Selected JCR Year: 2018** Selected Editions: SCIE,SSCI Selected Categories: **"MULTIDISCIPLINARY SCIENCES"** Selected Category Scheme: WoS

Gesamtanzahl: 69 Journale

Rank	Full Journal Title	Total Cites	Journal Impact Factor	Eigenfactor Score
1	NATURE	745,692	43.070	1.285010
2	SCIENCE	680,994	41.037	1.070190
3	National Science Review	1,842	13.222	0.006500
4	Science Advances	21,901	12.804	0.110010
5	Nature Communications	243,793	11.878	1.103290
6	Nature Human Behaviour	1,230	10.575	0.006550
7	PROCEEDINGS OF THE NATIONAL ACADEMY OF SCIENCES OF THE UNITED STATES OF AMERICA	661,118	9.580	1.022190
8	Science Bulletin	3,569	6.277	0.009840
9	Scientific Data	3,240	5.929	0.015610
10	Frontiers in Bioengineering and Biotechnology	1,994	5.122	0.006540
11	Journal of Advanced Research	2,691	5.045	0.004780
12	Research Synthesis Methods	1,932	5.043	0.005420
13	GigaScience	2,674	4.688	0.012510
14	Annals of the New York Academy of Sciences	46,385	4.295	0.025840
15	Scientific Reports	302,086	4.011	1.061540
16	Journal of the Royal Society Interface	12,933	3.224	0.029190
17	NPJ Microgravity	203	3.111	0.000670
18	PHILOSOPHICAL TRANSACTIONS OF THE ROYAL SOCIETY A-MATHEMATICAL PHYSICAL AND ENGINEERING SCIENCES	19,227	3.093	0.028200

17. Publication 3: Species-specific differences in synaptic transmission and plasticity

www.nature.com/scientificreports

SCIENTIFIC REPORTS
nature research

Check for updates

OPEN

Species-specific differences in synaptic transmission and plasticity

Prateep Beed[1,2,8]✉, Saikat Ray[3,4,8]✉, Laura Moreno Velasquez[1,8], Alexander Stumpf[1,8], Daniel Parthier[1], Aarti Swaminathan[1], Noam Nitzan[1], Jörg Breustedt[1], Liora Las[4], Michael Brecht[3] & Dietmar Schmitz[1,2,5,6,7]✉

Synaptic transmission and plasticity in the hippocampus are integral factors in learning and memory. While there has been intense investigation of these critical mechanisms in the brain of rodents, we lack a broader understanding of the generality of these processes across species. We investigated one of the smallest animals with conserved hippocampal macroanatomy—the Etruscan shrew, and found that while synaptic properties and plasticity in CA1 Schaffer collateral synapses were similar to mice, CA3 mossy fiber synapses showed striking differences in synaptic plasticity between shrews and mice. Shrew mossy fibers have lower long term plasticity compared to mice. Short term plasticity and the expression of a key protein involved in it, synaptotagmin 7 were also markedly lower at the mossy fibers in shrews than in mice. We also observed similar lower expression of synaptotagmin 7 in the mossy fibers of bats that are evolutionarily closer to shrews than mice. Species specific differences in synaptic plasticity and the key molecules regulating it, highlight the evolutionary divergence of neuronal circuit functions.

The Etruscan shrew *(Suncus etruscus)* is the smallest terrestrial mammal, with a full-grown adult weighing ~ 2 g and having a brain volume of ~ 60 mm^3[1,2]. It is approximately 15 times smaller in body size and has a brain ~ 7 times smaller than a lab mouse. They hunt for their food, and prey on insects like crickets—consuming multiple times their body weight every day, primarily using somatosensory input from their whiskers[3] to guide hunting. Despite the minutely sized brain, the overall layout of the brain is rather similar to other mammalian brains, with a 6-layered cortex[1,2] and conserved genetic and architectural features in the neocortex and hippocampal formation[1,2,4].

The hippocampus is a key structure in learning and memory in the central nervous system, and activity dependent changes in synaptic strength are thought to be the underlying cellular correlate[5–9]. Information to the hippocampus is routed from the neocortex through the evolutionarily conserved trisynaptic pathway[10]. The mossy fiber and the Schaffer collateral synapses are among the most investigated synapses in neuroscience—though most investigation has been limited to rodent studies. As the Etruscan shrew is one of the smallest animals with clearly defined hippocampal substructures, and features these two synapses, we compared the anatomy and physiology of these two synapses in the Etruscan shrew and in mice.

We first investigated the architecture of the hippocampus of the shrew, to determine if tissue size and space constraints affect the structural layout of hippocampal circuits. The overall layout of the hippocampus in shrews is similar to other mammalian species, with classical subfields like the dentate gyrus, CA1, CA2 and CA3 (Fig. 1). These areas can be easily distinguished by similar cytoarchitecture (Fig. 1a,b), cell densities (Fig. 1c) and consistent histochemical and immunohistochemical features (Fig. 1d–g) between shrews and mice. Histochemistry and immunohistochemistry also reveals that the major fiber pathways like the mossy fiber pathway are also conserved, with the mossy fibers in CA3 being enriched in synaptic zinc (Fig. 1e, brown) and the calcium binding protein

[1]Neuroscience Research Center, Charité-Universitätsmedizin Berlin, Berlin, Germany. [2]Berlin Institute of Health, 10178 Berlin, Germany. [3]Bernstein Center for Computational Neuroscience, Humboldt University of Berlin, Philippstr. 13, Haus 6, 10115 Berlin, Germany. [4]Department of Neurobiology, Weizmann Institute of Science, 76100 Rehovot, Israel. [5]German Center for Neurodegenerative Diseases (DZNE), 10117 Berlin, Germany. [6]Cluster of Excellence NeuroCure, 10117 Berlin, Germany. [7]Einstein Center for Neurosciences Berlin, 10117 Berlin, Germany. [8]These authors contributed equally: Prateep Beed, Saikat Ray, Laura Moreno Velasquez and Alexander Stumpf. ✉email: prateep.beed@charite.de; saikat.ray@weizmann.ac.il; dietmar.schmitz@charite.de

Figure 1. Macroanatomy of the Etruscan shrew hippocampus is similar to mice. Sagittal sections stained for DAPI showing the hippocampus of (**a**) shrew and (**b**) mice indicating the different subregions of the hippocampus—dentate gyrus (DG), CA1, CA3 and the pyramidal (Py), Stratum Radiatum (Sr) and Stratum Lucidum (SL) layers. (**c**) Relative cell densities in different hippocampal subregions do not differ between shrews (green) and mice (purple), indicating conserved cytoarchitectonic layout (p-values based on Mann–Whitney two tailed test.). (**d**,**f**) Saggital section of an Etruscan shrew hippocampus labelled for calbindin (CB, green) and DAPI (blue) indicating the different hippocampal subregions—CA1, CA2, CA3, dentate gyrus (DG) and mossy fibers (mf). (**e**) Mossy fibers (mf) visualized by the presence of synaptic zinc (brown) in a sagittal section of an Etruscan shrew brain, and CA2 labelled by the presence of the protein PCP4 (yellow) show that the mossy fibers are present in CA3 and terminate at the CA2 region. (**g**) Sagittal section of a mouse, marked same as (**f**). (**h**) Relative convergence ratios between mossy fiber intensities and cell density reveal a higher mossy fiber to CA3 pyramidal cell convergence factor in shrews than in mice.

calbindin (CB, green; Fig. 1d,f). The mossy fibers extend through the entire CA3 region in the stratum lucidum layer and terminate at the CA2 region—which has neurons expressing the protein purkinje cell protein 4 (PCP4, yellow; Fig. 1e). However, the anatomy of mossy fibers in shrews indicates subtle differences with shrews having a slightly higher relative convergence ratio of mossy fiber inputs (Fig. 1f–h) in CA3 than mice.

We then explored if there were any corresponding differences in synaptic transmission and plasticity in the mossy fiber pathway. We recorded mossy fiber fEPSPs from sagittal slices of shrews using the same solutions and slicing procedure as used for mice (Fig. S1a). Mossy fiber inputs showed fEPSP/ fiber volley (FV) ratio similar to that in mice as well as its sensitivity to the agonist for the group II metabotropic glutamate receptors, dcg iv (Fig. S1b–d, Table S1). Therefore, synaptic transmission at the shrew mossy fiber is similar to that in mice.

The plasticity at the mossy fiber synapse is primarily presynaptic[11,12]. Most of the unique parameters that classifies mossy fibers as detonator synapses are due to its short-term plasticity (STP) such as 1 Hz frequency facilitation, paired-pulse ratio and post-tetanic potentiation. We investigated these short-term plasticity features at the mossy fiber synapse in shrews and compared it to mice. Surprisingly, we found that shrew mossy fiber synapses are much less plastic than those in mice, even though the relative convergence ratio of mossy fiber inputs in CA3 is higher in shrews than in mice (Fig. 1h). Frequency facilitation was measured by stimulating the mossy fiber inputs twenty times (Fig. 2a1,a2, sweeps 10–30) at 1 Hz. The ratio of the 30th (marked as 2 in Fig. 2a1) to the 10th (marked as 1 in Fig. 2a1) sweep was calculated for both shrews and mice to determine the frequency facilitation: we found that shrews had a much lower facilitation in comparison with mice (Fig. 2a3 shrews: 2.41 ± 0.26 fold increase, $n = 15$ recordings; mice: 6.34 ± 0.46 fold increase, $n = 13$ recordings, $p < 0.0001$, Mann–Whitney unpaired test). Paired pulse ratio (PPR) was calculated as the peak of second EPSP to the first EPSP which had an inter-pulse interval of 50 ms (Fig. 2b1). Paired pulse ratio was also significantly lower: shrews—1.72 ± 0.12, $n = 13$ recordings; mice—2.69 ± 0.29, $n = 13$ recordings, $p = 0.0002$, Mann–Whitney unpaired test (Fig. 2b2). Lastly to determine the post-tetanic potentiation (PTP) we stimulated $4\times$ at an interval of 20 s and each stimulus had 125 pulses at 25 Hz. PTP was determined as the average of the 3 sweeps following the repetitive stimulation. Here, we found a dramatic difference in the amount of PTP, with shrews having a much lower PTP than mice—shrews: 2.12 ± 0.17, $n = 15$ recordings; mice: 9.34 ± 1.32, $n = 13$ recordings, $p < 0.0001$, Mann–Whitney unpaired test (Fig. 2c1). When lowering extracellular Ca concentration from 2.5 to 1.5 mM, we observed the predicted change in fEPSP/FV ratio; however, shrews showed only moderate changes in PPR (paired-pulse facilitation, Fig. S2a–c, Table S1).

Finally, we analyzed LTP at this particular synapse. Following a stable baseline of synaptic transmission, we induced plasticity by using tetanic stimuli as mentioned above—a protocol which has been successfully used in many different preparations[27]. At this particular synapse there is a significantly lower level of LTP in shrews as compared to mice (Fig. 2d1–d3). Although lower than mice, mossy fiber LTP in shrews was significantly different from the mean normalized value of 1 (one-sample t-test, $p = 0.045$).

The calcium sensing protein, synaptotagmin 7 (Syt7) plays an important and reversible role in mediating short term plasticity[13]. To investigate if this molecular substrate contributes to the underlying difference between mice and shrews, we performed immunohistochemical investigation for the presence Syt7. Low levels of Syt7 leads to markedly lower plasticity potential at synapses like the mossy fibers, where the presynaptic side dominates[13]. Immunohistochemical processing of hippocampal sections with calbindin in shrews (Fig. 3a) and mice (Fig. 3d) marks the mossy fibers. Co-processing the same sections for Syt7 (Fig. 3b,e) shows strikingly lower levels of Syt7 expression in the shrew compared to mice mossy fibers (overlays in Fig. 3c,f,g, Table S1), despite a higher convergence ratio of mossy fibers from the dentate gyrus to the CA3 in shrews (Fig. 1h, Table S1). This posits Syt7 as a strong candidate for the observed differences in short-term plasticity at the mossy fiber between shrews and mice. To assess the evolutionary basis of these species differences in synaptotagmin 7 expression, and thus perhaps short term plasticity, we extended our anatomical studies to Egyptian fruit bats (*Rousettus aegyptiacus*), which genomic studies have indicated are evolutionarily closer to shrews than mice[4,26] (Fig. 4a). Indeed, we saw that Syt7 expression in the bat and shrew hippocampus followed a similar pattern—with comparatively lower expression of Syt7 in CA3 than in CA1, than that observed in mice (Fig. 4b–g, Table S1).

We then assessed if the differences in synaptic transmission and plasticity in shrews were limited to CA3 mossy fibers, or extended also to the CA1 Schaffer collateral pathway. We therefore performed both field (with synaptic stimulation of the Schaffer collateral synapses) and whole cell recordings of shrew CA1 pyramidal cells to investigate the properties of synaptic transmission, plasticity and single cell morphological and electrophysiogical features. We found no differences in input/output behaviour as well as in short-term and long-term plasticity in area CA1 of the hippocampus of the shrews (Fig. 5a–c) compared to that observed in mice[28]. We also investigated the basic cellular physiology of CA1 pyramidal neurons by performing whole-cell patch clamp recordings

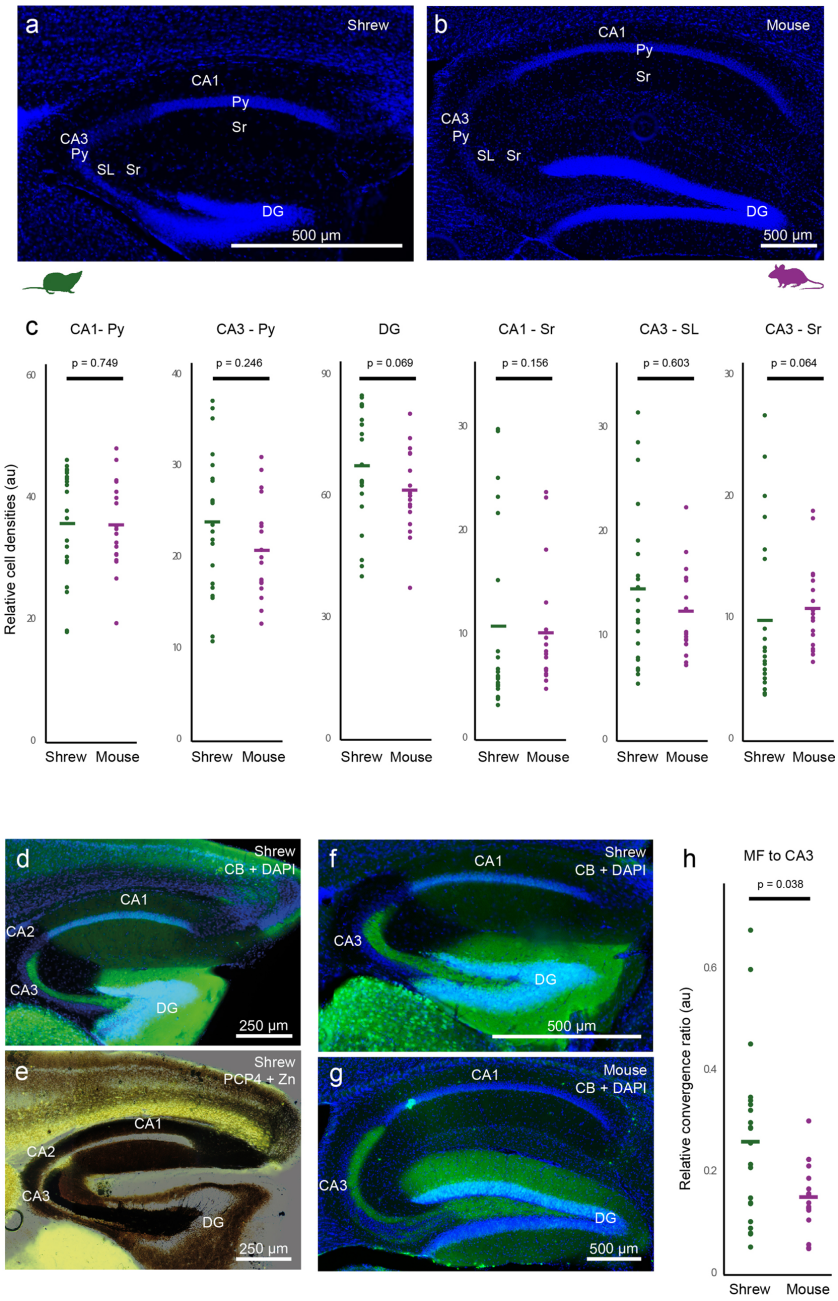
a
Shrew
CA1
Py
Sr
CA3
Py
SL Sr
DG
500 µm
b
Mouse
CA1
Py
Sr
CA3
Py
SL Sr
DG
500 µm
c
CA1- Py
CA3 - Py
DG
CA1 - Sr
CA3 - SL
CA3 - Sr
p = 0.749
p = 0.246
p = 0.069
p = 0.156
p = 0.603
p = 0.064
Relative cell densities (au)
Shrew Mouse
d
Shrew
CB + DAPI
CA1
CA2
CA3
DG
250 µm
e
Shrew
PCP4 + Zn
CA1
CA2
CA3
DG
250 µm
f
CA1
Shrew
CB + DAPI
CA3
DG
500 µm
g
CA1
Mouse
CB + DAPI
CA3
DG
500 µm
h
MF to CA3
p = 0.038
Relative convergence ratio (au)
Shrew Mouse

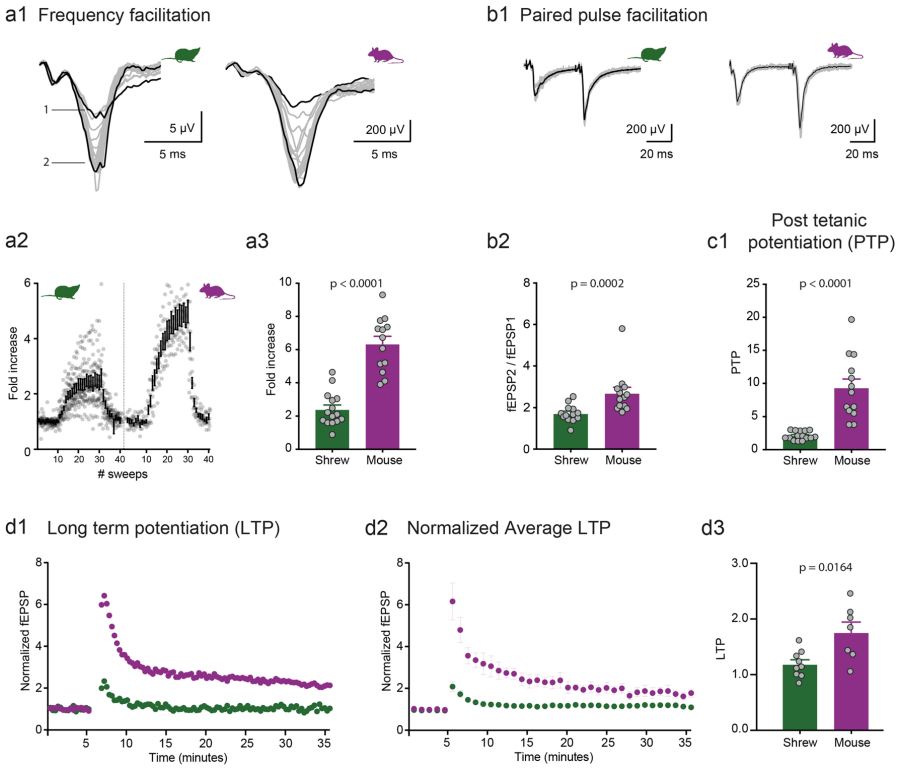

Figure 2. Low synaptic plasticity at mossy fiber synapse of the Etruscan shrew. Different short-term plasticity parameters are quantified and compared at the mossy fiber synapse between shrews (green) and mice (purple). (**a1**) 1 Hz frequency facilitation in shrews versus mice. (**a2**) Lower frequency facilitation in shrews as compared to mice in (**a3**). (**b1**) Paired pulse facilitation with 50 ms inter pulse interval is also lower in shrews as compared to mice in (**b2**). (**c1**) Following 4 × tetanic stimulation, the post-tetanic potentiation was also compared between shrews and mice. Several-folds lower potentiation in shrews as compared to mice. Long-term plasticity at the mossy fiber synapse between shrews (green) and mice (purple). (**d1**) Single example of mossy fiber LTP in shrew (green) versus mouse (purple). (**d2**) Average LTP data shows lower levels of mossy fiber LTP in shrews as compared to mice. (**d3**) Shrews show lower levels of mossy fiber LTP as compared to mice.

(Fig. S3). We investigated both anatomical details (Fig. S3a,b,c1,c2) and intrinsic cellular properties. Intrinsic properties such as firing pattern and resting membrane potential (Fig. S3d1), input resistance (Fig. S3d2), action potential threshold (Fig. S3d3), action potential amplitude (Fig. S3d4) and action potential FWHM (Fig. S3d5) were similar to the values observed in mice[14]. Similarly, single cell anatomical structures indicate no apparent difference to those reported in mice[14]. Overall this indicated that in shrews the basic properties of cellular architecture and physiology, synaptic transmission and plasticity are largely similar to those observed in well investigated species like mice. However, specific changes in molecular architecture and correlated changes in plasticity at the CA3 mossy fiber synapse points towards species specific adaptation of neural microcircuits.

The mossy fiber synapse in mice has been postulated to work as a detonator synapse[15,16], with synaptic facilitation due to short term plasticity allowing the synapse to go into a detonation mode, where one spike from a presynaptic granule cell would be sufficient to induce a postsynaptic spike in the postsynaptic CA3 pyramidal neurons. However, shrews show low STP, and based on anatomical similarities, we predict that bats might also have similarly low levels of short-term plasticity. Thus the feasibility of the mossy fiber synapse to act as a detonator synapse might be limited to certain species and perhaps not a general phenomenon.

The importance in learning and memory of the hippocampus has been thoroughly investigated, and hippocampal LTP in general has been observed to be important in the process of spatial learning and memory. However, the investigation of the behavioural impact of mossy fiber synaptic transmission and LTP has not been conclusive, and has produced contradictory findings, with some studies finding that the lack or alterations of mossy fiber transmission results in impaired memory[17–19], while others indicate there are no such effects[20,21]. However, even though shrews have comparatively lower mossy fiber LTP than mice, they can show spatial memory and

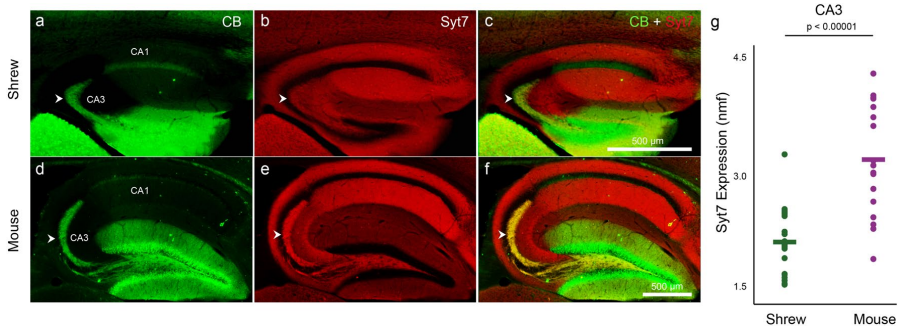

Figure 3. Etruscan shrew mossy fibers have low synaptotagmin 7. Hippocampal mossy fibers (white arrowheads) are labeled with calbindin (green) in shrews (**a**) and mice (**d**). The same sections co-labeled with synaptotagmin 7 (**b**,**e**; Syt7, red) and overlaid in (**c**) and (**f**) respectively, show low Syt7 expression in the shrew CA3-mossy fibers (**b**,**c**) but not in mice (**e**,**f**). Note the yellow colour of the mossy fibers in (**f**) but not in (**c**) due to the lack of Syt7 in shrews. Quantification of normalized mean fluorescence levels of Syt7 in shrews and mice (**g**) indicates that the CA3-mossy fibers in shrews have lower Syt7 expression than mice. Scale bar in (**c**) and (**f**) also applies to (**a**,**b**) and (**c**,**d**) respectively.

hoard food stashes both close and away from their nests[22] and learn new strategies for hunting[3]. This seems to indicate that plasticity at the mossy fiber synapse might only play a limited role in spatial memory—however its involvement might vary in other forms of episodic-like memories such as contextual memory formation.

In summary, we show that plasticity at the mossy fiber synapse in shrews is markedly distinct—with several fold lower levels of short term plasticity and long term potentiation than that observed in mice. The lower levels of expression of the protein synaptotagmin 7 in shrew mossy fibers might contribute to the physiological differences observed in plasticity. Our findings suggest that while the basic layout of classical circuits like the mossy fiber pathway might be conserved across different mammals, specific genetic differences among them can result in distinct physiology of these circuits and question the functional and behavioural impact of plasticity at the hippocampal mossy fiber synapse.

Methods

Animal husbandry and experimental interventions were performed in accordance with the German Animal Welfare Act and European Council Directive 86/609/EEC regarding the protection of animals used for experimental and other scientific purposes. All experimental procedures and maintenance of mice were conducted in accordance with permission from local regulatory authorities (Berlin Landesamt für Gesundheit und Soziales, permit T0100/03). All experimental procedures and maintenance of shrews were conducted in accordance with permission from local regulatory authorities (Berlin Landesamt für Gesundheit und Soziales, permits T0160/14 and T0078/16). Bat brains were obtained from experimental procedures approved by the Institutional Animal Care and Use Committee of the Weizmann Institute of Science.

Electrophysiology. Slice preparation and electrophysiogical recordings were done as described before[28,29].

Slice preparation. Shrews and mice of both sexes (2–3 months old) were anesthetized with isofluorane and decapitated. The brain was quickly removed and chilled in ice-cold sucrose-artificial cerebrospinal fluid (sACSF) containing (in mM): 50 NaCl, 25 $NaHCO_3$, 10 glucose, 150 sucrose, 2.5 KCl, 1 NaH_2PO_4, 0.5 $CaCl_2$, and 7 $MgCl_2$ for Mossy fiber recordings and 87 NaCl, 26 $NaHCO_3$, 10 glucose, 50 sucrose, 2.5 KCl, 1.25 NaH_2PO_4, 0.5 $CaCl_2$, and 3 $MgCl_2$ for Schaffer collateral recordings. All solutions were saturated with 95% O2 (vol/vol) and 5% CO2 (vol/vol), pH 7.4.

Slices (400 µm, sagittal) were cut with a Leica VT1200S microtome (Wetzlar, Germany) and stored submerged in sACSF for 30 min at 35 °C and subsequently stored in ACSF containing (in mM): 119 NaCl, 26 $NaHCO_3$, 10 glucose, 2.5 KCl, 1 NaH_2PO_4, 2.5 $CaCl_2$ and 1.3 $MgCl_2$ saturated with 95% O2 (vol/vol) 5% CO_2 (vol/vol), pH 7.4, at RT. Experiments were started 1–6 h after the preparation.

Electrophysiological recordings. Electrophysiogical recordings were done as described before[28,29]. In brief, slices were placed in a recording chamber continuously superfused with ACSF at RT at a rate of 2.5 ml/min. fEPSPs were evoked by electrical stimulation with patch pipettes filled with ACSF. fEPSPs were recorded with a low-resistance patch-pipette filled with ACSF. Recordings were performed with a MultiClamp 700B amplifier. Signals were filtered at 2 kHz and digitized (BNC-2090; National Instruments Germany GmbH) at 10–20 kHz. IGOR Pro software was used for signal acquisition (WaveMetrics, Inc.).

For Mossy fiber recordings, stimulation electrodes were placed in the granule cell layer or in the hilus region. Mossy fiber origin of recorded signals was verified by frequency facilitation and a reduction of 80% of the responses upon DCGIV (1 µM; Tocris) application at the end of each experiment. fEPSPs in area CA1 were

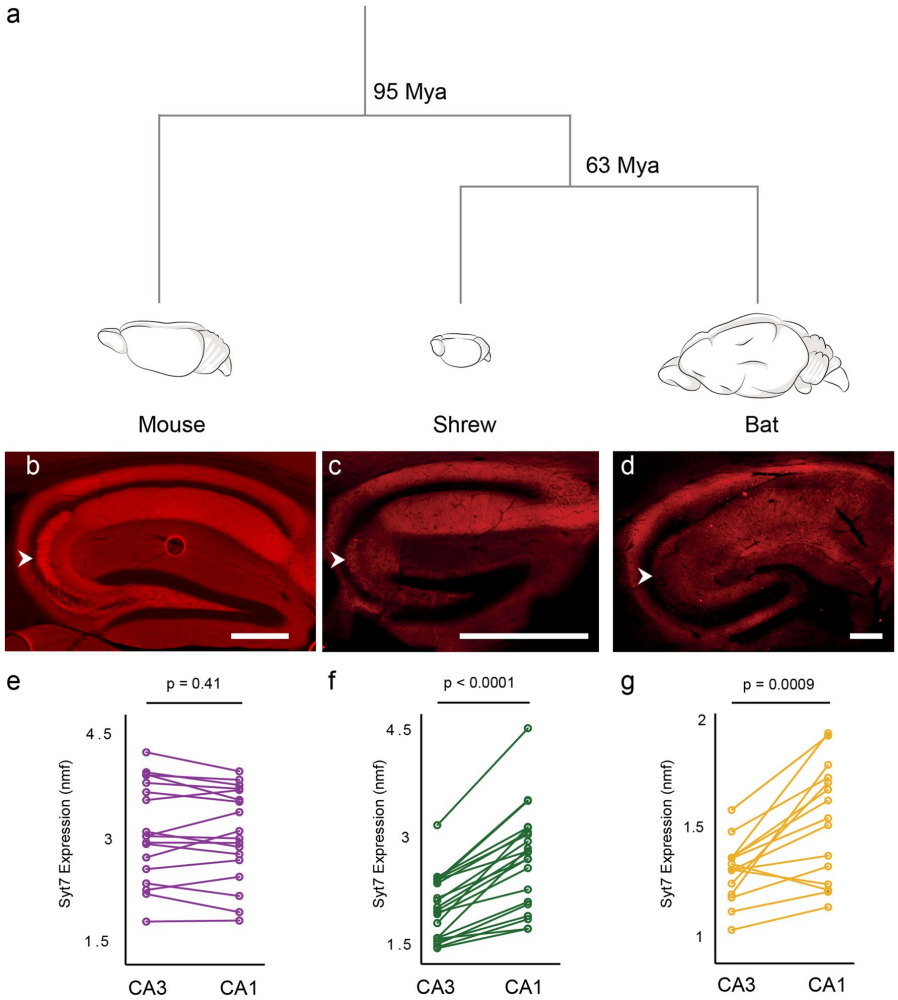

Figure 4. Synaptotagmin 7 distribution in CA3 and CA1 of mice, shrews and bats. (**a**) Evolutionary time-line between mice, shrews and bats shows bats are closer relatives of shrews than mice [4,26]. (**b**–**d**) Syt 7 expression in the hippocampus of mice in (**b**), shrews in (**c**) and bats in (**d**). White arrowheads indicate the mossy fibers. (**e**–**f**) Quantification of Syt 7 between CA3 and CA1 area of mice in (**e**), shrews in (**f**) and bats in (**g**). Expression patterns of Syt 7 are similar between bats and shrews compared to mice which correlates well with their phylogeny. Scale bars 500 µm.

recorded in stratum radiatum after stimulation of the Schaffer collaterals. fEPSP magnitude was determined by analyzing ± 2 ms of the amplitude peak. Data were analyzed with the Igor plug-in NeuroMatic (neuromatic.thinkrandom.com) software. Statistical analysis was performed with Prism 6 (GraphPad Software).

Anatomy. *Brain tissue preparation.* Brain tissue preparation were done as described before[23–25]. In brief, male and female mice, Etruscan shrews and Egyptian fruit bats (n = 20 mice, 20 shrews, 5 bats) were used in the study.

Animals were anaesthetized by isoflurane, and then euthanized by an intraperitoneal injection of 20% urethane. They were then perfused transcardially with first 0.9% phosphate buffered saline solution, followed by 4% formaldehyde, from paraformaldehyde, in 0.1 M phosphate buffer (PFA). Subsequently, brains were removed from the skull and postfixed in PFA overnight. Brains were then transferred to 10% sucrose solution for one night and subsequently immersed in 30% sucrose solution for at least one night for cryoprotection. The brains

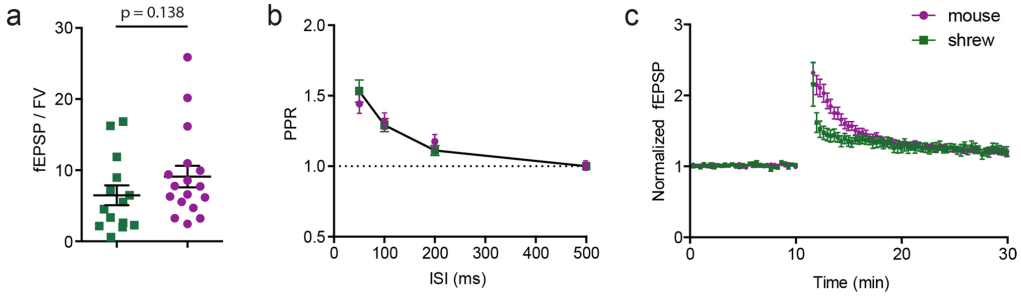

Figure 5. CA1 Schaffer collateral synapse in the shrew and mouse. (**a**) Field EPSP to presynaptic fiber volley ratio. (**b**) Paired pulse ration at 4 different time intervals of 50 ms, 100 ms, 200 ms and 500 ms. (**c**) LTP at this synapse is comparable between shrew and mouse.

were embedded in Jung Tissue Freezing Medium (Leica Microsystems Nussloch, Germany), and subsequently mounted on the freezing microtome (Leica 2035 Biocut) to obtain 20–60 µm thick sagittal sections or tangential sections parallel to the pia.

Sagittal sections of the hippocampus were obtained by first separating the two hemispheres. The hemisphere was then positioned with the medial surface of the brain being attached to the block face of the microtome to obtain sections.

Histochemistry and immunohistochemistry. Hisotchemistry for visualization of synaptic zinc was performed as described previously[23]. In brief, sections were exposed to a solution containing gum arabic, citrate buffer, hydroquinone and silver lactate for 60–120 min, in the dark at room temperature. Development of reaction products was checked under a microscope and terminated by rinsing the sections in 0.01 M PB and, subsequently, several times in 0.1 M PB.

Immunohistochemical stainings were performed according to standard procedures and as described previously[24,25]. Briefly, brain sections were pre-incubated in a blocking solution containing 0.1 M PBS, 2% Bovine Serum Albumin (BSA) and 0.5% Triton X-100 (PBS-X) for an hour at room temperature (RT). Following this, primary antibodies were diluted in a solution containing PBS-X and 1% BSA. Primary antibodies against the calcium binding proteins Calbindin (Swant: CB300, CB 38; 1:5000), the calmodulin binding protein Purkinje cell protein 4 (Sigma: HPA005792; 1:200) and the calcium sensing protein Synaptotagmin 7 (Synaptic Systems: 105173; 1:200) were used. Incubations with primary antibodies were allowed to proceed for at least 24 h under mild shaking at 4 °C in free-floating sections. Incubations with primary antibodies were followed by detection with secondary antibodies coupled to different fluorophores (Alexa 488, 546 and 633; Invitrogen). Secondary antibodies were diluted (1:500) in PBS-X and the reaction allowed to proceed for two hours in the dark at RT. For multiple antibody labeling, antibodies raised in different host species were used. For visualizing cell nuclei, sections were counterstained with DAPI (Molecular Probes: R37606). After the staining procedure, sections were mounted on gelatin coated glass slides with Vectashield mounting medium (Vectorlabs: H-1000).

Image acquisition. Similar to our previous studies[23–25] an Olympus BX51 microscope (Olympus, Shinjuku Tokyo, Japan) equipped with a motorized stage (LUDL Electronics, Hawthorne NY, USA) and a z-encoder (Heidenhain, Shaumburg IL, USA), was used for bright field microscopy. Images were captured using a MBF CX9000 (Optronics, Goleta CA, USA) camera using Neurolucida or StereoInvestigator (MBF Bioscience, Williston VT, USA). A Leica DM5500B epifluorescence microscope with a Leica DFC345 FX camera (Leica Microsystems, Mannheim, Germany) was used to image the immunofluorescent sections. Alexa fluorophores were excited using the appropriate filters (Alexa 350—A4, Alexa 488—L5, Alexa 546—N3, Alexa 633—Y5). Fluorescent images were acquired in monochrome, and color maps were applied to the images post acquisition. Post hoc linear brightness and contrast adjustment were applied uniformly to the image under analysis.

Image analysis. Analysis of mean fluorescence intensities were performed on microscope images without any adjustments, in ImageJ. Specifically, region of interests were marked around mossy fibers in the suprapyramidal layer in CA3 stratum lucidum; the DG granule cell layer; the CA1 stratum radiatum; the CA3 stratum radiatum and the CA1 and CA3 pyramidal cell layer regions. Mean fluorescence intensities were measured using ImageJ. Cell density estimates were based on mean on mean fluorescent intensity from the DAPI for different subregions. For normalization of syt7 measurements, the intensities from mossy fibers were divided with those obtained from the granule cell region—as the granule cell region lacked syt7 expression and the intensities were related to unspecific background fluorescence. For quantification of CB intensities, the same regions were used as for the syt7 for determining mean fluorescence intensity in mossy fiber regions with normalization performed with background intensities from CA3 stratum radiatum region. Mossy fiber convergence ratios were determined by dividing normalized CB intensities in mossy fibers with cell density estimates obtained for CA3 pyramidal cell layer region.

Received: 2 May 2020; Accepted: 15 September 2020
Published online: 06 October 2020

References

1. Naumann, R. K., Anjum, F., Roth-Alpermann, C. & Brecht, M. Cytoarchitecture, areas, and neuron numbers of the Etruscan shrew cortex. *J Comp Neurol.* **520**(11), 2512–2530 (2012).
2. Ray, S. Li, M., Mueller, S., Boehm-Sturm, P., Brecht, M., Naumann, R. K. Seasonal plasticity in the adult somatosensory cortex. Program No. 486.16. Neuroscience Meeting Planner. Chicago, IL: Society for Neuroscience, Online (2019).
3. Anjum, F. & Brecht, M. Tactile experience shapes prey-capture behavior in Etruscan shrews. *Front. Behav. Neurosci.* **6**, 28 (2012).
4. Naumann, R. K. *et al.* Conserved size and periodicity of pyramidal patches in layer 2 of medial/caudal entorhinal cortex. *J. Compar. Neurol.* **524**(4), 783–806 (2016).
5. Hebb, D. O. *The organization of behaviour* (Wiley, New York, 1949).
6. Malenka, R. C. Synaptic plasticity in the hippocampus: LTP and LTD. *Cell* **78**(4), 535–538 (1994).
7. Martin, S. J., Grimwood, P. D. & Morris, R. G. M. Synaptic plasticity and Memory: an evaluation of the hypothesis. *Annu. Rev. Neurosci.* **23**, 649–711 (2000).
8. McNaughton, B. L. & Morris, R. G. Hippocampal synaptic enhancement and information storage within a distributed memory system. *Trends Neurosci.* **10**(10), 408–415 (1987).
9. Squire, L. R. *Memory and brain* (Oxford UP, New York, 1987).
10. Lorente de No, R. Studies on the structure of the cerebral cortex II. Continuation of the study of the Ammonic system. *J. Psychol. Neurol. (Lpz.)* **46**, 113–177 (1934).
11. Monday, H. R., Younts, T. J. & Castillo, P. E. Long-term plasticity of neurotransmitter release: emerging mechanisms and contributions to brain function and disease. *Annu. Rev. Neurosci.* **41**, 299–322 (2018).
12. Nicoll, R. A. & Schmitz, D. Synaptic plasticity at hippocampal mossy fibre synapses. *Nat. Rev. Neurosci.* **6**(11), 863 (2005).
13. Jackman, S. L., Turecek, J., Belinsky, J. E. & Regehr, W. G. The calcium sensor synaptotagmin 7 is required for synaptic facilitation. *Nature* **529**(7584), 88 (2016).
14. Routh, B. N., Johnston, D., Harris, K. & Chitwood, R. A. Anatomical and electrophysiological comparison of CA1 pyramidal neurons of the rat and mouse. *J. Neurophysiol.* **102**(4), 2288–2302 (2009).
15. Henze, D. A., Urban, N. N. & Barrionuevo, G. The multifarious hippocampal mossy fiber pathway: a review. *Neuroscience* **98**(3), 407–427 (2000).
16. Vyleta, N. P., Borges-Merjane, C. & Jonas, P. Plasticity-dependent, full detonation at hippocampal mossy fiber–CA3 pyramidal neuron synapses. *Elife* **5**, e17977 (2016).
17. Villacres, E. C., Wong, S. T., Chavkin, C. & Storm, D. R. Type I adenylyl cyclase mutant mice have impaired mossy fiber long-term potentiation. *J. Neurosci.* **18**(9), 3186–3194 (1998).
18. Weng, F. J. *et al.* Npas4 is a critical regulator of learning-induced plasticity at mossy fiber-CA3 synapses during contextual memory formation. *Neuron* **97**(5), 1137-1152.e5 (2018).
19. Wu, Z. L. *et al.* Altered behavior and long-term potentiation in type I adenylyl cyclase mutant mice. *Proc. Natl. Acad. Sci.* **92**(1), 220–224 (1995).
20. Huang, Y. Y. *et al.* A genetic test of the effects of mutations in PKA on mossy fiber LTP and its relation to spatial and contextual learning. *Cell* **83**(7), 1211–1222 (1995).
21. Otto, C. *et al.* Impairment of mossy fiber long-term potentiation and associative learning in pituitary adenylate cyclase activating polypeptide type I receptor-deficient mice. *J. Neurosci.* **21**(15), 5520–5527 (2001).
22. Formanowicz Jr, D. R., Bradley, P. J., & Brodie Jr, E. D. (1989). Food hoarding by the least shrew (Cryptotis parva): intersexual and prey type effects. American Midland Naturalist, 26–33.
23. Ray, S., Burgalossi, A., Brecht, M. & Naumann, R. K. Complementary modular microcircuits of the rat medial entorhinal cortex. *Front. Syst. Neurosci.* **11**, 20 (2017).
24. Ray, S. *et al.* Grid-layout and theta-modulation of layer 2 pyramidal neurons in medial entorhinal cortex. *Science* **343**(6173), 891–896 (2014).
25. Ray, S. & Brecht, M. Structural development and dorsoventral maturation of the medial entorhinal cortex. *Elife* **5**, e13343 (2016).
26. Waddell, P. J., Kishino, H. & Ota, R. A phylogenetic foundation for comparative mammalian genomics. *Genome Inf.* **12**, 141–154 (2001).
27. Zalutsky, R. A. & Nicoll, R. A. Comparison of two forms of long-term potentiation in single hippocampal neurons. *Science* **248**(4963), 1619–1624 (1990).
28. Wozny, C., Breustedt, J., Wolk, F., Varoqueaux, F., Boretius, S., Zivkovic, A.R., Neeb, A., Frahm, J., Schmitz, D., Brose, N., & Ivanovic, A. The function of glutamatergic synapses is not perturbed by severe knockdown of 4.1 N and 4.1 G expression. J. Cell Sci. **122**(5), 735–744 (2009).
29. Moore, K. A., Nicoll, R. A. & Schmitz, D. Adenosine gates synaptic plasticity at hippocampal mossy fiber synapses. *Proc. Natl Acad. Sci. U S A.* **100**(24), 14397–14402 (2003).

Acknowledgements

This study was supported by grants from the Deutsche Forschungsgemeinschaft (DFG, German Research Foundation): Exc 2049, SFB 1315 (Project-ID 327654276), SPP 1665; the BMBF: 01GQ1420B and a BrainPlay-ERC-Synergy Grant; Stiftung Charité to PB; European Molecular Biology Organization (LTF 853-2017) and Human Frontier Science Program (LT000365/2018) to SR. We thank Undine Schneeweiß for outstanding technical support and Barbara Imbrosci for analysis of CA1 intrinsic properties.

Author contributions

P.B., S.R., L.M.V., A.S., D.P., A.S., N.N. and L.L. performed experiments. P.B., S.R., L.M.V., A.S., and J.B. anaylsed the data. P.B., S.R., M.B. and D.S. designed the study and wrote the manuscript.

Funding

Open Access funding enabled and organized by Projekt DEAL.

Competing interests

The authors declare no competing interests.

Additional information

Supplementary information is available for this paper at https://doi.org/10.1038/s41598-020-73547-6.

Correspondence and requests for materials should be addressed to P.B., S.R. or D.S.

Reprints and permissions information is available at www.nature.com/reprints.

Publisher's note Springer Nature remains neutral with regard to jurisdictional claims in published maps and institutional affiliations.

Supplementary Material

Species-specific differences in synaptic transmission and plasticity

Authors:
Prateep Beed[1,2*‡], Saikat Ray[3,4*‡], Laura Moreno Velasquez[1*], Alexander Stumpf[1*], Daniel Parthier[1], Aarti Swaminathan[1], Noam Nitzan[1], Jörg Breustedt[1], Liora Las[4], Michael Brecht[3] & Dietmar Schmitz[1,2,5,6,7‡]

Affiliations:
1 Neuroscience Research Center, Charité - Universitätsmedizin Berlin, Germany
2 Berlin Institute of Health, 10178 Berlin, Germany
3 Bernstein Center for Computational Neuroscience, Humboldt University of Berlin, Philippstr. 13, Haus 6, 10115 Berlin, Germany
4 Department of Neurobiology, Weizmann Institute of Science, 76100 Rehovot, Israel
5 German Center for Neurodegenerative Diseases (DZNE) Berlin, 10117 Berlin, Germany
6 Cluster of Excellence NeuroCure, 10117 Berlin, Germany
7 Einstein Center for Neurosciences Berlin, 10117 Berlin, Germany

* These authors contributed equally
‡To whom correspondence should be addressed: prateep.beed@charite.de, saikat.ray@weizmann.ac.il or dietmar.schmitz@charite.de

List of Supplementary Material:

1. Figures S1, S2 & S3
2. Table S1

Supplementary Figures

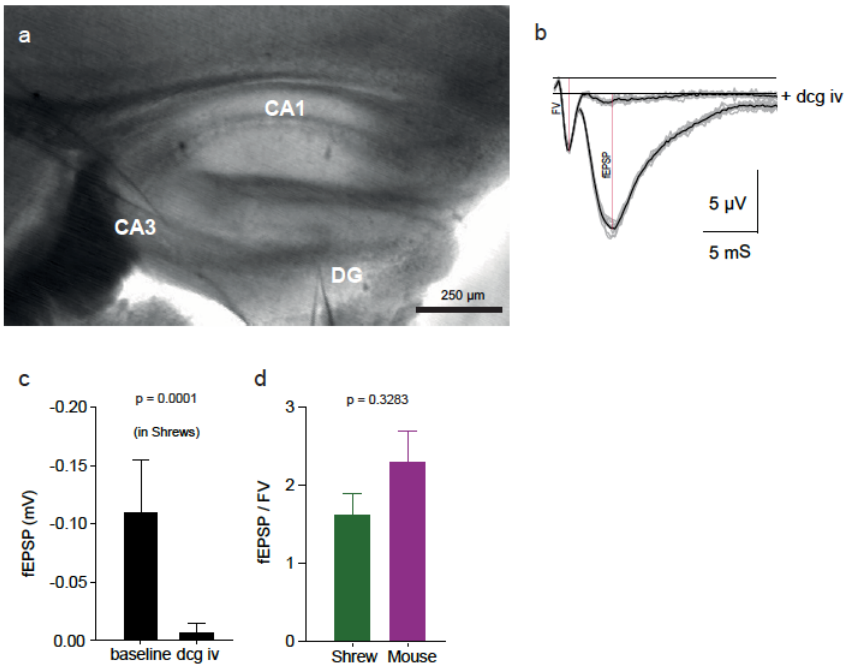

Figure S1 (related to Fig 2) Mossy fibers in shrews are also DCG IV sensitive similar to mice.

(a) Stimulation electrode were placed in the dentate gyrus while the recording electrode was placed in the stratum lucidum in the CA3 area to record mossy fiber inputs.
(b-c) Mossy fiber fEPSPs are DCG IV sensitive **(b)** and the reduction is quantified in **(c)**.
(d) fEPSP to fiber volley ratio are not significantly different between shrews (green) and mice (purple)

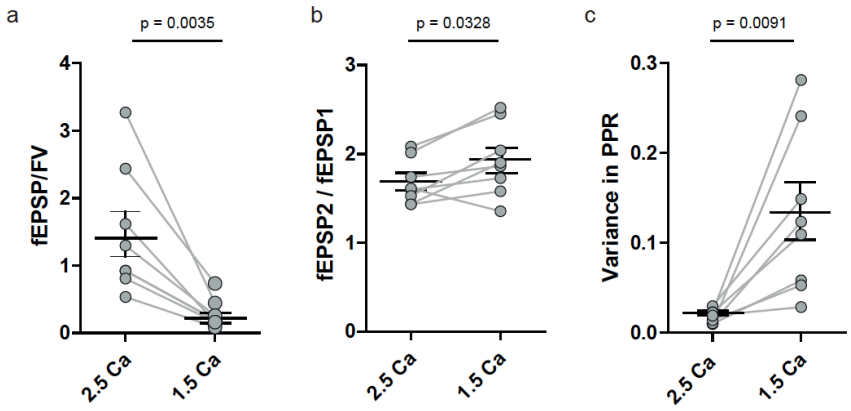

Figure S2 (related to Fig 2) Paired pulse ratios in shrews are minimally affected by changing extracellular calcium concentration at the mossy fiber synapse.

(a) External calcium was reduced from 2.5mM to 1.5mM while recording mossy fiber fEPSP and an expected reduction in the fEPSP to FV change.
(b) Also paired pulse ratio is increased on lowering external calcium.
(c) For every experiment the variance was calculated from 20 sweeps in 2.5 and 1.5mM Calcium. As expected the variance in PPR is higher in lower calcium.

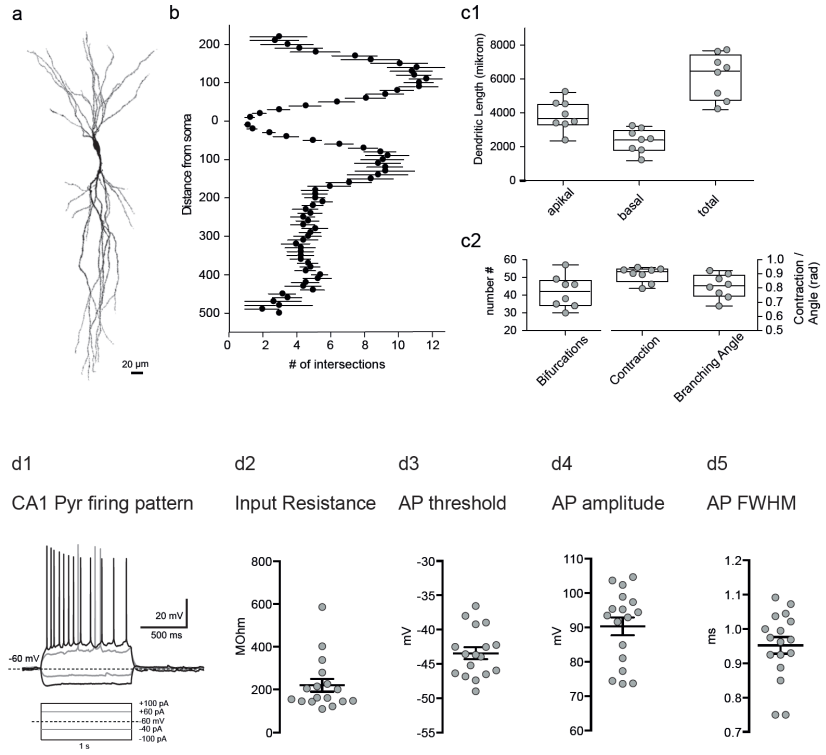

Figure S3 (related to Fig 5) Conserved microanatomy and cellular physiology of pyramidal cells in CA1 of the shrew.

(a) An example of a biocytin labeled CA1 pyramid
(b) Spatial profile of number of intersections of CA1 pyramids in shrews with respect to distance from soma.
(c1) Apical, basal and total dendritic length of CA1 pyramids in shrews (apical: 3802 ± 318 µm, basal: 2313 ± 244 µm, total: 6115 ± 472 µm, n= 8 cells)
(c2) Bifurcations, contraction and branching angle of CA1 pyramids in shrews (bifurcations: 41.9 ± 3.2, contraction: 0.89 ± 0.02, branching angle: 0.81±0.03 rad, n= 8 cells)
(d) Intrinsic properties of CA1 pyramids
(d1) Firing pattern of CA1 pyramidal cells in Etruscan Shrew
(d2) Input resistance
(d3) Action potential threshold
(d4) Action potential amplitude
(d5) Action potential full-width half-maximum

Figure	Experiment	Number of measurements	Number of animals	Mean ± SEM	p-value	Statistical test
1a-b	DAPI intensity (au)	-	7 shrews, 6 mice	-	-	
1c panel 1	DAPI intensity (au)	21 shrews, 18 mice	7 shrews, 6 mice	35.87 ± 1.98 (shrews), 35.36 ± 1.73 (mice)	0.749	Mann whitney two tailed
1c panel 2	DAPI intensity (au)	21 shrews, 18 mice	7 shrews, 6 mice	23.89 ± 1.70 (shrews), 20.79 ± 1.27 (mice)	0.246	Mann whitney two tailed
1c panel 3	DAPI intensity (au)	21 shrews, 18 mice	7 shrews, 6 mice	67.56 ± 3.13 (shrews), 61.18 ± 2.41 (mice)	0.069	Mann whitney two tailed
1c panel 4	DAPI intensity (au)	21 shrews, 18 mice	7 shrews, 6 mice	10.84 ± 1.99 (shrews), 10.27 ± 1.35 (mice)	0.156	Mann whitney two tailed
1c panel 5	DAPI intensity (au)	21 shrews, 18 mice	7 shrews, 6 mice	14.39 ± 1.67 (shrews), 12.10 ± 0.97 (mice)	0.603	Mann whitney two tailed
1c panel 6	DAPI intensity (au)	21 shrews, 18 mice	7 shrews, 6 mice	9.87 ± 1.52 (shrews), 10.85 ± 0.85 (mice)	0.064	Mann whitney two tailed
1f-h	CB+DAPI intensities (au)	21 shrews, 18 mice	7 shrews, 6 mice	0.26 ± 0.04 (shrews), 0.15 ± 0.02 (mice)	0.038	Mann whitney two tailed
2a1-a3	MF FF	15 shrews, 13 mice		240.9 ± 26.32 (shrews), 634.5 ± 45.71 (mice)	<0.0001	Mann whitney two tailed
2b1-b2	MF PPR	13 shrews, 13 mice		1.717 ± 0.115 (shrews), 2.687 ± 0.286 (mice)	0.0002	Mann whitney two tailed
2c1	MF PTP	15 shrews, 13 mice		2.119 ± 0.165 (shrews), 9.342 ± 1.321 (mice)	<0.0001	Mann whitney two tailed
2d1-d3	MF LTP	9 shrews, 7 mice		1.189 ± 0.079 (shrews), 1.759 ± 0.186 (mice)	0.0164	Mann whitney two tailed
3	CB+Syt7 intensities (au)	21 shrews, 18 mice	7 shrews, 6 mice	2.04 ± 0.10 (shrews), 3.13 ± 0.17 (mice)	<0.00001	Mann whitney two tailed
4b-d	Syt7 intensity (au)	-	6 mice, 7 shrews, 5 bats	-	-	-
4e	Syt7 intensity (au)	18	6 mice	3.08 ± 0.15 (CA1), 3.13 ± 0.16 (CA3)	0.41	Paired t-test
4f	Syt7 intensity (au)	21	7 shrews	2.74 ± 0.15 (CA1), 2.05 ± 0.09 (CA3)	<0.0001	Paired t-test
4g	Syt7 intensity (au)	15	5 bats	1.57 ± 0.06 (CA1), 1.35 ± 0.03 (CA3)	0.0009	Paired t-test
5a	CA1 fEPSP/FV	14 shrews 17 mice		6.479 ± 1.405 (shrews) 9.115 ± 1.521 (mice)	0.138	Mann whitney two tailed
5b	CA1 PPR	14 shrews		Shrew data: 1.532 ± 0.079 (50 ms), 1.292 ± 0.047 (100 ms), 1.112 ± 0.024 (200 ms), 1.001 ± 0.013 (500 ms) Mouse data is extracted from Wozny et al., 2009	-	-
5c	CA1 LTP	13 shrews 14 mice			-	-
S1c	MF dcg iv	14 shrews		-0.1104 ± 0.044 mV (EPSP), -0.0081 ± 0.007 mV (dcg iv)	0.0001	Wilcoxon matched-pairs test
S1d	MF fEPSP/FV	11 shrews, 7 mice		1.623 ± 0.266 (shrews) 2.296 ± 0.3978 (mice)	0.3283	Mann whitney two tailed
S2a	MF fEPSP/FV in low Ca^{+2}	8 shrews		1.476 ± 0.331 (2.5Ca), 0.279 ± 0.075 (1.5Ca)	0.0035	Paired t-test

S2b	MF PPR in low Ca^{+2}	8 shrews		1.680 ± 0.088 (2.5Ca), 1.930 ± 0.142 (1.5Ca)	0.0328	Paired t-test
S2c	MF PPR Variance in low Ca^{+2}	8 shrews		0.017 ± 0.003 (2.5Ca), 0.130 ± 0.032 (1.5Ca)	0.0091	Paired t-test
S3c1	CA1 morphology	8 shrews		apical: 3802 ± 318 µm, basal: 2313 ± 244 µm, total: 6115 ± 472 µm	-	-
S3c2	CA1 morphology	8 shrews		bif: 41.9 ± 3.2, contract: 0.89 ± 0.02, br.angle: 0.81 ± 0.03 rad	-	-
S3d2	CA1 Input Resistance	17 CA1 pyramids		220.3 ± 29.7 MΩ	-	-
S3d3	CA1 AP Threshold	17 CA1 pyramids		-43.44 ± 0.865 mV	-	-
S3d4	CA1 AP Amplitude	17 CA1 pyramids		90.27 ± 2.597 mV	-	-
S3d5	CA1 AP FWHM	17 CA1 pyramids		0.952 ± 0.024 ms	-	-

Table S1. Experiments and respective statistical analysis

18. Curriculum Vitae

My curriculum vitae does not appear in the electronic version of my paper for reasons of data protection

My curriculum vitae does not appear in the electronic version of my paper for reasons of data protection

19. List of publications

Oldani S, **Moreno-Velasquez L**, Faiss L, Stumpf A, Rosenmund C, Schmitz D, Rost BR. SynaptoPAC, an optogenetic tool for induction of presynaptic plasticity. J Neurochem. 2021 Feb;156(3):324-336. doi: 10.1111/jnc.15210. Epub 2020 Oct 22. PMID: 33037623. Impact factor 5.372.

Rodríguez de Los Santos M, Rivalan M, David FS, Stumpf A, Pitsch J, Tsortouktzidis D, **Velasquez LM**, Voigt A, Schilling K, Mattei D, Long M, Vogt G, Knaus A, Fischer-Zirnsak B, Wittler L, Timmermann B, Robinson PN, Horn D, Mundlos S, Kornak U, Becker AJ, Schmitz D, Winter Y, Krawitz PM. A CRISPR-Cas9-engineered mouse model for GPI-anchor deficiency mirrors human phenotypes and exhibits hippocampal synaptic dysfunctions. Proc Natl Acad Sci U S A. 2021 Jan 12;118(2): e2014481118. doi: 10.1073/pnas.2014481118. PMID: 33402532; PMCID: PMC7812744. Impact factor 11.205

Beed P, Ray S, **Velasquez LM**, Stumpf A, Parthier D, Swaminathan A, Nitzan N, Breustedt J, Las L, Brecht M, Schmitz D. Species-specific differences in synaptic transmission and plasticity. Sci Rep. 2020 Oct 6;10(1):16557. doi: 10.1038/s41598-020-73547-6. PMID: 33024184; PMCID: PMC7538572. Impact factor 4.379

Moreno-Velasquez L, Lo H, Lenzi S, Kaehne M, Breustedt J, Schmitz D, Rüdiger S, Johenning FW. Circuit-Specific Dendritic Development in the Piriform Cortex. eNeuro. 2020 Jun 19;7(3): ENEURO.0083-20.2020. doi: 10.1523/ENEURO.0083-20.2020. PMID: 32457067; PMCID: PMC7307633. Impact factor 3.544

Maglione M, Kochlamazashvili G, Eisenberg T, Rácz B, Michael E, Toppe D, Stumpf A, Wirth A, Zeug A, Müller FE, **Moreno-Velasquez L**, Sammons RP, Hofer SJ, Madeo F, Maritzen T, Maier N, Ponimaskin E, Schmitz D, Haucke V, Sigrist SJ. Spermidine protects from age-related synaptic alterations at hippocampal mossy fiber-CA3 synapses. Sci Rep. 2019 Dec 23;9(1):19616. doi: 10.1038/s41598-019-56133-3. PMID: 31873156; PMCID: PMC6927957. Impact factor 4.011

Brockmann MM, Maglione M, Willmes CG, Stumpf A, Bouazza BA, **Velasquez LM**, Grauel MK, Beed P, Lehmann M, Gimber N, Schmoranzer J, Sigrist SJ, Rosenmund C, Schmitz D. RIM-BP2 primes synaptic vesicles *via* recruitment of Munc13-1 at hippocampal mossy fiber synapses. Elife. 2019 Sep 19;8: e43243. doi: 10.7554/eLife.43243. PMID: 31535974; PMCID: PMC6752948. Impact factor 7.551

Chatard C, Sabac A, **Moreno-Velasquez L**, Meiller A, Marinesco S. Minimally Invasive Microelectrode Biosensors Based on Platinized Carbon Fibers for *in Vivo* Brain Monitoring. ACS Cent Sci. 2018 Dec 26;4(12):1751-1760. doi: 10.1021/acscentsci.8b00797. Epub 2018 Dec 14. PMID: 30648158; PMCID: PMC6311694. Impact factor 11.228

Rueckl M, Lenzi SC, **Moreno-Velasquez L**, Parthier D, Schmitz D, Ruediger S, Johenning FW. SamuROI, a Python-Based Software Tool for Visualization and Analysis of Dynamic Time Series Imaging at Multiple Spatial Scales. Front

Neuroinform. 2017 Jun 29; 11:44. doi: 10.3389/fninf.2017.00044. PMID: 28706482; PMCID: PMC5489661. Impact factor 3.074

Brossel R, Yahi A, David S, **Moreno Velasquez L**, Guinebretière JM. Mechanical Signals Inhibit Growth of a Grafted Tumor In Vivo: Proof of Concept. PLoS One. 2016 Apr 21;11(4): e0152885. doi: 10.1371/journal.pone.0152885. PMID: 27100674; PMCID: PMC4839666. Impact factor 2.806

Moreno L, Rose C, Mohanraj A, Allinquant B, Billard JM, Dutar P. sAβPPα Improves Hippocampal NMDA-Dependent Functional Alterations Linked to Healthy Aging. J Alzheimers Dis. 2015;48(4):927-35. doi: 10.3233/JAD-150297. PMID: 26402095. Impact factor 4.237

20. Acknowledgements

First of all, I would like to deeply thank my doctoral supervisor Friedrich Johenning for his guidance, mentoring, support and patience throughout my PhD. He has always been available for insights and advises and I have learnt from him not only the techniques I needed to develop my PhD project but also the scientific rigor and personal skills required to pursue my career, I value him highly as supervisor and admire him sincerely as a scientist.

I would like to extend my gratitude to my co-supervisor and PI, Dietmar Schmitz for welcomed me into his group, let me be part of it and grew in it. I am particularly thankful for his support and guidance, for letting me develop my PhD project but also for encouraging me to participate and collaborate in many other projects from which I have learnt many technical and personal skills.

I would also like to thank the BIH for funding part of my PhD and offered me the possibility to develop my scientific skills in and out of the lab through their trainings and workshops.

Special thanks to the technical assistance in the Schmitz lab, Anke and particularly Suse, who have been always very supportive, helpful and essential for the lab. I feel extremely lucky to be part of the Schmitz lab and to have the opportunity to meet and work with the members of this group from which I have only received support. I am tremendously thankful for all the lessons I have learnt from them and all the fun I had all the way along. Thanks to new and former members: Anne-kathrin, Rosie, Feli, Alex, Daniel, Roberto, Constance, Noam, Barbara, Steve, Hung, Marta, Anton, Claire. They will always be part of my precious memories.

Very special thanks to Silvia and Aarti, who were not only my colleagues but they became my friends and family.

Last and more importantly, my greatest gratitude to my family, the most important part of my life. Thanks to my family in Berlin. Nano for your companionship, friendship and all the fun. Thank you Vini for your support, your love and the way you always know how to make feel better. Thank you for standing by my side and make me feel I want to be better. Thanks to my family in Colombia, my parents and my brother. They represent the main driving force in my life and without them none of this would have been possible. All my achievements are thanks to them and are to them.

Special thanks to my Luci and my baby, who came to bring light and colors to my life.